Studying Orientation and Conformation of α-helical Peptides at Interfaces

by

Bei Ding

A dissertation submitted in partial fulfillment
of the requirements for the degree of
Doctor of Philosophy
(Chemistry)
in the University of Michigan
2014

Doctoral Committee:

Professor Zhan Chen, Chair
Assistant Professor Barry Dov Dunietz, Kent State University
Professor Eitan Geva
Professor Ayyalusamy Ramamoorthy
Professor Chuanwu Xi

To my Dad

ACKNOWLEDGEMENTS

First of all I would like to thank my advisor Professor Zhan Chen for his advices and support during my Ph.D years. Professor Chen provided extensive scientific suggestions on my projects. Besides he is a great role model who effectively runs a lab with hard-work and enthusiasm.

I also wish to thank my labmates who helped me in different stages of my Ph.D research. Dr. Xiaofeng Han and Dr. Pei Yang taught me how to operate SFG spectrometers in detail. Dr. Andy Boughton provided beneficial suggestions on data analysis. Besides, I am glad to have the opportunities to collaborate with Jesse Zhang, Yuwei Liu and Lauren Soblosky in several projects.

I am also deeply appreciated the help I received from the the collaborators outside our lab. Prof. John Tesmer and Alisa Glukhova collaborated with us in the "GRK5 segment" project. As structural biologists, they taught me important biological knowledge and ensured that every detail was taken care of in the project. Prof. Martin Zanni and Jennifer Laaser collaborated with us in the "isotope labeling" projects with great passion. They taught me the theoretical ways to treat the signal from the isotope labeled samples. Prof. Ayyalusamy Ramamoorthy, who is also on my dissertation committee, collaborated with us to study antimicrobial peptide LL-37. Prof. Ramamoorthy's lab is interested in a wide range of biological systems and it broadened my horizons whenever I talked with Prof. Ramamoorthy or his students.

I also would like to thank two visiting scholars. I learned SPR technique from Dr. Junqing Geng from Tsinghua University and gained basic knowledge on molecular dynamics simulation from Dr. Zunliang Wang from Southeast University in China.

I would like to thank my committee members Prof. Barry Dunietz, Prof. Eitan Geva, Prof. Ramamoorthy and Prof. Chuanwu Xi for their suggestions and encouragements during the past five years when pursuing my Ph.D degree. I did my second rotation in graduate school with Prof. Barry Dunietz and he taught me how to make use of computational package QChem. This experience provided me the chance to learn about coding which later on became extremely useful in data analysis on SFG spectra.

Finally I would like to thank my family and friends. Thank you for making my life meaningful.

TABLE OF CONTENTS

LIST OF FIGURES

LIST OF TABLES

CHAPTER 1

INTRODUCTION

1.1Goals

Membrane associated peptides and proteins with unique biological functions have drawn extensive attention due to their enormous therapeutic potentials. Being an intrinsic surface-sensitive technique, Sum Frequency Generation (SFG) Vibrational Spectroscopy has the capability to elucidate both structural and orientational information of biomolecules at biointerfaces, e.g., peptides and proteins associated with cell membranes. However, there are significant experimental and theoretical challenges in adapting this application from simple model peptides to more complex systems like proteins associated with cell membranes. My Ph.D. research started with elucidating structure and orientation of a simple linear helical peptide. Then I developed orientation analysis methodology to extend the work to study peptides with more complicated structures and also to proteins. Furthermore, in order to obtain site-specific structural information on peptides, we successfully detected and analyzed signals from an isotope-labeled amide unit in a peptide embedded at the polymer interface. Finally we applied this new technique, isotope-labeled SFG, to observe subtle structure characteristic of a peptide in a single lipid bilayer and the experimental results have been correlated to those obtained from the molecular dynamics simulation work.

1.2Sum Frequency Generation and its Biological Application

1.2.1 SFG Surface Sensitivity

Sum Frequency Generation (SFG) vibrational spectroscopy can be used to study many types of surfaces and interfaces[1-5], but this chapter will focus on studies related to biology. Understanding biointerfaces is the key to understanding diverse topics such as biomedical materials, marine antifouling coatings, biosensors, antimicrobial peptides and membrane proteins. Many analytical techniques have been developed to examine various biointerfacial phenomena such as surface plasmon resonance spectroscopy, neutron reflection, atomic force microscopy, ellipsometry, attenuated total reflectance-Fourier transform infrared spectroscopy (ATR-FTIR) [6]. However, no single technique is capable of elucidating molecular structure of buried interfaces *in situ* (e.g., a solid/liquid interface) with a submonolayer surface specificity.

SFG has been developed into a powerful analytical technique to investigate surfaces and interfaces since 1987[7]. It has been widely applied to identify functional groups, deduce molecular orientation distribution, and investigate dynamics of various molecules at different interfaces including liquid-liquid, air-liquid, and liquid-solid interfaces. In a typical SFG experimental set-up, two pulsed laser beams (a frequency fixed visible and a frequency tunable infrared beams) are overlapped in space and time at the sample interface to generate an output beam at the sum frequency. (Figure 1.1A) The simplified energy level diagram of a SFG process is shown in Figure 1.1B. Using specific polarizations of each of the three beams, it is possible to probe specific components of the second order nonlinear optical susceptibility $\chi^{(2)}$of the sample. This quantity determines the contribution P(2) to the polarization of matter that is induced by the product of the input electric fields of the visible and IR beams Evis(t) and Eir(t): $P^{(2)}$

$=\chi^{(2)}Evis(t)Eir(t)$. Under the electric-dipole approximation, when inversion symmetry is broken (as occurs at surfaces and interfaces), $\chi^{(2)}$ is nonzero, and signals can be detected; this selection rule is the basis for the intrinsic surface specificity for SFG. Thus, SFG can distinguish interfacial species (with inversion symmetry broken) from the bulk molecules (with average inversion symmetry – no signal), eliminating the need to perform background subtraction of bulk signals. Also, SFG signal can be enhanced when the input IR beam frequency is tuned over the vibrational resonances of interfacial molecules, yielding peaks that correspond to vibrational spectra of interfaces. These peaks are characteristic of specific functional groups, and therefore SFG signals can be detected without any fluorescent labels that might change the chemical properties of the sample.

In the following text, SFG studies involving phospholipid bilayers (serving as model cell membranes) will be presented first. Then methods for quantifying the ordering and orientations of peptides and proteins associated with lipid bilayers will be discussed. Lastly, SFG research on proteins at polymer surfaces, with a focus on conformational change and surface immobilization, will be introduced.

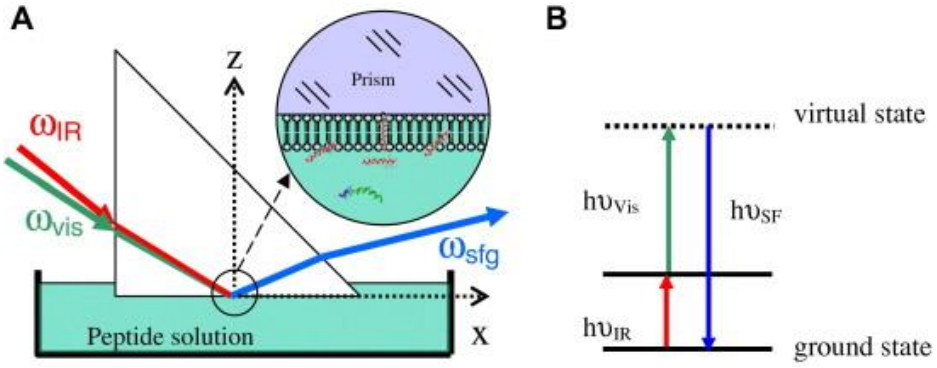

Figure 1.1 SFG experimental geometry and energy diagram. (A) Total reflection geometry. (B) Simplified energy level diagram of SFG process. (Reproduced from ref 17, with permission)

1.2.2 Phospholipids Flip-flop in Model Cell Membranes

Extensive SFG research has been performed on fatty acids and lipid monolayers/bilayers[8-11]. In the literature, some previous research showed that the exchange of lipids between the distal and proximal leaflets of cellular membranes was mediated by proteins named "flipases" or "flopases". Although other techniques such as NMR, fluorescence and EPR have shown that the movement is also possible in the absence of proteins, these studies address labelled lipid species instead of native ones, possibly changing the lipid chemical properties. Conboy and coworkers used SFG to observe the slow translocation movement ("flip-flop") of 1,2-distearoyl-sn-glycero-3-phosphocholine (DSPC) in a planar supported lipid bilayer system, in the absence of protein in situ[12]. As shown in Figure 1.2, their model system has a hydrogenated leaflet and a deuterated leaflet in order to induce asymmetry of the sample for SFG study. As the two leaflets underwent flip-flop and "mixed", the intensity of the SFG signal from the terminal CH_3 symmetric stretching mode of the inner leaflet decreased. Later, the authors measured the phase transition temperatures of different lipids [9]. Unlike the previous work, the bilayer used was symmetric (Figure 1.3) which produced no SFG signal when the sample is uniform in the gel phase and the liquid phase. When the temperature approached the phase transition temperature, heterogeneities arose that resulted in a break in symmetry along the bilayer normal (and, consequently, detectable SFG signals). Together, these bilayer studies showed that SFG can be used to detect a biological process that changes the symmetry. As in the flip-flop study, this was done by introducing isotope labelled lipids to break the original symmetry of the lipid bilayer and study each leaflet of the bilayer simultaneously. Later on, other research groups used similar isotope labelled lipid models to study the interactions between various molecules and the model cell

membrane. For example, molecular interactions between an antibiotic oligomer and a lipid bilayer have been investigated using SFG, showing that the molecule can cut into the lipid bilayer like a knife [11]. When the molecular structure of the oligomer is altered, the interactions with bilayers can be markedly varied [13]. SFG studies also showed that when melittin molecules interact with the lipid bilayer, the two leaflets are disrupted differently, one after the other. When tachyplesin I molecules interact with the bilayer, two leaflets were disrupted simultaneously [14].

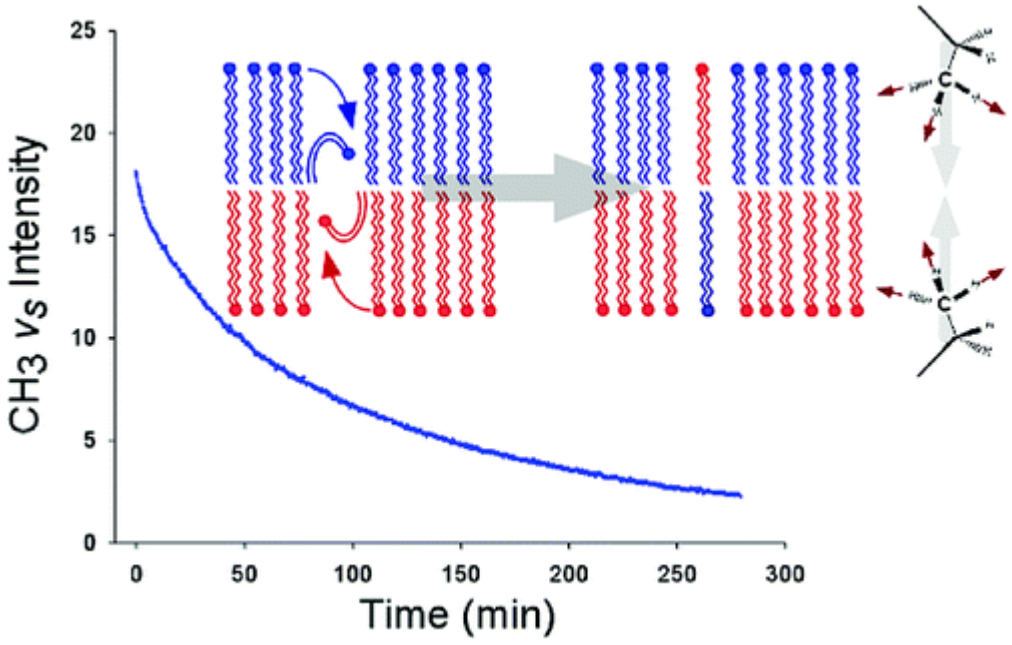

Figure 1.2 SFG spectrum of a DSPC/DSPC-d83 bilayer recorded with s-polarized sum-frequency, s-polarized visible, and p-polarized IR. Insert: schematic of asymmetric lipid bilayer structure. (Reproduced from ref 8, with permission)

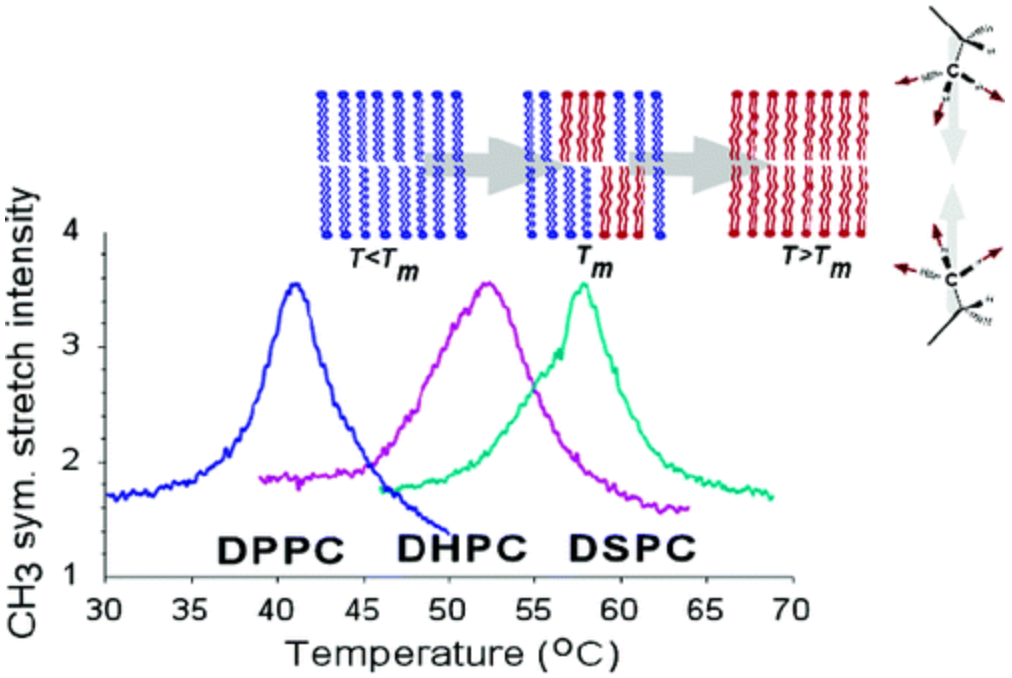

Figure 1.3 Representation of gel (blue) to liquid-crystalline (red) phase transition illustrating domain dislocation and domain size disparity which could give rise to membrane asymmetry. Also shown is the cancellation of the terminal CH_3 symmetric stretching mode in case of symmetric leaflets, i.e. before and after the phase transition (Reproduced from ref 9, with permission)

1.2.3 Peptides with α-helical or β-sheet Secondary Structure in Lipid Bilayers

Analogous to IR spectroscopy, the amide I band in SFG spectra provides information about the secondary structure of peptides and proteins[15,16]. Moreover, polarized SFG spectroscopy can be adopted to deduce the average orientation and orientation distribution.[15-18] For an orientation angle θ, e.g., the tilt angle between an α-helical principal axis and the surface normal, ATR-FTIR can relate the signal intensity ratio measured using different polarized IR beams to $\langle\cos^2\theta\rangle$ (the ensemble average of $\cos^2\theta$).[19] SFG spectroscopy measures different parameters, $\langle\cos\theta\rangle$ and $\langle\cos^3\theta\rangle$, making it possible to characterize the average orientation and orientation distribution in more detail.[19] In addition to providing more measurements than ATR-

FTIR, SFG has a much lower detection limit due to its intrinsic sensitivity. It can be used to study peptides with a low surface coverage and under conditions where ATR-FTIR could not detect any signal.[16]

Zhan Chen group has developed systematic methodologies for orientation analysis on interfacial α-helical, 3_{10}-helical and β-sheet structures using SFG [15,18]. Based on the methodology for α-helical peptides, Zhan Chen and his colleagues have measured the average tilt angle of magainin 2 peptides in lipid bilayers, and found that on the negatively charged (POPG/POPG) lipid bilayer, magainin 2 molecules adopt a transmembrane orientation whereas on the zwitterionic (POPC/POPC) lipid bilayer, a parallel orientation is preferred [16]. These results provided important molecular understanding on the antimicrobial activity and selectivity of magainin 2. Since SFG and ATR-FTIR measure different orientation parameters, the combination of SFG and ATR-FTIR studies can be used to determine complicated orientation distributions.[20] For example, combined SFG and ATR-FTIR studies on α-helical melittin indicate that melittin molecules adopt two distinct orientations, with ~30% roughly standing up while ~70% lie down and tilt slightly on the membrane surface. Such a complicated orientation distribution could not have been determined using only a single technique or measurement alone[20].With the developed data analysis methodology for β-sheet peptides, Zhan Chen group successfully determined the tilt and twist angles of a β-sheet peptide tachyplesin I in DPPG/dDPPG lipid bilayers. Interestingly, unlike linear α-helical peptides, the chiral SFG signals of the β-sheet can be obtained in addition to the signals detected using normal laser polarizations of ssp and ppp. [18]. SFG has also been applied to investigate the membrane orientation of alamethicin, which adopts a mixed α-helical and 3_{10}-helical structure. It was found to adopt a transmembrane orientation in fluid-phase lipid bilayers. [21]

1.2.4 Peripheral Proteins

Extensive efforts have been made to understand the structure and function of proteins associated with cellular membranes.[22,23] Such functions are often dependent on the protein adopting a certain orientation, with is difficult to measure *in situ* with most structural determining techniques. By extending the data analysis methods from simple peptides to larger proteins, SFG was used to study the membrane orientation of Gβγ. This orientation was found to depend on the composition of the lipid bilayer, due to differences in how the protein interacts with each type of lipid [24].

1.2.5 Proteins and peptides at other interfaces

Biomedical technologies commonly involve artificial surfaces that protein can interact with. For example, the first body reaction to a biomedical implant is protein adsorption. The protein-surface interaction determines finally whether the biomaterial can be accepted or rejected by the body. The blood protein Factor XII can be activated on negatively charged surfaces, but not on neutral surfaces.[25] The activation of Factor XII leads to blood coagulation through the intrinsic pathway.[25] Factor XII has been investigated using polarized SFG spectroscopy along with some other techniques. The results showed that a negatively charged polymer surface can cause Factor XII activation by orienting the protein molecules on the surface. [25]

Another important blood protein, fibrinogen, has been investigated comprehensively by Zhan Chen group to understand its molecular behaviour at polymer interfaces. It was shown that fibrinogen changes its conformation over time after adsorption onto various surfaces, including a polyurethane, a silicone-polyurethane copolymer and a fluorinated polymer. After the initial adsorption, fibrinogen adopts a "bent" structure. On the polyurethane surface, fibrinogen slowly

lies down and becomes linear. On the other two surfaces, fibrinogen becomes even more "bent" [26]. SFG has also been used to study fibrinogen on polystyrene surfaces. Orientation analysis on the SFG spectra along with maximum entropy function method supports that fibrinogen exhibits a broad distribution of orientations on polystyrene surfaces [27,28].

Molecular orientation is also important to the understanding of biosensors based on immobilized peptides and proteins like enzymes, for which performance is mediated by the molecular structure (e.g. orientation) of the active site. SFG can be used to directly observe differences in molecular orientation when a variety of immobilization methods are used. SFG results showed that C-terminus cysteine modified cecropin P1 peptides stand up when chemically immobilized onto a polystyrene maleimide (PS-MA) surface but adopt a multiple-orientation distribution when physically adsorbed on the polystyrene surface [29]. SFG results also showed that cecropin P1 immobilized on a maleimide terminated self-assembled monolayer (SAM) via C-terminus ans N-terminus adopt varied conformation/orientation,[30] SFG has been also used to deduce surface orientation of enzyme β-glucosidase immobilized on the surface.[31]

In summary, SFG has been demonstrated to be a powerful tool to study interfacial biological molecules such as lipids, peptides and proteins. It has been shown that SFG studies can provide unique knowledge on lipid flip-flop, lipid phase transition, orientation of peptides and protein associated with model cell membranes, as well as orientations of peptides and proteins physical adsorbed and chemically immobilized on various surface.

1.3 In-depth SFG Data Analysis

1.3.1 SFG Data Analysis Methodology on Linear α-helical Peptides

The orientation determination methodology for an ideal linear α-helical peptide has been reported by our group using the bond additivity model.[15] In this section, we will explain in detail how this methodology can provide us information on the peptide orientation.

First, we generated an orientation curve plotting $\chi^{(2)}_{zzz}/\chi^{(2)}_{xxz}$ as a function of the tilt angle (which is defined as the angle between the helix axis and the surface normal of the supported lipid bilayer). Second, we measured $\chi^{(2)}_{zzz}/\chi^{(2)}_{xxz}$ experimentally. The intensity of experimental SFG spectra is proportional to the square of the effective second order nonlinear optical susceptibility $\chi^{(2)}_{eff,ppp}$.

$$\chi^{(2)}_{\mathrm{eff}} = \chi^{(2)}_{\mathrm{nr}} + \sum_q \frac{A_q}{\omega_n - \omega_q + i\Gamma_q} \qquad (1)$$

where $\chi^{(2)}_{\mathrm{nr}}$ denotes the nonresonant background, A_q denotes the signal strength, ω_n and ω_q are frequencies of the tunable IR beam and a specific vibration mode (the peak center), and Γ_q is the damping coefficient. Thus, we can obtain the ratio of the effective second order nonlinear optical susceptibility $\chi^{(2)}_{eff,ppp}/\chi^{(2)}_{eff,ppp}$ value by collecting and fitting the ppp and ssp spectra of the amide I region. After that, the experimental $\chi^{(2)}_{zzz}/\chi^{(2)}_{xxz}$ can be derived from $\chi^{(2)}_{eff,ppp}/\chi^{(2)}_{eff,ppp}$ value after taking consideration of the Fresnel coefficients.

$$\chi^{(2)}_{\mathrm{eff,ssp}} = \mathrm{L_{xxz}}\chi^{(2)}_{\mathrm{xxz}} \qquad (2)$$

$$\chi^{(2)}_{\mathrm{eff,ppp}} = \mathrm{L_{xxz}}\chi^{(2)}_{\mathrm{xxz}} + \mathrm{L_{xzx}}\chi^{(2)}_{\mathrm{xzx}} + \mathrm{L_{zxx}}\chi^{(2)}_{\mathrm{zxx}} + \mathrm{L_{zzz}}\chi^{(2)}_{\mathrm{zzz}} \qquad (3)$$

The experimental $\chi^{(2)}_{zzz}/\chi^{(2)}_{xxz}$ can be used to determine the tilt angle with the theoretical orientation curve.

An ideal α-helix has a $C_{18/5}$ symmetry. The character table for a $C_{18/5}$ point group shows that there are two types of SFG-active (both IR- and Raman-active) molecular vibrations. [36] The A mode is polarized along the *z* axis (the principal axis of the helix) and the ε_1 and ε_1* vibrations

are circularly polarized down the z-axis. The linear combination of ε_1 and ε_1* vibrations forms the degenerate E1 mode, which is polarized perpendicular to the z-axis. In this paper, we calculated the SFG hyperpolarizability tensor for the A and E1 (ε_1 and ε_1* modes and combined them to the E1) modes.

The SFG hyperpolarizability tensor, β, is described as a product of the IR transition dipole moment and the Raman polarizability tensor.

$$\beta_{lmn,q} \sim \frac{\partial \alpha^*_{lm}}{\partial Q_{\mathrm{q}}} \frac{\partial \mu_{lm}}{\partial Q_{\mathrm{q}}} \quad (1)$$

where *l*, *m*, and *n* denote the molecular coordinates and $(\partial \alpha^*_{lm} / \partial Q_{\mathrm{q}})$ and $(\partial \mu_{lm} / \partial Q_{\mathrm{q}})$ are Raman polarizability and IR dipole moment derivatives with respect to the normal mode coordinate of the *q*th vibrational mode, respectively. In this paper, these derivatives simply mean the components of the Raman polarizability tensor and IR transition dipole moment. Here in a bent helix, to obtain $(\partial \alpha^*_{lm} / \partial Q_{\mathrm{q}})$, we need to sum the Raman polarizability for the two segments. A similar approach was adopted to calculate $(\partial \mu_{lm} / \partial Q_{\mathrm{q}})$.

1.3.2 Limitations

The methodology above will prove to be very useful in next chapters. In Chapter 2 we will show that we use this methodology to elucidate the orientation of the α-helical segment of peptide Pep-1 at different concentrations when associated with liquid-phase lipid bilayers. In Chapter 4, we calculated the orientation information on the α-helical segment of GRK5 protein terminal peptide under different buffer conditions. However, this method is not valid in some circumstances and thus efforts will be made to address this challenge. In Chapter 3, we will

develop data analysis methodology to study LL-37, which adopt different bent structures when associated with different types of vesicles. In Chapter 5 and 6, when we incorporate isotope labels into the peptide backbone to obtain site-specific information, the symmetry of the peptide is broken and the above-mentioned methodology is not valid anymore. Therefore, we will use the Hamiltonian approach instead to calculate the hyperpolarizability for the α-helical peptide.

1.4 Site-specific Information Obtained by SFG

Early experiments which utilize vibrational spectroscopy technique to study peptides and proteins focus mainly on a few peptide backbone vibrations such as amide I, II, III and A modes. [32] However, because the neighboring vibrational modes are highly coupled within the peptide, the vibrational spectra cannot resolve site-specific information.[33] More recently, researchers have incorporated infrared probes such as $^{13}C=O$, $^{13}C=^{18}O$, -CD, -CN, -SCN and $-N_3$ into peptides and proteins to deduce site-specific structural and dynamics information. While IR absorption and Raman Spectroscopy can access the solvent accessibility of a particular site within a peptide or protein in different solvent, 2D IR and Time-resolved IR is able to monitor site-specific conformational charge of biomolecules with different substrates or binding ligands[34]. In 2010, Castner group has incorporated C-D into peptide side chains and measure the SFG signal from a particular site chain of a peptide[35]. In my dissertation chapter 5 and 6, for the first time we incorporated 13C=O into peptide backbones and obtained site-specific orientation from the isotope labeled carbonyl groups in the backbone. This suggested more infrared probes should be introduced to the SFG community for more site-specific structural and dynamic information

1.5 References

.

(1) Zhuang, X.; Miranda, P.; Kim, D.; Shen, Y. *Physical Review B* **1999**, *59*, 12632–12640.

(2) Shen, Y. R.; Ostroverkhov, V. *Chemical Reviews* **2006**, *106*, 1140–54.

(3) Ji, N. A.; Shen, Y. *Chirality* **2006**, *158*, 146–158.

(4) Chen, Z.; Shen, Y. R.; Somorjai, G. A. *Annual review of physical chemistry* **2002**, *53*, 437–65.

(5) York, R. L.; Holinga, G. J.; Somorjai, G. A. *Langmuir* **2009**, *25*, 9369–74.

(6) Lee, A. G. *Molecular bioSystems* **2005**, *1*, 203–12.

(7) Guyot-Sionnest, P.; Hunt, J.; Shen, Y. *Physical Review Letters* **1987**, *59*, 1597–1600.

(8) Liu, J.; Conboy, J. C. *Journal of the American Chemical Society* **2004**, *126*, 8376–7.

(9) Liu, J.; Conboy, J. C. *Journal of the American Chemical Society* **2004**, *126*, 8894–5.

(10) Chen, X.; Wang, J.; Kristalyn, C. B.; Chen, Z. *Biophysical Journal* **2007**, *93*, 866–75.

(11) Chen, X.; Tang, H.; Even, M. a; Wang, J.; Tew, G. N.; Chen, Z. *Journal of the American Chemical Society* **2006**, *128*, 2711–4.

(12) Liu, J.; Conboy, J. C. *Journal of the American Chemical Society* **2004**, *126*, 8376–7.

(13) Avery, C. W.; Som, A.; Xu, Y.; Tew, G. N.; Chen, Z. *Analytical chemistry* **2009**, *81*, 8365–72.

(14) Chen, X.; Chen, Z. *Biochimica et Biophysica Acta* **2006**, *1758*, 1257–73.

(15) Nguyen, K. T.; Clair, S. V Le; Ye, S.; Chen, Z. *The Journal of Physical Chemistry. B* **2009**, *113*, 12169–80.

(16) Nguyen, K. T.; Clair, S. V Le; Ye, S.; Chen, Z. *The Journal of Physical Chemistry. B* **2009**, *113*, 12358–63.

(17) Ye, S.; Nguyen, K. T.; Clair, S. V Le; Chen, Z. *Journal of Structural Biology* **2009**, *168*, 61–77.

(18) Nguyen, K. T.; King, J. T.; Chen, Z. *The Journal of Physical Chemistry. B* **2010**, *114*, 8291–300.

(19) Chen, X.; Wang, J.; Boughton, A. P.; Kristalyn, C. B.; Chen, Z. *Journal of the American Chemical Society* **2007**, *129*, 1420–7.

(20) Chen, X.; Wang, J.; Boughton, A. P.; Kristalyn, C. B.; Chen, Z. *Journal of the American Chemical Society* **2007**, *129*, 1420–7.

(21) Ye, S.; Nguyen, K. T.; Chen, Z. *The Journal of Physical Chemistry. B* **2010**, *114*, 3334–40.

(22) Palczewski, K. *Science* **2000**, *289*, 739–745.

(23) Rasmussen, S. G. F.; DeVree, B. T.; Zou, Y.; Kruse, A. C.; Chung, K. Y.; Kobilka, T. S.; Thian, F. S.; Chae, P. S.; Pardon, E.; Calinski, D.; Mathiesen, J. M.; Shah, S. T. a; Lyons, J. a; Caffrey, M.; Gellman, S. H.; Steyaert, J.; Skiniotis, G.; Weis, W. I.; Sunahara, R. K.; Kobilka, B. K. *Nature* **2011**, *477*, 549–55.

(24) Chen, X.; Boughton, A. P.; Tesmer, J. J. G.; Chen, Z. **2007**, 12658–12659.

(25) Chen, X.; Wang, J.; Paszti, Z.; Wang, F.; Schrauben, J. N.; Tarabara, V. V; Schmaier, A. H.; Chen, Z. *Analytical and Bioanalytical Chemistry* **2007**, *388*, 65–72.

(26) Clarke, M. L.; Chen, Z. *Langmuir* **2006**, *22*, 8627–30.

(27) Wang, J.; Lee, S.-H.; Chen, Z. *The Journal of Physical Chemistry. B* **2008**, *112*, 2281–90.

(28) Wang, J.; Chen, X.; Clarke, M. L.; Chen, Z. *The Journal of Physical Chemistry. B* **2006**, *110*, 5017–24.

(29) Ye, S.; Nguyen, K. T.; Boughton, A. P.; Mello, C. M.; Chen, Z. *Langmuir* **2010**, *26*, 6471–7.

(30) Han, X.; Uzarski, J. R.; Mello, C. M.; Chen, Z. *Langmuir* **2013**, 29, 11705-12

(31) Liu, Y.; Ogorzalek, T. L.; Yang, P.; Schroeder, M. M.; Marsh, E. N. G.; Chen, Z. *Journal of the American Chemical Society* **2013**, *135*, 12660–9.

(32) Krimm, S. *Biopolymers* **1983**, *22*, 217–25.

(33) Hamm, P.; Lim, M.; Hochstrasser, R. M. **1998**, *5647*, 6123–6138.

(34) Hamm, P.; Zanni, M. T. Concepts and Methods of 2D Infrared Spectroscopy

(35) Weidner, T.; Breen, N. F.; Li, K.; Drobny, G. P.; Castner, D. G. *Proceedings of the National Academy of Sciences of the United States of America* **2010**, *107*, 13288–93.

(36) Fanconi, B., Tomlinson, B., Nafie, L. A., Small, W. & Peticolas, W. L. Polarized laser Raman studies of biological polymers. *J. Chem. Phys.* **1969**, *51*, 3993-4005.

CHAPTER 2

MOLECULAR INTERACTIONS BETWEEN CELL PENETRATING PEPTIDE PEP-1 AND MODEL CELL MEMBRANE

2.1. Introduction

The cell penetrating peptide (CPP) family has drawn increasing interest in the field of drug delivery because it is one of the most efficient tools for intracellular access.[1-7] CPPs are usually short peptides with 11 to 34 amino acids. Being highly hydrophilic and cationic, they are able to translocate across the cell membranes carrying various types of cargos, such as peptides, proteins, plasmid DNAs, oligonucleotides and liposome nanoparticles.[8-10] Two main mechanisms for cellular uptake of CPPs have been proposed. One is physically driven to directly interact with and penetrate through the cell membranes and the other is the endocytosis pathway.[11] Although numerous studies have been carried out on the therapeutic effects of CPPs, the molecular-level interactions between cell membranes and CPPs remain largely unknown.[12]

Synthetic peptide carrier Pep-1 is one of the most widely studied peptides in the CPP family. Pep-1 is stable in physiological buffer with high delivery efficiency and low toxicity.[13,14] While many other CPPs must be covalently bound to their cargo, Pep-1 can form non-covalent complexes with a broad spectrum of peptides, proteins, and nanoparticles.[15] A Pep-1 molecule has three segments: a hydrophobic tryptophan-rich motif (KETWWETWWTEW), a spacer

domain (SQP) and a hydrophilic lysine-rich domain (KKKRKV). Previous research using model membranes has shown that Pep-1 appears to directly penetrate through the cell membrane via a physically-driven rather than an endocytosis pathway.[16] This peptide has a high affinity for both neutral and negatively charged cell membranes. NMR and CD experiments have shown that the membrane environment can induce the Pep-1 hydrophobic motif to form an α-helical structure.[16] By measuring the orientation of Pep-1 in bilayers during the process of translocation, it is possible to understand the molecular mechanism of Pep-1/lipid interactions. However, to date inconsistent orientation distributions have been reported for Pep-1 from studies that use a variety of techniques and model systems.[16, 17]

As discussed in the previous chapter, SFG spectroscopy is an intrinsically surface-sensitive technique. It has been widely applied to investigate various types of biointerfaces including those where peptides are associated with model cell membranes.[18-40] With the use of SFG, we can observe the process of peptide adsorption onto the lipid bilayer, monitor changes in the lipid bilayer when the peptide interacts, and obtain conformation and orientation information for peptides with a variety of different secondary structures.[18,41] We have extensively investigated molecular interactions between model cell membranes and various antimicrobial peptides (AMPs) using SFG. The AMPs investigated include magainin 2,[26] MSI-78,[42] alamethicin,[43] melittin[44] and tachyplesin I.[27] But to the best of our knowledge, no CPPs have yet been investigated by SFG. CPPs and AMPs are different classes of peptides. AMPs disrupt bacteria cell membranes via one of several possible modes of action (such as barrel stave, toroidal pore formation or a carpet model) above some threshold concentration, while CPPs usually enter the cell through a physically-driven or endocytosis pathway without disrupting the membranes. The concentration of CPPs required for translocation to occur is usually lower than

that required for AMPs to disrupt the cell membranes and therefore a technique with high sensitivity to study CPPs is necessary. In fact, previous research has shown that when increasing the concentration of Pep-1 molecules, they will exhibit toxicity and behave similar to AMPs towards cell membranes.[45] Also, it may be challenging to observe the translocation process of CPPs into cells using the simple model cell membranes (e.g., solid supported lipid bilayers) often used for SFG. For example, the endocytosis pathway may require non-lipid components (such as caveolars) to be present in the membrane.[46] The transmembrane potential, which is believed to be a driving force for Pep-1 translocation also adds to the difficulty of the use of model systems.[45, 47]

As a technique with a high sensitivity as well as the ability to obtain orientation information, SFG spectroscopy was applied to study cell penetrating peptide Pep-1 for the first time in this work. The results revealed that SFG spectroscopy is sensitive enough to detect Pep-1 associated with lipid bilayers and can be used to deduce the orientation of Pep-1 at low concentrations suitable for the study of peptide translocation. The different behaviors of CPPs on gel-phase and liquid-phase lipid bilayers observed explain why the fluidity of the membrane plays an important role in CPP translocation. In addition, attenuated total reflectance - Fourier transform infrared spectroscopy (ATR-FTIR) was used as a supplemental technique to confirm the conclusions drawn from the SFG study. This study is the first step towards fully understanding how CPPs deliver cargo. Studies on the interactions of CPPs with more advanced cell model systems and the translocation process of CPPs with drugs into cells will be carried out in the future.

2.2 Experimental Details

Pep-1 (sequence H-KETWWETWWTEWSQPKKKRKV-OH) was purchased from Anaspec with >95% purity. Hydrogenated and deuterated 1,2-dipalmitoyl(d62)-sn-glycero-3-phosphoglycerol (DPPG and dDPPG) and 1-palmitoyl-2-oleoyl-sn-glycero-3-phospho-(1'-rac-glycerol) (POPG) were purchased from Avanti Polar Lipids Inc (Alabaster, AL).

Lipid bilayers were deposited on CaF_2 right angle prisms (Altos Photonics, Bozeman, MT). Langmuir-Blodgett and Langmuir-Schaefer (LB/LS) methods were used to deposit the proximal and then the distal leaflets of the lipid bilayers, respectively.[26, 44] The first layer is deposited on one of the square faces of the right-angle CaF_2 prism with A KSV2000 LB system: The plasma-cleaned prism was first immersed in the LB trough. Then a certain amount of lipid chloroform solution, typically 5 drops of 10 mg/ml, was spread on the water surface until the surface tension reaches ~5 mN/m. Two barrier arms were suppressed so that the surface tension remains 34 mN/m, while the CaF_2 prism was lifted from the subphase. A layer of lipids was deposited on the face perpendicular to the water surface in this way. After aligning the laser beams to find the monolayer signal, a 2 ml reservoir filled with water were placed beneath the prism. Lipids were added to the surface of the water in the reservoir so that the surface tension is around 34 mN/m. The reservoir was elevated so that the water surface contacts with the first layer deposited on the prism to form a lipid bilayer. A KSV2000 LB system and ultrapure water from a Millipore system (Millipore, Bedford, MA) were used throughout the experiments for bilayer preparation. The bilayer was immersed in 50 μM pH=7.2 phosphate buffer inside of a 2 mL reservoir during the experiment. 80, 16 and 3.2 μL of 0.5 mg/mL Pep-1 was injected into the reservoir for concentration-dependent experiments. A magnetic microstirrer was used at a rate of 100 rpm to ensure a homogeneous concentration distribution of peptide molecules in the

subphase below the bilayer. The final concentrations of the peptide solutions are 7.0 μM, 1.4 μM and 0.28 μM.

The details of SFG theory, our SFG setup and our experimental design have been described previously and Chapter 1.[26, 48-62] Spectra were collected from peptides associated with the lipid bilayers in ssp (s-SFG, s-visible, p-IR) and ppp polarization combinations using our previously reported near total reflection geometry.[26,44] ATR-FTIR experiments were performed with a Nicolet Magna 550 FTIR spectrometer using a detachable ZnSe total internal reflection crystal (Specac Ltd. RI, U.K.).[44] The substrate surface was cleaned with methanol, Contrex AP solution, and deionized water, followed by a treatment in a glow discharge plasma chamber for 2 min to remove residual hydrocarbon contamination. The lipid bilayer was deposited on the crystal surface with a procedure previously reported.[44] The appropriate volume of a Pep-1 stock solution (in D_2O phosphate buffer) was injected into the subphase of 1.6 mL to achieve the above mentioned concentrations. The s- and p-polarized ATR-FTIR spectra were recorded 1h, followed by a return to the s polarization to ensure that samples were equilibrated and did not change during the timescale of the experiments.

2.3 Results

2.3.1 SFG Results on Pep-1 Interacting with Gel-phase Lipid Bilayers

SFG spectra were collected with dDPPG/DPPG bilayers in contact with Pep-1 solutions with different peptide concentrations. At the low Pep-1 concentration of 0.28 μM, no SFG amide I signal from Pep-1 in the lipid bilayer was observed. When the Pep-1 concentration was increased to 1.4 μM, SFG amide I signals centered at 1677 cm^{-1} was detected from Pep-1 associated with the lipid bilayer, as shown in Fig. 2.1a. This peak center indicates that Pep-1

likely forms β-sheet type structures on the gel-phase membrane interfaces. The SFG amide signal is quite broad, showing a high degree of structural heterogeneity. This peak center shifted to 1663 cm^{-1} when the Pep-1 concentration was increased to 7.0 μM (Fig. 2.1b), which may indicate a change in secondary structure to β-turns and/or disordered structure.

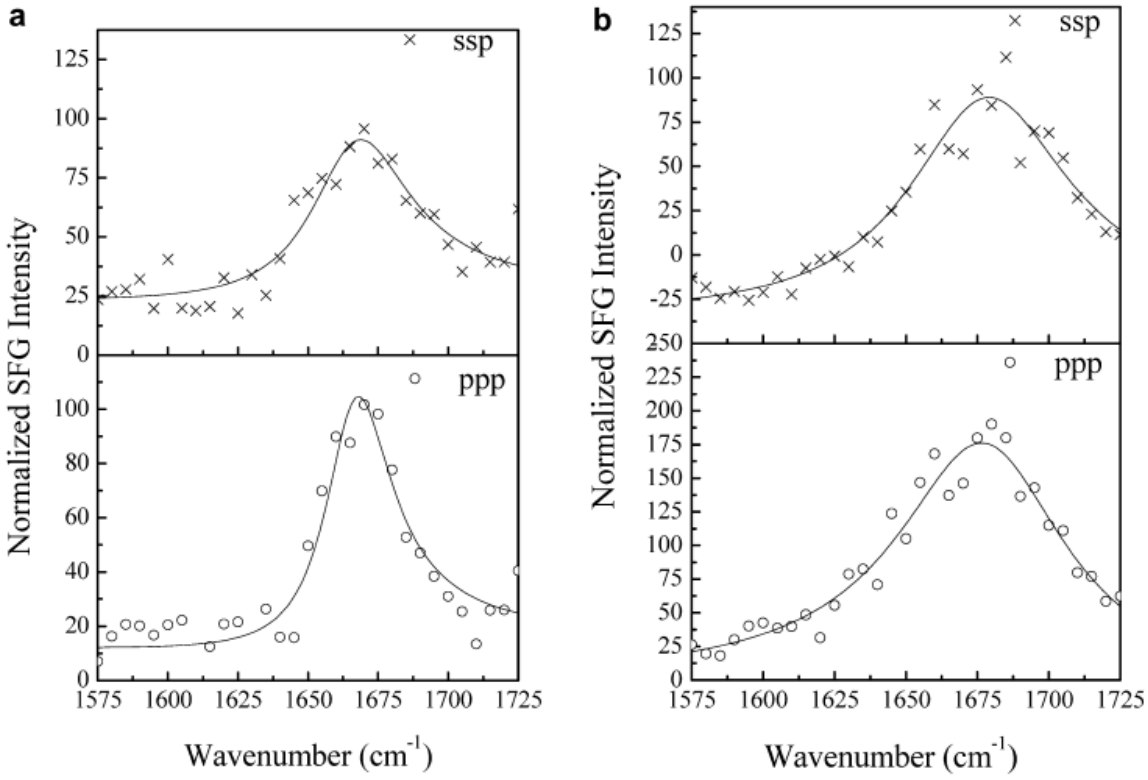

Figure 2.1 The ssp and ppp SFG amide I spectra of Pep-1 associated with a dDPPG/DPPG bilayer at the peptide concentrations of 1.4 μM (a) and 7.0 μM (b).

The adsorption and association of Pep-1 to the dDPPG/DPPG bilayer can also be confirmed by the SFG signals collected in the O-H stretching frequency region. Such SFG signals are contributed by ordered water molecules associated with the charged lipid head groups of the dDPPG/DPPG lipid bilayer. As shown in Fig. 2.2, at the low peptide concentration of 0.28 μM, the detected SFG signal from water decreased upon addition of the peptides, but the spectral

feature did not differ substantially. The water SFG signals at 3200 cm^{-1} and 3500 cm^{-1} greatly decreased when the peptide concentration was increased to 1.4 μM and completely disappeared at the high concentration of 7.0 μM. We believe that the positively charged Pep-1 molecules interact with and neutralize the negatively charged head group of the dDPPG/DPPG bilayer, therefore disordering the water molecules originally associated with the bilayer. The SFG signals observed in the O-H stretching frequency region indicate that water molecules on the bilayer surface were removed and/or disordered by the adsorption of Pep-1 molecules. When combined with the amide I signals, these results confirm that Pep-1 molecules at a variety of concentrations interact with dDPPG/DPPG bilayers.

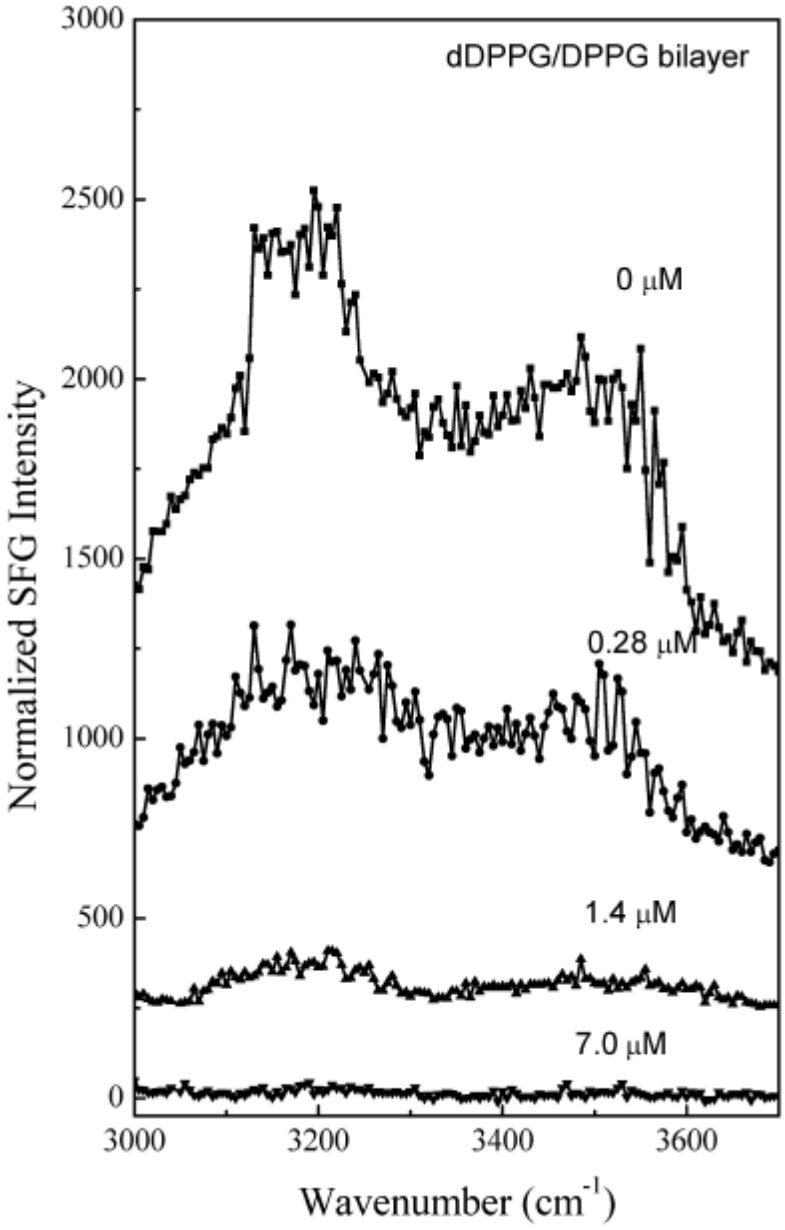

Figure 2.2 The ssp SFG spectra in the O-H stretching frequency range detected when the dDPPG/dDPPG bilayer is in contact with Pep-1 solutions with different concentrations.

We also studied the behavior of the lipid bilayer when interacting with Pep-1. To avoid a potential overlap of signals from the peptide and the lipids in the C-H stretching frequency region, we also used a fully deuterated lipid bilayer (dDPPG/dDPPG). Amide I spectra from the

peptide were found to be the same as when dDPPG/DPPG bilayers were used. No C-D stretching signal was observed from the lipids before the addition of Pep-1 to the subphase, showing that the dDPPG/dDPPG bilayer was symmetric (as expected). After the introduction of Pep-1 into the subphase, at the concentration of 7.0 μM, no SFG C-D stretching signal was detected (Fig. 2.3). This implies that Pep-1 binds to the lipid headgroups rather than inserting into the gel- phase lipid bilayers. This observation is different from the peptides that disrupt the gel-phase lipid bilayers we investigated previously.[63]

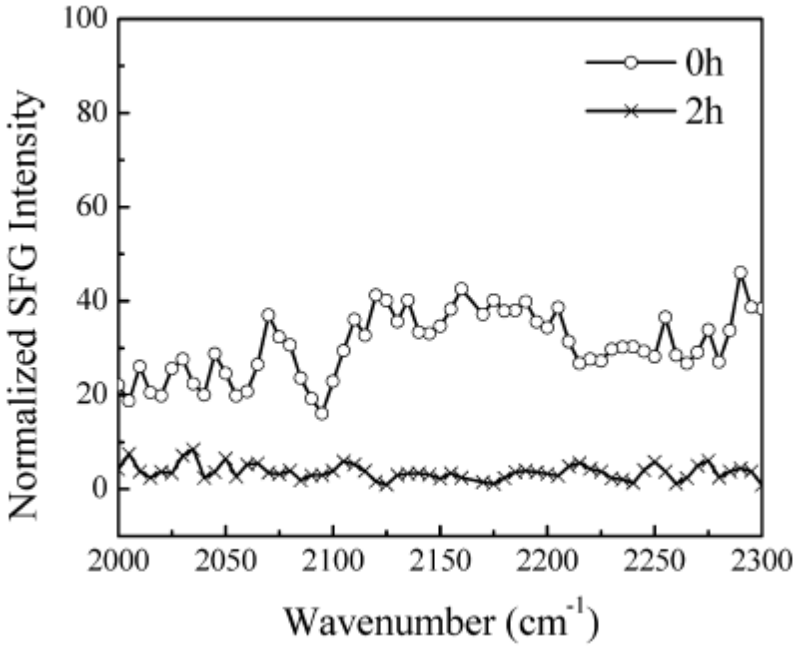

Figure 2.3 The ssp SFG spectra in the C-D stretching frequency range detected before, and two hours after, the dDPPG/DPPG bilayer is in contact with the Pep-1 solution with a concentration of 7.0 μM.

2.3.2 SFG Results on Pep-1 Interacting with Liquid-phase Lipid Bilayers

Concentration-dependent Pep-1 experiments were also performed using liquid-phase lipid bilayers (POPG/POPG), and the results were compared to those from gel-phase bilayers. Unlike

the asymmetric dDPPG/DPPG bilayer, the disruption of the POPG bilayer could not be monitored directly by SFG. This is because POPG bilayers are prone to rapid flip-flop, and this rapid exchange of lipids between leaflets prevents the use of deuterated lipids to create asymmetry. Thus in this section we mainly focus on the SFG signals generated from the peptides. It is found that the SFG spectra collected from Pep-1 in fluid phase bilayers were significantly different from the gel phase bilayer results.

Fig. 2.4 shows the SFG amide I signals collected from Pep-1 interacting with a POPG/POPG bilayer with the same peptide concentrations as used previously. At the low concentration of 0.28 μM, a prominent peak at 1653 cm^{-1} was detected in both the ssp and ppp spectra, suggesting that some peptide molecules associated with the POPG/POPG bilayer adopted an α-helical structure. Additional peak shoulders at 1634 cm^{-1} and 1670 cm^{-1} indicate the coexistence of a β-sheet structure. At the intermediate concentration of 1.4 μM, in addition to the dominant 1651 cm^{-1} peak, shoulders at 1630 cm^{-1} and 1673 cm^{-1} were also detected. Therefore, at these two concentrations, Pep-1 adopts a mix of α-helical and β-sheet structures when associated with the POPG/POPG bilayer. SFG spectra were also collected from Pep-1 molecules associated with the POPG/POPG bilayer when the peptide concentration was increased to 7.0 μM. Interestingly, for a high solution concentration of Pep-1, the observed peak intensities in the SFG spectra were much *weaker* than signals detected at lower peptide concentrations. It is well known that the SFG intensity is affected by molecular ordering/orientation as well as the number of molecules, and a drop in signal as peptide concentration increases suggests that the Pep-1 molecules were either lying down on the surface or else adopted a more random orientation distribution.

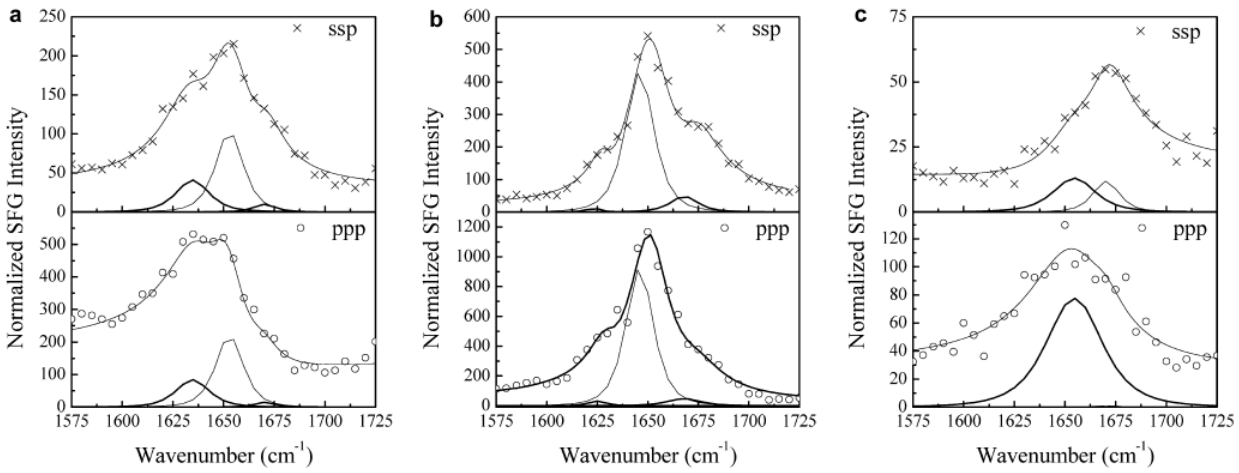

Figure 2.4 The ssp and ppp SFG amide I spectra of Pep-1 associated with a POPG/POPG bilayer at the peptide concentrations of 0.28μM (a), 1.4 μM (b) and 7.0 μM (c).

The orientation information could be further quantified with the methodology our group has recently developed.[26, 65] We want to emphasize here that the 1653 cm^{-1} peak is solely due to the α-helical structure based on the following reasons. (a) Due to the lack of a high-resolution three-dimensional structure, we were unable to calculate the SFG signal contributed by the random coil section of Pep-1. However, in other cases such as cytochrome-b5,[71] we found that the random coil part of the peptide would contribute less than 2% of the SFG signal generated from the α-helical components, even if they could have a somewhat ordered structure. This means that unlike linear vibrational spectroscopic techniques (e.g., FTIR), SFG is much more sensitive to α-helices than random components. (b) It was reported in ref. 64 that the structure of Pep-1 calculated by DYANA has free C and free N termini (referred to as PepW in the paper). The random coil parts in this structure are very dynamic and have no preferred ordering. Therefore even if the random coil part contributes a small SFG signal from one peptide molecule, those signals would be averaged out as an ensemble. (c) The width for the SFG α-helical peak (e.g., at 1.4 μM peptide concentration) is 12 cm^{-1} with a peak center of 1653cm^{-1}.

These parameters are similar to those of the purely α-helical peptide magainin-2.[26] If random coil signals contributed to the overall lineshape, we would expect to see a larger peak width and a lower peak center frequency.

To relate the expected signal intensities to molecular orientation (also see Chapter 1 for calculation details), we first generated a theoretical curve by plotting the ratio between the two susceptibility tensor elements $\chi^{(2)}_{zzz}/\chi^{(2)}_{xxz}$ for the α-helix peak as a function of the tilt angle of α-helical component (residues 4-13)[16, 64] of the Pep-1 molecules associated with the lipid bilayer.[65] Here we define the molecular c axis as along the α-helical backbone and the tilt angle θ is the angle between the backbone and the surface normal of the bilayer. Then we calculate the experimental value of $\chi^{(2)}_{zzz}/\chi^{(2)}_{xxz}$ from the fitted signal strength ratio $\chi^{(2)}_{ppp}/\chi^{(2)}_{ssp}$, which includes a correction for the Fresnel coefficients. Lastly, we find the corresponding orientation information of the experimentally measured $\chi^{(2)}_{zzz}/\chi^{(2)}_{xxz}$ from the generated theoretical curve. If we assume that the molecules adopt a Gaussian orientation distribution, the relationship between the ratio $\chi^{(2)}_{zzz}/\chi^{(2)}_{xxz}$ and the tilt angle θ of the α-helix relative to the bilayer normal is plotted in Fig. 5, for various distribution widths. For Pep-1 in fluid-phase lipid bilayers, the ratio $\chi^{(2)}_{zzz}/\chi^{(2)}_{xxz}$ was found to depend on the peptide concentration: 1.81 ±0.03 for Pep-1 in the lipid bilayer at the intermediate peptide concentration of 1.4 μM, and 1.75 ±0.07 at the low concentration of 0.28 μM. The larger error bar in the measurement from the low peptide concentration is because the lower SFG signal led to a weaker signal to noise ratio. The deduced tilt angles (relative to the membrane normal) for the two peptide concentrations are ~15˚and ~18˚, respectively, if we assume that all molecules adopt the same orientation (σ is 0˚, a δ-distribution). If the distribution width is assumed to be 10 degrees, the tilt angles for the two concentrations are ~3˚and ~12˚,

respectively. Based on the experimental data and the curves in Figure 2.5, a Gaussian distribution of 20^{o} or greater would be unlikely. This implies that for both concentrations, the helical components in the Pep-1 molecules in the POPG/POPG bilayer orient more or less perpendicular to the membrane surface with a narrow distribution. If we assume that the molecules at both concentrations adopt a δ-distribution, we can further deduce from the fitted SFG signal strengths that the ratio of the number of Pep-1 molecules in lipid bilayers for 0.28 μM and 1.4 μM cases is about 1:2 (although the ratio of the numbers of peptide molecules in the bulk solutions is 1:5). At higher concentration 7.0 μM, although the overall spectral lineshape was reproducible, the reduced signal intensity hindered efforts to reliably determine molecular orientation.

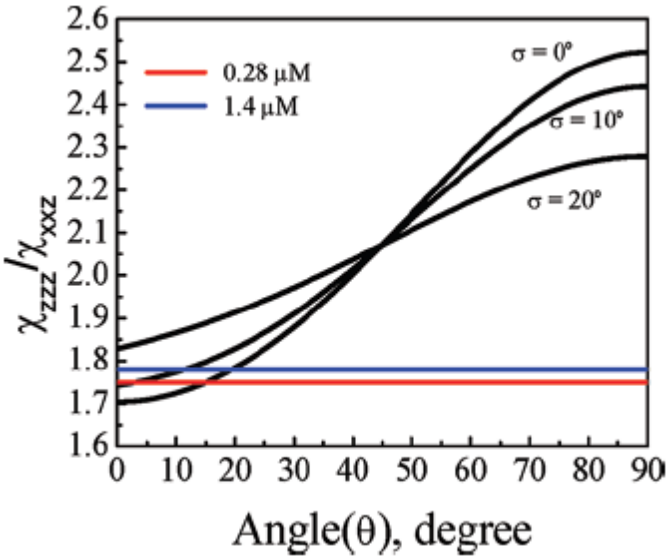

Figure 2.5 Dependence of the measured SFG $\chi^{(2)}_{zzz}/\chi^{(2)}_{xxz}$ ratio of a 10-residue α-helix on the helix tilt angle relative to the surface normal.

Helices interacting with lipid membranes sometimes unravel in the end. In a previous publication, we reported the calculated SFG responses of alpha helices with different numbers of amino acids[65] (11, 10 and 9 residues), but these curves are quite similar especially in the region

of interest. Therefore a slight unraveling would not affect the conclusion that the peptides mainly adopt a perpendicular orientation.

The SFG spectra collected in the O-H stretching frequency region show that the O-H stretching signals decreased after the Pep-1 molecules were introduced to the subphase of the fluid-phase bilayer (Fig. 2.6). This is similar to what was observed when a gel-phase dDPPG/DPPG bilayer was used. However, for the fluid phase bilayer, the drop in signal intensity is accompanied by a change in the overall lineshape the O-H stretching frequency region. We believe that this change is due to the SFG signal generated from the N-H stretching mode at 3300 cm^{-1}. Previous NMR studies showed that residues 4-13 could form a well-defined amphipathic α-helix, resulting in a hydrophobic face built by five Trp residues.[64] The 3300 cm^{-1} peak therefore could come from the N-H groups of these Trp residues in the side chains. It has shown previously that SFG signals in this region are contributed by amino acid side chains.[38, 70] No peak at 3300 cm^{-1} peak was seen for Pep-1 in gel-phase lipid bilayers, suggesting that lipid bilayer phase has an effect on peptide conformation or side chain ordering. We can conclude that Pep-1 adopts different conformations when associated with the gel-phase and liquid-phase bilayers. For the intermediate Pep-1 concentration of 1.4 μM, the 3300 cm^{-1} peak became more distinct due to the further decrease in the water O-H stretching signal. For the higher peptide concentration of 7.0 μM, the signal in the O-H stretching region decreased further, indicating the bilayer associated water molecules were even more disordered. However, no N-H stretching signals were observed at this higher concentration, suggesting that the Pep-1 molecules associated with the lipid bilayer adopt a different orientation (or orientation distribution) at the high peptide concentration compared to that at the intermediate concentration. Again, this agrees with the results obtained from studies on the amide I frequency region.

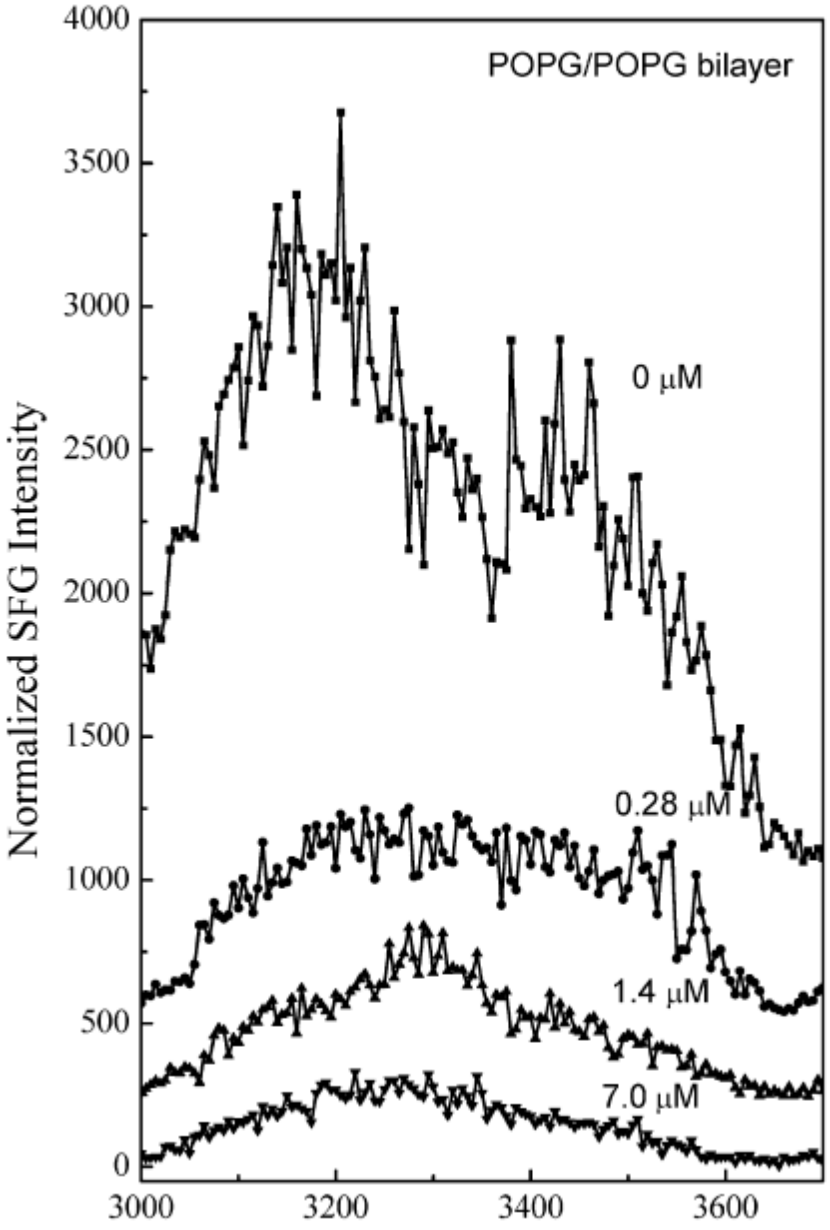

Figure 2.6 The ssp SFG spectra in the O-H stretching frequency range detected when the POPG/POPG bilayer is in contact with Pep-1 solutions with different concentrations.

2.3.3 ATR-FTIR Results on Pep-1 Interacting with Liquid-phase Lipid Bilayers

We also performed ATR-FTIR experiments to supplement our SFG studies on Pep-1 interacting with lipid bilayers. Whereas SFG is more sensitive to α-helices than β-sheets or

random coils due to the dependence of SFG signals on molecular ordering, ATR-FTIR can readily detect amide I signals from many different secondary structures, but it is not able to detect very low concentrations of peptides.

No discernible ATR-FTIR signal was detected from Pep-1 associated with the POPG/POPG bilayer at low (0.28 μM) and intermediate (1.4 μM) peptide concentrations. At the high peptide concentration of 7.0 μM, ATR-FTIR signals were observed (Fig. 2.7). The fitting results for the ATR-FTIR spectra collected using the s- and p-polarized light are shown in Table 2.1. From the signal strength ratio of the s and p polarized spectra, the tilt angle of the α-helical component with respect to the membrane normal was determined to be 52˚, assuming a δ orientation distribution (Fig. 2.8). However, as we discussed in Section 4.2, very weak SFG signals were detected from 7.0 μM Pep-1 in the POPG/POPG lipid bilayer, suggesting that the δ-distribution is not a good assumption here. In fact, this orientation angle deduced by polarized ATR-FTIR is close to the "magic" angle (54.7˚) that would be predicted for a random orientation of molecules. From the combination of SFG and ATR-FTIR we believe that the helical sections of Pep-1 molecules adopt a random orientation distribution.

Frequency	Assignment	Peak Width	A (S polarization)	A (P polarization)
1673	Turn and β-sheet	9.72	0.007	0.014
1656	α-helix	6.46	0.0205	0.0308
1640	Random coil	6.97	0.0229	0.033
1628	Intermolecular β-sheet	6.87	0.0065	0.0091
1613	Side chains	10.59	0.012	0.020

Table 2.1 Fitting parameters for s and p polarized ATR-FTIR spectra.

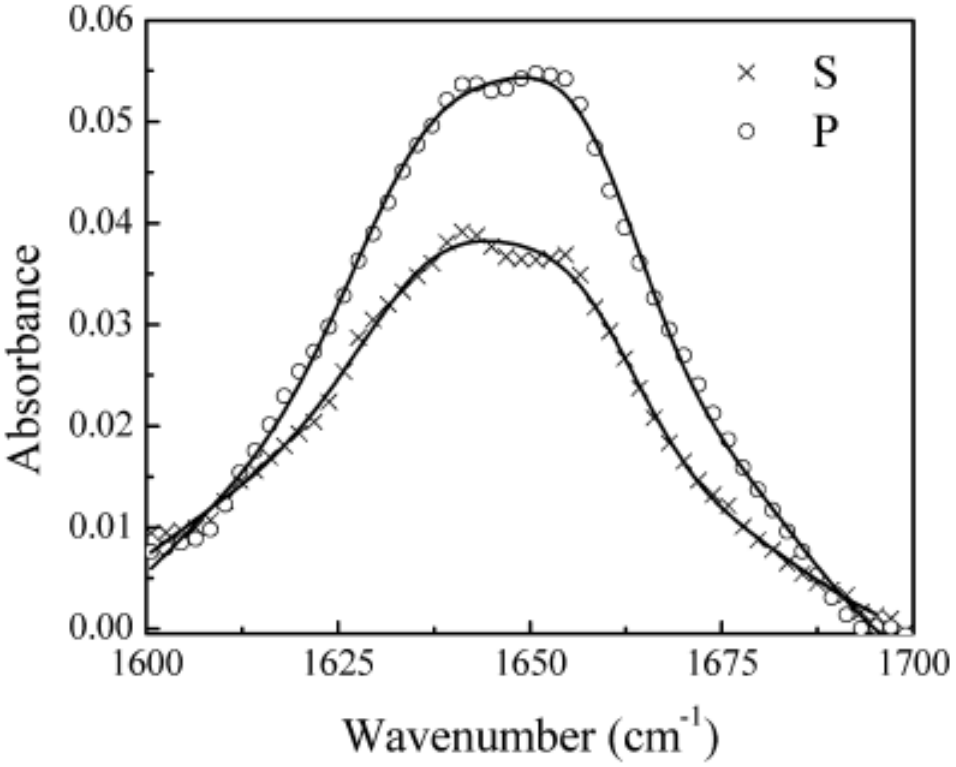

Figure 2.7 Polarized ATR-FTIR amide I spectra of Pep-1 in a POPG/POPG bilayer in contact with the peptide solution with a concentration of 7.0 μM.

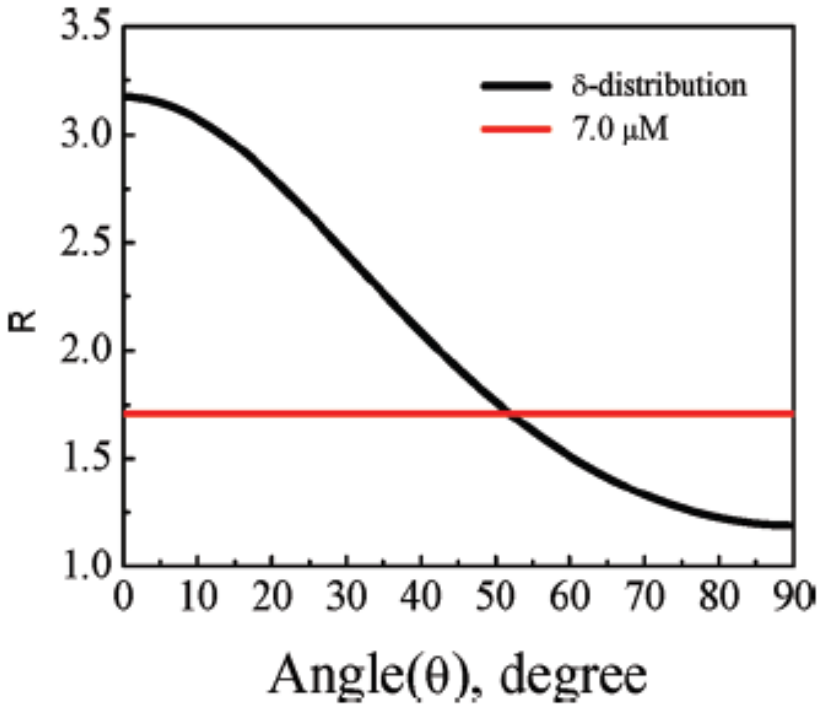

Figure 2.8 Dependence of the ATR-FTIR measured p to s spectral intensity ratio of an α-helix on the helix tilt angle vs. the surface normal.

2.4 Further Discussion and Conclusion

Previous studies using surface plasmon resonance (SPR) showed that Pep-1 - lipid interactions are modulated by membrane fluidity.[66] When the fluidity increases, more Pep-1 molecules bind and insert into the membrane. This is in agreement with our results from SFG and ATR-FTIR, but our results provide a way to reveal molecular level information about Pep-1 conformation and orientation while interacting with lipid bilayers.

While ATR-FTIR has been proven to be a powerful tool to study the conformations of peptides associated with membrane lipids, previous work focused on samples that were semi-dehydrated. As a result, Pep-1 molecules not inserted into the membrane could precipitate as aggregates and contribute to the ATR-FTIR spectrum.[17] By contrast, SFG is uniquely sensitive to

interfaces, and therefore can selectively monitor the structures of peptides associated with the lipid bilayer without contributions from peptide molecules in the bulk environment (e.g., in solution or as aggregates). Also, compared to ATR-FTIR, SFG is more sensitive. Whereas no ATR-FTIR signals were observed from Pep-1 in a POPG/POPG bilayer at peptide concentrations of 0.28 and 1.4 μM, SFG signals were detected at those concentrations. By using different polarization combinations of the laser beams, we are able to deduce the orientation of the α-helical component of Pep-1. Our results clearly show that Pep-1 can interact with both gel-phase (DPPG) and fluid-phase (POPG) lipid bilayers, as indicated by a decrease in the water O-H stretching signal from water molecules at the lipid-water interface. In gel-phase lipid bilayers, Pep-1 generated very weak signals centered around 1670 cm^{-1} in the amide I frequency range, suggesting a random coil or β-sheet conformation. By contrast, for fluid-phase bilayers at low and intermediate Pep-1 concentrations, a strong peak around 1653 cm^{-1} could be detected from, indicating an α-helical conformation.

2.4.1 Orientation Information

Elucidating the orientation of the α-helical component in Pep-1 is essential to understand the process of membrane translocation. Previous studies on this process have produced various results. For example, based on fluorescence results, Heitz et al. first proposed that translocation involves the construction of a transient transmembrane pore-like structure.[16] They concluded that the tryptophan residues in the α-helix are embedded in a hydrophobic environment, which would be consistent with Pep-1/ membrane interactions that place the helical axis perpendicular to the membrane plane. Further support for this claim came from electrophysiological measurements.[67] However, spin-label studies by Weller and coworkers revealed a three-amino acid periodicity in signal attenuation, leading them to conclude that CPP lies parallel with the surface of DPC/SDS

micelles.[64] ATR-FTIR has also been applied to measure the *in situ* orientation of Pep-1 with respect to the membrane normal in various types of lipids, and without the need for exogenous labels.[17] In POPC and mixed POPC/Cholesterol multilayers, the angles were measured to be 46.5˚ and 44.5˚, respectively. These values are not very different from the average orientation angle expected for randomly oriented peptides. It was suggested from such measurements that the cyto-toxicity of Pep-1 is due to a "carpet-like" mechanism. Their study[17] used high concentrations of Pep-1. Translocation activity at lower peptide concentrations was not studied, possibly due to the limited sensitivity of ATR-FTIR spectroscopy.

The combined SFG and ATR-FTIR studies reported in this paper showed that the behavior of Pep-1 associated with POPG/POPG bilayers is concentration-dependent (schematic in Fig. 2.9). At the highest concentration of 7.0 μM, results lead to a random orientation of Pep-1 helical component, in agreement with the previous ATR-FTIR studies.[17] At the low and intermediate peptide concentrations, SFG results showed that the Pep-1 helical component is more or less perpendicular to the lipid bilayer surface, indicating that Pep-1 inserts into the membrane in this concentration range.

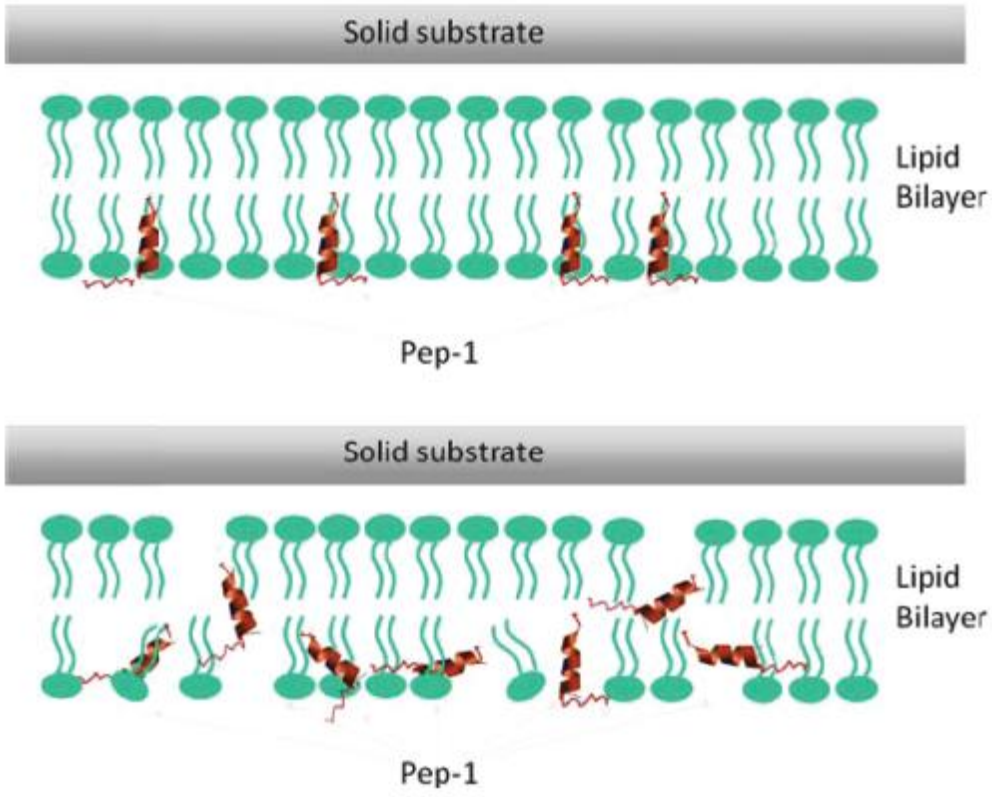

Figure 2.9 Schematics showing the interactions between lipid bilayers and Pep-1 with low or intermediate (a) and high (b) peptide concentrations.

2.4.2 The Effect of Lipid Bilayer Phase

SFG results show that on gel-phase lipid bilayers, Pep-1 molecules are loosely adsorbed on the surface with random or β-sheet type structures. On fluid-phase lipid bilayers, new peaks around 1653 cm^{-1} indicate the existence of α-helices. Previous CD studies have shown that in the range between 0.1 and 0.3 mg/mL, Pep-1 molecules in aqueous solution are poorly ordered,[16] but that range is three orders of magnitude larger than the concentrations studied in our experiments. Interestingly, here even at the low concentration of 0.28 μM, β-sheet type structures were detected on the POPG/POPG lipid bilayers. This implies that these β-sheet type structures are not a consequence of peptide aggregation, but rather perhaps an intermediate species in the

absorption process. It is the high fluidity of the lipid bilayer rather than the headgroups that will induce the formation and insertion of α-helices. Our results demonstrate that with SFG, it is possible to examine the translocation process from a molecular level.

2.4.3 Difference between CPPs and AMPs

CPPs and AMPs are both membrane-active peptides. The two classes of peptides share several characteristics such as charge, amphipathicity, helicity and length. CPPs have the capability to translocate biological membranes in a non-disruptive way, whereas AMPs can induce membrane permeabilization. The molecular mechanisms that underlie these differences in membrane interactions remain unclear.[68, 69] Our SFG studies on both types of peptides can shed light on how they differ in their interactions with membranes.

MSI-78 is a synthetic analog of magainin 2 with high antimicrobial activity. SFG results[42] showed that at the low concentration of 400 nM, MSI-78 molecules lie down on the surface of the negatively-charged gel-phase DPPG bilayer with ~70 ˚deviation from the membrane surface normal. When the concentration is increased to 600 nM, MSI-78 inserts into the membrane with a ~25˚tilt from the lipid bilayer normal. Multiple orientations were observed for an even higher peptide concentration, possibly indicating a toroidal-pore mechanism. This is an interesting contrast to studies on Pep-1, for which even at a low concentrations of 280 nM, the molecules were observed to insert into the fluid-phase POPG bilayer with α-helical structure. In gel-phase DPPG bilayers, Pep-1 does not form α-helices. This different performance from MSI-78 suggested that formation of α-helical structure in Pep-1 is induced by the fluid lipid chains in the hydrophobic interior of the bilayer rather than by interactions with the charged PG lipid headgroups. This agrees with the claim from previous research that CPPs are generally less amphipathic than AMPs.[12]

Alamethicin is an antibiotic peptide that can form voltage-gated ion channels in membranes. It interacts with cell membranes through the barrel-stave mode. SFG results[43] indicated that alamethicin molecules lie down on gel-phase bilayers but adopt a mixed α-helical and 3_{10}-helical structure in the fluid-phase bilayers. The α-helical component at the N-terminus tilts ~63˚ while 3_{10}-helical component at the C-terminus tilts ~43˚ versus the surface normal. Similar to Pep-1, alamethicin selectively forms α-helices in fluid-phase lipid bilayers, but not gel-phase lipid bilayers. However, there are also key differences. For Pep-1, signals from α-helical and β-sheet structures were observed simultaneously, although the magnitude of the β-sheet signals decreased as we increased the concentration of Pep-1. This shows that there is an equilibrium from the β-sheet type to the α-helical component in the Pep-1-membrane interface. However for alamethicin, such coexistence has not been observed.

2.5 Conclusion

In this study we expand the application of SFG studies on AMPs to CPPs. This work is our first step towards understanding the molecular interactions between CPPs and cell membranes. The effect of a membrane potential on CPP translocation will be investigated using SFG in the future. In addition, molecular interactions between cell membranes and CPPs with various molecular cargos (including small molecules, nanoparticles, proteins and DNAs) will be examined.

2.6 References

(1) Fernández-Carneado, J.; Kogan, M. J.; Pujals, S.; Giralt, E. *Biopolymers* **2004**, *76*, 196-203.

(2) Magzoub, M.; Gräslund, A. *Quart. Rev. Biophys.* **2004**, *37*, 147-195.

(3) Patel, L. N.; Zaro, J. L.; Shen, W.-C. *Pharmaceut. Res.* **2007**, *24*, 1977-1992.

(4) Vivès, E.; Schmidt, J.; Pèlegrin, A. *Biochim. Biophys. Acta* **2008**, *1786*, 126-138.

(5) Heitz, F.; Morris, M. C.; Divita, G. *Brit. J. Pharmacol.* **2009**, 195-206.

(6) Fonseca, S. B.; Pereira, M. P.; Kelley, S. O. *Adv. Drug Deliver. Rev.* **2009**, *61*, 953-964.

(7) Chugh, A.; Eudes, F.; Shim, Y.-S. *IUBMB Life* **2010**, *62*, 183-193.

(8) Moore, M. J.; Rosbash, M. *Adv. Sci.* **2001**, *294*, 1841-1842.

(9) Kumar, P.; Wu, H.; McBride, J. L.; Jung, K. -E.; Kim, M. H.; Davidson, B. L.; Lee, S. K.; Shankar, P.; Manjunath, N. *Nature* **2007**, *448*, 39-43.

(10) Muñoz-Morris, M. A.; Heitz, F.; Divita, G.; Morris, M. C. *Biochem. Biophys. Res. Commun.* **2007**, *355*, 877-882.

(11) Räägel, H.; Säälik, P.; Pooga, M. *Biochim. Biophys. Acta* **2010**, *1798*, 2240-2248.

(12) Herce, H. D.; Garcia, A. E. *J. Biol. Chem.* **2007**, *33*, 345-356.

(13) Morris, M. C.; Depollier, J.; Mery, J.; Heitz, F.; Divita, G. *Nature Biotech.* **2001**, *19*, 1173-1176.

(14) Deshayes, S.; Plénat, T.; Charnet, P.; Divita, G.; Molle, G.; Heitz, F. *Biochim. Biophys. Acta* **2006**, *1758*, 1846-1851.

(15) Gros, E.; Deshayes, S.; Morris, M. C.; Aldrian-Herrada, G.; Depollier, J.; Heitz, F.; Divita, G. *Biochim. Biophys. Acta* **2006**, *1758*, 384-393.

(16) Deshayes, S.; Heitz, A.; Morris, M. C.; Charnet, P.; Divita, G.; Heitz, F. *Biochemistry* **2004**, *43*, 1449-1457.

(17) Henriques, S. T.; Quintas, A.; Bagatolli, L. A; Homblé, F.; M. A. R. B. *Mol. Membr. Biol.* **2007**, *24*, 282-293.

(18) Ye, S.; Nguyen, K. T.; Le Clair, S. V.; Chen, Z. *J. Struct. Biol.* **2009**, *168*, 61-77.

(19) Wang, J.; Buck, S. M.; Even, M. A.; Chen, Z. *J. Am. Chem. Soc.* **2002**, *124*, 13302-13305.

(20) Wang, J.; Clarke, M. L.; Zhang, Y.; Chen, X.; Chen, Z. *Langmuir* **2003**, *19*, 7862-7866.

(21) Wang, J.; Even, M. a; Chen, X.; Schmaier, A. H.; Waite, J. H.; Chen, Z. *J. Am. Chem. Soc.* **2003**, *125*, 9914-9915.

(22) Chen, X.; Wang, J.; Sniadecki, J. J.; Even, M. A.; Chen, Z. *Langmuir* **2005**, 2662-2664.

(23) Wang, J.; Clarke, M., L.; Chen, X.; Even, M., A.; Johnson, W., C.; Chen, Z. *Surf. Sci.* **2005**, *587*, 1-11.

(24) Wang, J.; Paszti, Z.; Clarke, M. L.; Chen, X.; Chen, Z. *J. Phys. Chem. B* **2007**, *111*, 6088-6095.

(25) Wang, J.; Lee, S.-H.; Chen, Z. *J. Phys. Chem. B* **2008**, *112*, 2281-2290.

(26) Nguyen, K. T.; Le Clair, S. V.; Ye, S.; Chen, Z. *J. Phys. Chem. B* **2009**, *113*, 12358-12363.

(27) Nguyen, K. T.; King, J. T.; Chen, Z. *J. Phys. Chem. B* **2010**, *114*, 8291-8300.

(28) Boughton, A. P.; Andricioaei, I.; Chen, Z. *Langmuir* **2010**, *26*, 16031-16036.

(29) Chen, Z.; Ward, R.; Tian, Y.; Malizia, F.; Gracias, D. H.; Shen, Y. R.; Somorjai, G. A. *J. Biomed. Mater. Res.* **2002**, *62*, 254-264.

(30) Mermut, O.; Phillips, D. C.; York, R. L.; McCrea K., R.; Ward, R. S.; Somorjai, G. A. *J. Am. Chem. Soc.* **2006**, *128*, 3598-3607.

(31) Phillips, D. C.; York, R. L.; Mermut, O.; McCrea, K. R.; Ward, R. S.; Somorjai, G. A. *J. Phys. Chem. C* **2007**, *111*, 255-261.

(32) York, R. L.; Browne, W. K.; Geissler, P. L.; Somorjai, G. A. *Isr. J. Chem.* **2007**, *47*, 51-58.

(33) Weidner, T.; Apte, J. S.; Gamble, L. J.; Castner, D. G. *Langmuir* **2010**, *26*, 3433-3440.

(34) Baugh, L.; Weidner, T.; Baio, J. E.; Nguyen, P. C.; Gamble, L. J.; Stayton, P. S.; Castner, D. G. *Langmuir* **2010**, *26*, 16434-16441.

(35) Fu, L.; Ma, G.; Yan, E. C. *J. Am. Chem. Soc.* **2010**, *132*, 5405-5412.

(36) Anglin, T. C.; Liu, J.; Conboy, J. C. *Biophys. J.* **2007**, *92*, L01-L03.

(37) Anglin, T. C.; Brown, K. L.; Conboy, J. C. *J. Struct. Biol.* **2009**, *168*, 37-52.

(38) Jung, S.-Y.; Lim, S.-M.; Albertorio, F.; Kim, G.; Gurau, M. C.; Yang, R. D.; Holden, M. A.; Cremer, P. S. *J. Am. Chem. Soc.* **2003**, *125*, 12782-12786.

(39) Chen, X.; Sagle, L. B.; Cremer, P. S. *J. Am. Chem. Soc.* **2007**, *129*, 15104-15105.

(40) Hall, S. A.; Jena, K. C.; Trudeau, T. G.; Hore, D. K. *J. Phys. Chem. C* **2011**, 113, 15364-15372.

(41) Chen, X.; Chen, Z. *Biochim. Biophys. Acta* **2006**, *1758*, 1257-1273.

(42) Yang, P.; Ramamoorthy, A.; Chen, Z. *Langmuir* **2011**, *27*, 7760-7767.

(43) Ye, S.; Nguyen, K. T.; Chen, Z. *J. Phys. Chem. B* **2010**, *114*, 3334-3340.

(44) Chen, X.; Wang, J.; Boughton, A. P.; Kristalyn, C. B.; Chen, Z. *J. Am. Chem. Soc.* **2007**, *129*, 1420-1427.

(45) Henriques, T.; Castanho, M. A. R. B. *J. Pept. Sci.* **2008**, *1*, 482-487.

(46) Fittipaldi, A.; Ferrari, A.; Zoppé, M.; Arcangeli, C.; Pellegrini, V.; Beltram, F.; Giacca, M. *J. Biol. Chem.* **2003**, *278*, 34141-34149.

(47) Henriques, S. T.; Castanho, M. A. R. B. *Biochemistry* **2004**, *43*, 9716-9724.

(48) Shen, Y. *Nature*. **1989**, *337*, 519–525.

(49) Zhuang, X.; Miranda, P. B.; Kim, D.; Shen, Y. R. *Phys. Rev. B*. **1999**, *59*, 12632-12640.

(50) Chen, Z.; Shen, Y. R.; Somorjai, G. A. *Ann. Rev. Phys. Chem.* **2002**, *53*, 437-465.

(51) Eisenthal, K. B. *Chem. Rev*. **1996**, *96*, 1343-1360.

(52) Chen, Z. *Prog. Polym. Sci.* **2010**, *35*, 1376-1402.

(53) Chen, Z. *Polym. Inter*. **2007**, *56*, 577-587.

(54) Li, G.; Ye, S.; Morita, S.; Nishida, T.; Osawa, M. *J. Am. Chem. Soc*. **2004**, *126*, 12198 12199.

(55) Voges, A. B.; Al-Abadleh, H. A.; Musorrariti, M. J.; Bertin, P. A.; Nguyen, S. T.; Geiger, F. M. *J. Phys. Chem. B* **2004**, *108*, 18675-18682.

(56) Li, Q. F.; Hua, R.; Chea, I. J.; Chou, K. C. *J. Phys. Chem. B* **2008**, *112*, 694-697.

(57) Ye, H. K.; Gu, Z. Y.; Gracias, D. H. *Langmuir* **2006**, *22*, 1863-1868.

(58) Yatawara, A. K.; Tiruchinapally, G.; Bordenyuk, A. N.; Andreana, P. R.; Benderskii, A. V. *Langmuir* **2009**, *25*, 1901-1904.

(59) Moad, A. J.; Simpson, G. J. *J. Phys. Chem.* **2004**, *108*, 3548-3562.

(60) Moad, A. J.; Moad, C. W.; Perry, J. M.; Wampler, R. D.; Goeken, G. S.; Begue, N. J.; Shen, T.; Heiland, R.; Simpson, G. J. *J. Comp. Chem.* **2007**, *28*, 1996-2002.

(61) Tong, Y. J.; Li, N.; Liu, H. J.; Ge, A. L.; Osawa, M.; Ye, S. *Angew. Chem. Int. Ed.* **2010**, *49*, 2319-2323.

(62) Paszti, Z.; Guczi L. *Vib. Spectro.* **2009**, *50*, 48-56.

(63) Chen, X.; Wang, J.; Kristalyn, C. B.; Chen, Z. *Biophys. J.* **2007**, *93*, 866-875.

(64) Weller, K.; Lauber, S.; Lerch, M.; Renaud, a; Merkle, H. P.; Zerbe, O. *Biochemistry* **2005**, *44*, 15799-15811.

(65) Nguyen, K. T.; Le Clair, S. V.; Ye, S.; Chen, Z. *J. Phys. Chem. B* **2009**, *113*, 12169-12180.

(66) Henriques, S. T.; Castanho, M. A. R. B.; Pattenden, L. K.; Aguilar, M.-I. *J. Pept. Sci.* **2010**, *94*, 314-322.

(67) Deshayes, S.; Morris, M. C.; Divita, G.; Heitz, F. *Biochim. Biophys. Acta* **2006**, *1758*, 328-335.

(68) Henriques, S. T.; Melo, M. N.; Castanho, M. A. R. B. *Biochem. J.* **2006**, *399*, 1-7.

(69) Bobone, S.; Piazzon, A.; Orioni, B.; Pedersen, J. Z.; Nan, Y. H.; Hahm, K.-S.; Shin, S. Y.; Stella, L. *J. Pept. Sci.* **2011**, 335-341.

(70) Weidner, T.; Breen, N. F.; Drobny, G. P.; Castner, D. G. *J. Phys. Chem. B* **2009**, *113*, 15423-6.

(71) Unpublished data.

(72) Nguyen, K. T.; Soong, R.; Lm, S.-C.; Waskell, L.; Ramamoorthy, A.; Chen, Z. *J. Am. Chem. Soc.* **2010**, *132*, 15112-5.

CHAPTER 3

PHYSIOLOGICALLY-RELEVANT MODES OF MEMBRANE INTERACTIONS BY THE HUMAN ANTIMICROBIAL PEPTIDE, LL-37, REVEALED BY SFG EXPERIMENTS

The previous chapter studied a linear α-helical peptide, Pep-1. A previously developed SFG data analysis method was used to determine the Pep-1 membrane orientation. Many α-helices in peptide and large proteins may not be linear, but instead contain structural distortions. Unlike the linear peptide Pep-1, LL-37 is a bent α-helix that adopts different structures on different kinds of lipid membranes. LL-37 is an antimicrobial peptide (AMP), regarded as a potential source to solve bacterial antibiotic drug resistance issues.[1-9] In this chapter we developed SFG orientation analysis methodology to address the bend issue. Results from SFG experiments showed that LL-37 interacted with different lipid bilayers with different orientations. The conclusion was complemented by Surface Plasmon Resonance (SPR) experiments. This work shows that SFG can be used to study membrane orientations of bent helical structures. The work in this chapter has been published as: Ding, B.; Soblosky, L.; Nguyen, K.; Geng, J.; Yu, X.; Ramamoorthy, A.; Chen, Z. *Scientific Reports* **2013**, *3*, 1854. Z. C., A. R. and B. D. designed the project, analyzed the data and wrote the manuscript. B.D. performed SFG experiments and developed the data analysis method. L. S. prepared the cholesterol-related bilayer and

participated in cholesterol-related SFG experiments. K. N. did some initial SFG experiments on LL-37. J. G. and X. Y designed SPR experiments and collected SPR data.

3.1 Introduction

The development of drug resistance by many bacteria against traditional antibiotics poses an important challenge in curing infectious disease. Extensive research has been performed to develop antimicrobial peptides into powerful antibiotics to kill bacteria.[1-7] Because most antimicrobial peptides disrupt the cell membranes of bacteria, it is difficult for bacteria to develop drug resistance against antimicrobial peptides. However, the detailed interaction mechanisms between many antimicrobial peptides and bacterial cell membranes remain unclear.

LL-37, the only cathelicidin member in humans, plays an important role in human innate immunity system.[8,9] LL-37 exhibits a broad-spectrum antimicrobial activity and lipopolysaccharide-neutralizing effects. There is considerable therapeutic interest in utilizing LL-37 to overcome the bacterial resistance against traditional antibiotics and therefore there is significant interest in understanding its mechanism of antimicrobial action. Studies have reported the biological effects of LL-37 as well as the interactions of LL-37 with various types of lipid membranes. It was found that LL-37 readily disrupts the negative charged 1,2-dipalmitoyl-sn-glycero-3-phospho-(1'-rac-glycerol) (sodium salt) (DPPG) monolayer but exerts no effect on neutral charged 1,2-dipalmitoyl-sn-glycero-3-phosphocholine (DPPC) and 1,2-dipalmitoyl-sn-glycero-3-phosphoethanolamine (DPPE) monolayers by specular X-ray reflectivity.[10] NMR techniques have been used to determine 3D structures of LL-37 associated with neutral n-dodecylphosphocholine (DPC)[11] and negative-charged sodium dodecyl sulfate (SDS) micelles.[12] Although the peptide structures are not completely the same in these two environments, they

both feature a kink in the middle of the peptide. Solid-state NMR studies revealed the oligomerization[13], membrane orientation and carpet mechanism action for the peptide.[14] While solid-state NMR and calorimetric studies have provided insights into the mechanism of antimicrobial action for LL-37, obtaining such information at very low, physiologically relevant concentrations have not been achieved due to the low sensitivity of the two techniques. Methods to overcome this low concentration limitation not only can be used to study other AMPs but also other membrane active peptides/proteins including cell penetrating peptides and amyloid proteins.

In this chapter, we demonstrate the power of the sum frequency generation (SFG) vibrational spectroscopic technique to study the interactions between LL-37 and a single lipid bilayer containing different ratios of negative-charged 1-palmitoyl-2-oleoyl-sn-glycero-3-phosphoglycerol (POPG), neutral-charged 1-palmitoyl-2-oleoyl-sn-glycero-3-phosphocholine (POPC), and cholesterol for various peptide concentrations. As discussed in the previous chapters, SFG spectroscopy is an intrinsic surface-sensitive technique[15-22] and has been widely used to study the structure and orientation of peptides and proteins at bio-interfaces[23-27]. Because of the excellent sensitivity, SFG can be used to investigate peptide-membrane interactions in the physiologically-relevant peptide concentration range, which cannot be done using most other biophysical techniques.[28-31]

Most of the previous orientation studies on α-helical peptides using SFG were focused on the linear α-helical structure.[32,33] For peptides that are not linear, data analysis on linear peptides was still used to determine orientation.[34] Here, we studied a non-linear α-helical structure using SFG and for the first time developed approaches to analyze SFG data detected from such bent helical structures. We considered two types of non-linear α-helical structures in this study: a bent structure and a disrupted structure. The bent structure changes in the helix axis direction with all

the residues remaining helical, an example of which is LL-37 associated with SDS vesicles.[11] The disrupted structure also bears a change in the axial direction but with a loss of the helical character of the residues around the kink location, such as melittin, alamethicin and LL-37 associated with DPC vesicles[12]. For both "bend and disruption" models, we treat the helical part of the peptide as two adjacent segments. The way we treat the first segment is the same as for an ideal linear helix previously reported,[32,33] but the calculation for the second segment is different for the above two models. For the bend model, since there is no random structure between the two segments, we ought to consider that the entire helical LL-37 structure is continuous. Especially, there is a phase term involved in the calculation of the E1 vibrational mode which should also be continuous for the entire LL-37 helical structure. On the contrary, the phases for the vibrations of the two segments in the disrupted structure are unrelated and we do not consider the phase continuation. More calculation details (i.e. the values for the dipole moments and the Raman tensors) are included in section 3.2 below. The peptide membrane orientation deduced using SFG has been compared to results from NMR studies. Our results demonstrate that at the high peptide concentrations, SFG results are compatible to the NMR data. Different from NMR, SFG has the capability to investigate very low concentrations of complex α-helical structures and their membrane orientations.

3.2. Experimental Procedure

3.2.1 Experimental Details

LL-37 (sequence: LLGDFFRKSKEKIGKEFKRIVQRIKDFLRNLVPRTES) was purchased from Anaspec with >95% purity. The POPC and POPG lipids were purchased from Avanti Polar Lipids Inc. (Alabaster, AL).

Lipid bilayers were deposited on CaF_2 right angle prisms (Altos Photonics, Bozeman, MT) by Langmuir-Blodgett and Langmuir-Schaefer (LB/LS) methods and the CaF_2 substrates were cleaned as described in Chapter 2 before use. Ultrapure water from a Millipore system (Millipore, Bedford, MA) was used throughout the experiments for bilayer and sample preparation. The bilayer was immersed in water inside a 2 mL reservoir during the experiment. 4 μL and 14 μL of 1 mg/mL LL-37 aqueous solutions were injected into the reservoir to achieve final peptide concentrations of 460 nM and 1.6 μM respectively. A magnetic microstirrer was used at a spinning rate of 100 rpm to ensure the peptide bulk solution is homogeneous below the bilayer. The absorption time for the POPG system at 460 nM is ~1500 s and at 1.6 μM is ~250 s.

The details of our SFG setup with near-total reflection geometry have been previously described and will not be repeated. SFG Spectra were collected from the lipid bilayer in contact with the LL-37 solution in ssp (s-SFG, s-visible, p-IR) and ppp polarization combinations in the amide I frequency region (1500 cm^{-1} to 1800 cm^{-1}), and in the ssp polarization combination only in the high frequency region (2700 cm^{-1} to 4000 cm^{-1}).

3.2.2 Two Models for Calculating the Hyperpolarizability

Turns and kinks are ubiquitous in α-helical and β-sheet structures. [39] They cause structural complexities while at the same time contribute to the diversity of biological functions. Although it is well-known that membrane-associated α-helices may be kinked, there is disagreement in the nature and underlying causes of the kinked structures.[40] It was shown in the literature that kinks in α-helical transmembrane regions facilitate the conformational rearrangement and structural variability which make kinks important in biological functions. [3] Recently Rainey et al. developed a Monte Carlo method based simulation algorithm to determine

the angles of the kinks by finding the helical axes. They categorized kinks as either bends or disruptions.[40] As we discussed above, bent structure changes in the helix axis direction with all the residues remaining helical, an example of which is LL-37 associated with SDS vesicles.[12] Disrupted structure also bears a change in the axial direction but with a loss of helical character of the residues around the kink location, such as melittin, alamethicin and LL-37 associated with DPC vesicles[11]. Here we illustrate how we perform SFG data analysis on these two models

3.2.2.1 The Bend Model

Here we first discuss the calculation of the IR transition dipole moment. For the first segment of LL-37 which is a linear helix, we adopted the same model to do the calculation as we did in a previous paper.[33] The results as well as the calculation equation for the A mode and E1 mode are listed below. It is more complicated to calculate the second α-helical segment of LL-37. Firstly, we need to consider the bent angle between the two segments. Secondly, since there is no random structure between the two segments, we ought to consider that the entire helical LL-37 structure is continuous. Especially, there is a phase term involved in the calculation of the E1 mode, which should also be continuous for the entire LL-37 structure. The overall IR transition dipole of the bent LL-37 was calculated with the first segment of 16 residues and the second segment of 14 residues, and with 143 degrees between the two segments, as an example.

Similar to the calculation of the IR transition dipole, the Raman polarizability tensor for the first segment can be calculated with the same parameters as discussed in Chapter 1. The Raman polarizability tensor results for both A and E1 modes are also listed below. For the second segment, also similar to the IR transition dipole calculation, we need to consider the structure and phase continuation.

For the bend model (LL-37 on POPG lipid bilayers), the details on calculating the LL-37 IR dipole transition moment and Raman polarizability tensor are shown below:

The dipole transition moment for the first segment:

A mode:

$$\sum_{k=0}^{15}\left[\begin{pmatrix}\cos\left(2\pi\cdot\frac{100\cdot k}{360}\right) & \sin\left(2\pi\cdot\frac{100\cdot k}{360}\right) & 0\\ -\sin\left(2\pi\cdot\frac{100\cdot k}{360}\right) & \cos\left(2\pi\cdot\frac{100\cdot k}{360}\right) & 0\\ 0 & 0 & 1\end{pmatrix}^{T}\cdot\begin{pmatrix}\sin\left(2\pi\cdot\frac{42}{360}\right)\\ 0\\ \cos\left(2\pi\cdot\frac{42}{360}\right)\end{pmatrix}\right]=\begin{pmatrix}0.745\\ 0.43\\ 11.89\end{pmatrix} \tag{2}$$

E1 mode:

$$\sum_{k=0}^{15}\left[\begin{pmatrix}\cos\left(2\pi\cdot\frac{100\cdot k}{360}\right) & \sin\left(2\pi\cdot\frac{100\cdot k}{360}\right) & 0\\ -\sin\left(2\pi\cdot\frac{100\cdot k}{360}\right) & \cos\left(2\pi\cdot\frac{100\cdot k}{360}\right) & 0\\ 0 & 0 & 1\end{pmatrix}^{T}\cdot\begin{pmatrix}\sin\left(2\pi\cdot\frac{42}{360}\right)\\ 0\\ \cos\left(2\pi\cdot\frac{42}{360}\right)\end{pmatrix}\cdot e^{i\cdot\frac{100k\,\pi}{180}}\right]=\begin{pmatrix}5.411+0.101i\\ 0.101+5.295i\\ 0.827+0.478i\end{pmatrix} \tag{3}$$

$$\sum_{k=0}^{15}\left[\begin{pmatrix}\cos\left(2\pi\cdot\frac{100\cdot k}{360}\right) & \sin\left(2\pi\cdot\frac{100\cdot k}{360}\right) & 0\\ -\sin\left(2\pi\cdot\frac{100\cdot k}{360}\right) & \cos\left(2\pi\cdot\frac{100\cdot k}{360}\right) & 0\\ 0 & 0 & 1\end{pmatrix}^{T}\cdot\begin{pmatrix}\sin\left(2\pi\cdot\frac{42}{360}\right)\\ 0\\ \cos\left(2\pi\cdot\frac{42}{360}\right)\end{pmatrix}\cdot e^{-i\cdot\frac{100k\,\pi}{180}}\right]=\begin{pmatrix}5.411-0.101i\\ 0.101-5.295i\\ 0.827-0.478i\end{pmatrix} \tag{4}$$

The dipole transition moment for the second segment is:

A mode:

$$\sum_{k=16}^{29}\left[\begin{pmatrix}\cos\left(2\pi\cdot\frac{37}{360}\right) & 0 & -\sin\left(2\pi\cdot\frac{37}{360}\right)\\ 0 & 1 & 0\\ \sin\left(2\pi\cdot\frac{37}{360}\right) & 0 & \cos\left(2\pi\cdot\frac{37}{360}\right)\end{pmatrix}\begin{pmatrix}\cos\left(2\pi\cdot\frac{100\cdot k}{360}\right) & \sin\left(2\pi\cdot\frac{100\cdot k}{360}\right) & 0\\ -\sin\left(2\pi\cdot\frac{100\cdot k}{360}\right) & \cos\left(2\pi\cdot\frac{100\cdot k}{360}\right) & 0\\ 0 & 0 & 1\end{pmatrix}^{T}\cdot\begin{pmatrix}\sin\left(2\pi\cdot\frac{42}{360}\right)\\ 0\\ \cos\left(2\pi\cdot\frac{42}{360}\right)\end{pmatrix}\right]=\begin{pmatrix}-6.261\\ -0.299\\ 8.309\end{pmatrix}$$

(5)

E1 mode:

$$\sum_{k=16}^{29}\left[\left[\begin{pmatrix}\cos\left(2\pi\cdot\frac{37}{360}\right) & 0 & -\sin\left(2\pi\cdot\frac{37}{360}\right)\\ 0 & 1 & 0\\ \sin\left(2\pi\cdot\frac{37}{360}\right) & 0 & \cos\left(2\pi\cdot\frac{37}{360}\right)\end{pmatrix}\begin{pmatrix}\cos\left(2\pi\cdot\frac{100\cdot k}{360}\right) & \sin\left(2\pi\cdot\frac{100\cdot k}{360}\right) & 0\\ -\sin\left(2\pi\cdot\frac{100\cdot k}{360}\right) & \cos\left(2\pi\cdot\frac{100\cdot k}{360}\right) & 0\\ 0 & 0 & 1\end{pmatrix}^{T}\cdot\begin{pmatrix}\sin\left(2\pi\cdot\frac{42}{360}\right)\\ 0\\ \cos\left(2\pi\cdot\frac{42}{360}\right)\end{pmatrix}\right]\cdot e^{i\cdot\frac{100k\,\pi}{180}}\right]=\begin{pmatrix}3.915+0.2i\\ 4.466i\\ 2.95-0.265i\end{pmatrix}$$

(6)

$$\sum_{k=16}^{29}\left[\left[\begin{pmatrix}\cos\left(2\pi\cdot\frac{37}{360}\right) & 0 & -\sin\left(2\pi\cdot\frac{37}{360}\right)\\ 0 & 1 & 0\\ \sin\left(2\pi\cdot\frac{37}{360}\right) & 0 & \cos\left(2\pi\cdot\frac{37}{360}\right)\end{pmatrix}\begin{pmatrix}\cos\left(2\pi\cdot\frac{100\cdot k}{360}\right) & \sin\left(2\pi\cdot\frac{100\cdot k}{360}\right) & 0\\ -\sin\left(2\pi\cdot\frac{100\cdot k}{360}\right) & \cos\left(2\pi\cdot\frac{100\cdot k}{360}\right) & 0\\ 0 & 0 & 1\end{pmatrix}^{T}\cdot\begin{pmatrix}\sin\left(2\pi\cdot\frac{42}{360}\right)\\ 0\\ \cos\left(2\pi\cdot\frac{42}{360}\right)\end{pmatrix}\right]\cdot\left|e^{-i\cdot\frac{100k\,\pi}{180}}\right|\right]=\begin{pmatrix}3.915-0.2i\\ -4.466i\\ 2.95+0.265i\end{pmatrix}$$

(7)

The Raman tensor for the first segment is:

A mode:

$$\sum_{k=0}^{15}\left[\begin{pmatrix}\cos\left(2\pi\cdot\frac{100\cdot k}{360}\right) & \sin\left(2\pi\cdot\frac{100\cdot k}{360}\right) & 0\\ -\sin\left(2\pi\cdot\frac{100\cdot k}{360}\right) & \cos\left(2\pi\cdot\frac{100\cdot k}{360}\right) & 0\\ 0 & 0 & 1\end{pmatrix}^{T}\cdot\begin{pmatrix}0.624 & 0 & 0.4\\ 0 & 0.05 & 0\\ 0.4 & 0 & 0.577\end{pmatrix}\cdot\begin{pmatrix}\cos\left(2\pi\cdot\frac{100\cdot k}{360}\right) & \sin\left(2\pi\cdot\frac{100\cdot k}{360}\right) & 0\\ -\sin\left(2\pi\cdot\frac{100\cdot k}{360}\right) & \cos\left(2\pi\cdot\frac{100\cdot k}{360}\right) & 0\\ 0 & 0 & 1\end{pmatrix}\right]=$$

$$\begin{pmatrix}5.442 & 0.086 & 0.445\\ 0.086 & 5.342 & 0.257\\ 0.445 & 0.257 & 9.232\end{pmatrix}$$

(8)

E1 mode:

$$\sum_{k=0}^{15}\left[\begin{pmatrix}\cos\left(2\pi\cdot\frac{100\cdot k}{360}\right) & \sin\left(2\pi\cdot\frac{100\cdot k}{360}\right) & 0\\ -\sin\left(2\pi\cdot\frac{100\cdot k}{360}\right) & \cos\left(2\pi\cdot\frac{100\cdot k}{360}\right) & 0\\ 0 & 0 & 1\end{pmatrix}^{T}\cdot\begin{pmatrix}0.624 & 0 & 0.4\\ 0 & 0.05 & 0\\ 0.4 & 0 & 0.577\end{pmatrix}\cdot\begin{pmatrix}\cos\left(2\pi\cdot\frac{100\cdot k}{360}\right) & \sin\left(2\pi\cdot\frac{100\cdot k}{360}\right) & 0\\ -\sin\left(2\pi\cdot\frac{100\cdot k}{360}\right) & \cos\left(2\pi\cdot\frac{100\cdot k}{360}\right) & 0\\ 0 & 0 & 1\end{pmatrix}\cdot\begin{pmatrix}e^{i\cdot\frac{100k\,\pi}{180}} & 0 & 0\\ 0 & e^{i\cdot\frac{100k\cdot\pi}{180}} & 0\\ 0 & 0 & e^{i\cdot\frac{100k\cdot\pi}{180}}\end{pmatrix}\right]=\begin{pmatrix}0.535-0.124i & -0.156+0.16i & 3.235+0.06i\\ -0.156+0.16i & 0.215+0.557i & 0.06+3.165i\\ 3.235+0.06i & 0.06+3.165i & 0.642+0.371i\end{pmatrix}$$

(9)

$$\sum_{k=0}^{15}\left[\begin{pmatrix}\cos\left(2\pi\cdot\frac{100\cdot k}{360}\right) & \sin\left(2\pi\cdot\frac{100\cdot k}{360}\right) & 0\\ -\sin\left(2\pi\cdot\frac{100\cdot k}{360}\right) & \cos\left(2\pi\cdot\frac{100\cdot k}{360}\right) & 0\\ 0 & 0 & 1\end{pmatrix}^{T}\cdot\begin{pmatrix}0.624 & 0 & 0.4\\ 0 & 0.05 & 0\\ 0.4 & 0 & 0.577\end{pmatrix}\cdot\begin{pmatrix}\cos\left(2\pi\cdot\frac{100\cdot k}{360}\right) & \sin\left(2\pi\cdot\frac{100\cdot k}{360}\right) & 0\\ -\sin\left(2\pi\cdot\frac{100\cdot k}{360}\right) & \cos\left(2\pi\cdot\frac{100\cdot k}{360}\right) & 0\\ 0 & 0 & 1\end{pmatrix}\cdot\right.$$

$$\left[\begin{pmatrix} e^{-i\cdot\frac{100k\,\pi}{180}} & 0 & 0 \\ 0 & e^{-i\cdot\frac{100k\cdot\pi}{180}} & 0 \\ 0 & 0 & e^{-i\cdot\frac{100k\cdot\pi}{180}} \end{pmatrix}\right] = \begin{pmatrix} 0.535 + 0.124i & -0.156 - 0.16i & 3.235 - 0.06i \\ -0.156 - 0.16i & 0.215 - 0.557i & 0.06 - 3.165i \\ 3.235 - 0.06i & 0.06 - 3.165i & 0.642 - 0.371i \end{pmatrix} \tag{10}$$

The Raman tensor for the second segment is:

A mode:

$$\sum_{k=16}^{29}\left[\begin{pmatrix} \cos\left(2\pi\cdot\frac{37}{360}\right) & 0 & -\sin\left(2\pi\cdot\frac{37}{360}\right) \\ 0 & 1 & 0 \\ \sin\left(2\pi\cdot\frac{37}{360}\right) & 0 & \cos\left(2\pi\cdot\frac{37}{360}\right) \end{pmatrix}\begin{pmatrix} \cos\left(2\pi\cdot\frac{100\cdot k}{360}\right) & \sin\left(2\pi\cdot\frac{100\cdot k}{360}\right) & 0 \\ -\sin\left(2\pi\cdot\frac{100\cdot k}{360}\right) & \cos\left(2\pi\cdot\frac{100\cdot k}{360}\right) & 0 \\ 0 & 0 & 1 \end{pmatrix}^{T}\cdot\begin{pmatrix} 0.624 & 0 & 0.4 \\ 0 & 0.05 & 0 \\ 0.4 & 0 & 0.577 \end{pmatrix}\cdot$$

$$\begin{pmatrix} \cos\left(2\pi\cdot\frac{100\cdot k}{360}\right) & \sin\left(2\pi\cdot\frac{100\cdot k}{360}\right) & 0 \\ -\sin\left(2\pi\cdot\frac{100\cdot k}{360}\right) & \cos\left(2\pi\cdot\frac{100\cdot k}{360}\right) & 0 \\ 0 & 0 & 1 \end{pmatrix}\cdot\begin{pmatrix} \cos\left(2\pi\cdot\frac{37}{360}\right) & 0 & -\sin\left(2\pi\cdot\frac{37}{360}\right) \\ 0 & 1 & 0 \\ \sin\left(2\pi\cdot\frac{37}{360}\right) & 0 & \cos\left(2\pi\cdot\frac{37}{360}\right) \end{pmatrix}^{T}\Bigg] = \begin{pmatrix} 6.054 & 0.107 & -1.525 \\ 0.107 & 4.531 & -0.143 \\ -1.525 & -0.143 & 6.929 \end{pmatrix} \tag{11}$$

E1 mode:

$$\sum_{k=16}^{29}\left[\begin{pmatrix} \cos\left(2\pi\cdot\frac{37}{360}\right) & 0 & -\sin\left(2\pi\cdot\frac{37}{360}\right) \\ 0 & 1 & 0 \\ \sin\left(2\pi\cdot\frac{37}{360}\right) & 0 & \cos\left(2\pi\cdot\frac{37}{360}\right) \end{pmatrix}\begin{pmatrix} \cos\left(2\pi\cdot\frac{100\cdot k}{360}\right) & \sin\left(2\pi\cdot\frac{100\cdot k}{360}\right) & 0 \\ -\sin\left(2\pi\cdot\frac{100\cdot k}{360}\right) & \cos\left(2\pi\cdot\frac{100\cdot k}{360}\right) & 0 \\ 0 & 0 & 1 \end{pmatrix}^{T}\cdot\begin{pmatrix} 0.624 & 0 & 0.4 \\ 0 & 0.05 & 0 \\ 0.4 & 0 & 0.577 \end{pmatrix}\cdot$$

$$\left(\begin{matrix}\cos\left(2\pi\cdot\frac{100\cdot k}{360}\right) & \sin\left(2\pi\cdot\frac{100\cdot k}{360}\right) & 0\\ -\sin\left(2\pi\cdot\frac{100\cdot k}{360}\right) & \cos\left(2\pi\cdot\frac{100\cdot k}{360}\right) & 0\\ 0 & 0 & 1\end{matrix}\right)\cdot\left(\begin{matrix}\cos\left(2\pi\cdot\frac{37}{360}\right) & 0 & -\sin\left(2\pi\cdot\frac{37}{360}\right)\\ 0 & 1 & 0\\ \sin\left(2\pi\cdot\frac{37}{360}\right) & 0 & \cos\left(2\pi\cdot\frac{37}{360}\right)\end{matrix}\right)^{T}\cdot$$

$$\left(\begin{matrix}e^{i\cdot\frac{100k\,\pi}{180}} & 0 & 0\\ 0 & e^{i\cdot\frac{100k\cdot\pi}{180}} & 0\\ 0 & 0 & e^{i\cdot\frac{100k\cdot\pi}{180}}\end{matrix}\right)\Bigg]=\left(\begin{matrix}-2.817+0.01i & 0.147-1.607i & 0.808+0.202i\\ 0.147-1.607i & -0.463i & 0.111+2.132i\\ 0.808+0.202i & 0.111+2.132i & 2.817-0.106i\end{matrix}\right) \tag{12}$$

$$\sum_{k=16}^{29}\left[\left(\begin{matrix}\cos\left(2\pi\cdot\frac{37}{360}\right) & 0 & -\sin\left(2\pi\cdot\frac{37}{360}\right)\\ 0 & 1 & 0\\ \sin\left(2\pi\cdot\frac{37}{360}\right) & 0 & \cos\left(2\pi\cdot\frac{37}{360}\right)\end{matrix}\right)\left(\begin{matrix}\cos\left(2\pi\cdot\frac{100\cdot k}{360}\right) & \sin\left(2\pi\cdot\frac{100\cdot k}{360}\right) & 0\\ -\sin\left(2\pi\cdot\frac{100\cdot k}{360}\right) & \cos\left(2\pi\cdot\frac{100\cdot k}{360}\right) & 0\\ 0 & 0 & 1\end{matrix}\right)^{T}\cdot\left(\begin{matrix}0.624 & 0 & 0.4\\ 0 & 0.05 & 0\\ 0.4 & 0 & 0.577\end{matrix}\right)\cdot\right.$$

$$\left(\begin{matrix}\cos\left(2\pi\cdot\frac{100\cdot k}{360}\right) & \sin\left(2\pi\cdot\frac{100\cdot k}{360}\right) & 0\\ -\sin\left(2\pi\cdot\frac{100\cdot k}{360}\right) & \cos\left(2\pi\cdot\frac{100\cdot k}{360}\right) & 0\\ 0 & 0 & 1\end{matrix}\right)\cdot\left(\begin{matrix}\cos\left(2\pi\cdot\frac{37}{360}\right) & 0 & -\sin\left(2\pi\cdot\frac{37}{360}\right)\\ 0 & 1 & 0\\ \sin\left(2\pi\cdot\frac{37}{360}\right) & 0 & \cos\left(2\pi\cdot\frac{37}{360}\right)\end{matrix}\right)^{T}$$

$$\left[\begin{pmatrix} e^{-i\cdot\frac{100k\,\pi}{180}} & 0 & 0 \\ 0 & e^{-i\cdot\frac{100k\cdot\pi}{180}} & 0 \\ 0 & 0 & e^{-i\cdot\frac{100k\cdot\pi}{180}} \end{pmatrix}\right] = \begin{pmatrix} -2.817 - 0.01i & 0.147 + 1.607i & 0.808 - 0.202i \\ 0.147 + 1.607i & 0.463i & 0.111 - 2.132i \\ 0.808 - 0.202i & 0.111 - 2.132i & 2.817 + 0.106i \end{pmatrix} \tag{13}$$

3.2.2.2 The Disruption Model

The difference between a disrupted kink and a bent structure is that there is a random-coil structure between the two α-helical segments of a disrupted kink structure while the bent structure is continuous. We can adopt the similar method to deduce the orientation dependent second order nonlinear optical susceptibility components for disrupted LL-37 structure with some variations. The variation is that in a disrupted kink structure, the phases for the vibrations of the two segments are unrelated and we do not consider the phase continuation.

For the disruption model (LL-37 on POPC lipid bilayers), the overall transition dipole moment and Raman Polarizability with 21 residues for the first segment and 7 residues for the second segment can then be calculated and listed below.

The dipole transition moment for the first segment is:

A mode:

$$\sum_{k=0}^{20}\left[\begin{pmatrix} \cos\left(2\pi\cdot\frac{100\cdot k}{360}\right) & \sin\left(2\pi\cdot\frac{100\cdot k}{360}\right) & 0 \\ -\sin\left(2\pi\cdot\frac{100\cdot k}{360}\right) & \cos\left(2\pi\cdot\frac{100\cdot k}{360}\right) & 0 \\ 0 & 0 & 1 \end{pmatrix}^{T}\cdot\begin{pmatrix} \sin\left(2\pi\cdot\frac{42}{360}\right) \\ 0 \\ \cos\left(2\pi\cdot\frac{42}{360}\right) \end{pmatrix}\right] = \begin{pmatrix} -0.076 \\ 0.43 \\ 15.606 \end{pmatrix} \tag{14}$$

E1 mode:

$$\sum_{k=0}^{20}\left[\begin{pmatrix}\cos\left(2\pi\cdot\frac{100\cdot k}{360}\right) & \sin\left(2\pi\cdot\frac{100\cdot k}{360}\right) & 0\\ -\sin\left(2\pi\cdot\frac{100\cdot k}{360}\right) & \cos\left(2\pi\cdot\frac{100\cdot k}{360}\right) & 0\\ 0 & 0 & 1\end{pmatrix}^{T}\cdot\begin{pmatrix}\sin\left(2\pi\cdot\frac{42}{360}\right)\\ 0\\ \cos\left(2\pi\cdot\frac{42}{360}\right)\end{pmatrix}\cdot e^{i\cdot\frac{100k\,\pi}{180}}\right]=\begin{pmatrix}7.302+0.101i\\ 0.101+6.749i\\ -0.084+0.478i\end{pmatrix} \tag{15}$$

$$\sum_{k=0}^{20}\left[\begin{pmatrix}\cos\left(2\pi\cdot\frac{100\cdot k}{360}\right) & \sin\left(2\pi\cdot\frac{100\cdot k}{360}\right) & 0\\ -\sin\left(2\pi\cdot\frac{100\cdot k}{360}\right) & \cos\left(2\pi\cdot\frac{100\cdot k}{360}\right) & 0\\ 0 & 0 & 1\end{pmatrix}^{T}\cdot\begin{pmatrix}\sin\left(2\pi\cdot\frac{42}{360}\right)\\ 0\\ \cos\left(2\pi\cdot\frac{42}{360}\right)\end{pmatrix}\cdot e^{-i\cdot\frac{100k\,\pi}{180}}\right]=\begin{pmatrix}7.302-0.101i\\ 0.101-6.749i\\ -0.084-0.478i\end{pmatrix} \tag{16}$$

The dipole transition moment for the second segment is:

A mode:

$$\sum_{k=21}^{27}\left[\begin{pmatrix}\cos\left(2\pi\cdot\frac{60}{360}\right) & 0 & -\sin\left(2\pi\cdot\frac{60}{360}\right)\\ 0 & 1 & 0\\ \sin\left(2\pi\cdot\frac{60}{360}\right) & 0 & \cos\left(2\pi\cdot\frac{60}{360}\right)\end{pmatrix}\begin{pmatrix}\cos\left(2\pi\cdot\frac{100\cdot k}{360}\right) & \sin\left(2\pi\cdot\frac{100\cdot k}{360}\right) & 0\\ -\sin\left(2\pi\cdot\frac{100\cdot k}{360}\right) & \cos\left(2\pi\cdot\frac{100\cdot k}{360}\right) & 0\\ 0 & 0 & 1\end{pmatrix}^{T}\cdot\begin{pmatrix}\sin\left(2\pi\cdot\frac{42}{360}\right)\\ 0\\ \cos\left(2\pi\cdot\frac{42}{360}\right)\end{pmatrix}\right]=\begin{pmatrix}-4.467\\ 0.131\\ 2.667\end{pmatrix} \tag{17}$$

E1 mode:

$$\sum_{k=21}^{27}\left[\left[\begin{pmatrix}\cos\left(2\pi\cdot\frac{60}{360}\right) & 0 & -\sin\left(2\pi\cdot\frac{60}{360}\right)\\ 0 & 1 & 0\\ \sin\left(2\pi\cdot\frac{60}{360}\right) & 0 & \cos\left(2\pi\cdot\frac{60}{360}\right)\end{pmatrix}\begin{pmatrix}\cos\left(2\pi\cdot\frac{100\cdot k}{360}\right) & \sin\left(2\pi\cdot\frac{100\cdot k}{360}\right) & 0\\ -\sin\left(2\pi\cdot\frac{100\cdot k}{360}\right) & \cos\left(2\pi\cdot\frac{100\cdot k}{360}\right) & 0\\ 0 & 0 & 1\end{pmatrix}^{T}\cdot\begin{pmatrix}\sin\left(2\pi\cdot\frac{42}{360}\right)\\ 0\\ \cos\left(2\pi\cdot\frac{42}{360}\right)\end{pmatrix}\right]\cdot\right.$$

$$\left[e^{i\cdot\frac{100(k-21)\pi}{180}}\right] = \begin{pmatrix} 0.717 + 0.888i \\ -2.028 + 1.055i \\ 1.073 + 1.829i \end{pmatrix} \tag{18}$$

$$\sum_{k=21}^{27}\left[\left[\begin{pmatrix} \cos\left(2\pi\cdot\frac{60}{360}\right) & 0 & -\sin\left(2\pi\cdot\frac{60}{360}\right) \\ 0 & 1 & 0 \\ \sin\left(2\pi\cdot\frac{60}{360}\right) & 0 & \cos\left(2\pi\cdot\frac{60}{360}\right) \end{pmatrix}\begin{pmatrix} \cos\left(2\pi\cdot\frac{100\cdot k}{360}\right) & \sin\left(2\pi\cdot\frac{100\cdot k}{360}\right) & 0 \\ -\sin\left(2\pi\cdot\frac{100\cdot k}{360}\right) & \cos\left(2\pi\cdot\frac{100\cdot k}{360}\right) & 0 \\ 0 & 0 & 1 \end{pmatrix}^{T}\cdot\begin{pmatrix} \sin\left(2\pi\cdot\frac{42}{360}\right) \\ 0 \\ \cos\left(2\pi\cdot\frac{42}{360}\right) \end{pmatrix}\right]\cdot\left[e^{-i\cdot\frac{100(k-21)\pi}{180}}\right] = \begin{pmatrix} 0.717 - 0.888i \\ -2.028 - 1.055i \\ 1.073 - 1.829i \end{pmatrix} \tag{19}$$

The Raman tensor for the first segment is:

A mode:

$$\sum_{k=0}^{20}\left[\begin{pmatrix} \cos\left(2\pi\cdot\frac{100\cdot k}{360}\right) & \sin\left(2\pi\cdot\frac{100\cdot k}{360}\right) & 0 \\ -\sin\left(2\pi\cdot\frac{100\cdot k}{360}\right) & \cos\left(2\pi\cdot\frac{100\cdot k}{360}\right) & 0 \\ 0 & 0 & 1 \end{pmatrix}^{T}\cdot\begin{pmatrix} 0.624 & 0 & 0.4 \\ 0 & 0.05 & 0 \\ 0.4 & 0 & 0.577 \end{pmatrix}\cdot\begin{pmatrix} \cos\left(2\pi\cdot\frac{100\cdot k}{360}\right) & \sin\left(2\pi\cdot\frac{100\cdot k}{360}\right) & 0 \\ -\sin\left(2\pi\cdot\frac{100\cdot k}{360}\right) & \cos\left(2\pi\cdot\frac{100\cdot k}{360}\right) & 0 \\ 0 & 0 & 1 \end{pmatrix}\right] =$$

$$\begin{pmatrix} 7.314 & 0.086 & -0.045 \\ 0.086 & 6.84 & 0.257 \\ -0.045 & 0.257 & 12.117 \end{pmatrix} \tag{20}$$

E1 mode:

$$\sum_{k=0}^{20}\left[\begin{pmatrix}\cos\left(2\pi\cdot\frac{100\cdot k}{360}\right) & \sin\left(2\pi\cdot\frac{100\cdot k}{360}\right) & 0\\ -\sin\left(2\pi\cdot\frac{100\cdot k}{360}\right) & \cos\left(2\pi\cdot\frac{100\cdot k}{360}\right) & 0\\ 0 & 0 & 1\end{pmatrix}^{T}\cdot\begin{pmatrix}0.624 & 0 & 0.4\\ 0 & 0.05 & 0\\ 0.4 & 0 & 0.577\end{pmatrix}\cdot\begin{pmatrix}\cos\left(2\pi\cdot\frac{100\cdot k}{360}\right) & \sin\left(2\pi\cdot\frac{100\cdot k}{360}\right) & 0\\ -\sin\left(2\pi\cdot\frac{100\cdot k}{360}\right) & \cos\left(2\pi\cdot\frac{100\cdot k}{360}\right) & 0\\ 0 & 0 & 1\end{pmatrix}\cdot\begin{pmatrix}e^{i\cdot\frac{100k\,\pi}{180}} & 0 & 0\\ 0 & e^{i\cdot\frac{100k\cdot\pi}{180}} & 0\\ 0 & 0 & e^{i\cdot\frac{100k\cdot\pi}{180}}\end{pmatrix}\right]=\begin{pmatrix}0.089-0.124i & -0.156-0.16i & 4.365+0.06i\\ -0.156-0.16i & -0.165+0.557i & 0.06+4.035i\\ 4.365+0.06i & 0.06+4.035i & -0.065+0.371i\end{pmatrix} \tag{21}$$

$$\sum_{k=0}^{20}\left[\begin{pmatrix}\cos\left(2\pi\cdot\frac{100\cdot k}{360}\right) & \sin\left(2\pi\cdot\frac{100\cdot k}{360}\right) & 0\\ -\sin\left(2\pi\cdot\frac{100\cdot k}{360}\right) & \cos\left(2\pi\cdot\frac{100\cdot k}{360}\right) & 0\\ 0 & 0 & 1\end{pmatrix}^{T}\cdot\begin{pmatrix}0.624 & 0 & 0.4\\ 0 & 0.05 & 0\\ 0.4 & 0 & 0.577\end{pmatrix}\cdot\begin{pmatrix}\cos\left(2\pi\cdot\frac{100\cdot k}{360}\right) & \sin\left(2\pi\cdot\frac{100\cdot k}{360}\right) & 0\\ -\sin\left(2\pi\cdot\frac{100\cdot k}{360}\right) & \cos\left(2\pi\cdot\frac{100\cdot k}{360}\right) & 0\\ 0 & 0 & 1\end{pmatrix}\cdot\begin{pmatrix}e^{-i\cdot\frac{100k\,\pi}{180}} & 0 & 0\\ 0 & e^{-i\cdot\frac{100k\cdot\pi}{180}} & 0\\ 0 & 0 & e^{-i\cdot\frac{100k\cdot\pi}{180}}\end{pmatrix}\right]=\begin{pmatrix}0.089+0.124i & -0.156+0.16i & 4.365-0.06i\\ -0.156+0.16i & -0.165-0.557i & 0.06-4.035i\\ 4.365-0.06i & 0.06-4.035i & -0.065-0.371i\end{pmatrix} \tag{22}$$

The Raman tensor for the second segment is:

A mode:

$$\sum_{k=21}^{27}\left[\begin{pmatrix}\cos\left(2\pi\cdot\frac{60}{360}\right) & 0 & -\sin\left(2\pi\cdot\frac{60}{360}\right)\\ 0 & 1 & 0\\ \sin\left(2\pi\cdot\frac{60}{360}\right) & 0 & \cos\left(2\pi\cdot\frac{60}{360}\right)\end{pmatrix}\begin{pmatrix}\cos\left(2\pi\cdot\frac{100\cdot k}{360}\right) & \sin\left(2\pi\cdot\frac{100\cdot k}{360}\right) & 0\\ -\sin\left(2\pi\cdot\frac{100\cdot k}{360}\right) & \cos\left(2\pi\cdot\frac{100\cdot k}{360}\right) & 0\\ 0 & 0 & 1\end{pmatrix}^{T}\cdot\begin{pmatrix}0.624 & 0 & 0.4\\ 0 & 0.05 & 0\\ 0.4 & 0 & 0.577\end{pmatrix}\cdot\right.$$

$$\left.\begin{pmatrix}\cos\left(2\pi\cdot\frac{100\cdot k}{360}\right) & \sin\left(2\pi\cdot\frac{100\cdot k}{360}\right) & 0\\ -\sin\left(2\pi\cdot\frac{100\cdot k}{360}\right) & \cos\left(2\pi\cdot\frac{100\cdot k}{360}\right) & 0\\ 0 & 0 & 1\end{pmatrix}\begin{pmatrix}\cos\left(2\pi\cdot\frac{60}{360}\right) & 0 & -\sin\left(2\pi\cdot\frac{60}{360}\right)\\ 0 & 1 & 0\\ \sin\left(2\pi\cdot\frac{60}{360}\right) & 0 & \cos\left(2\pi\cdot\frac{60}{360}\right)\end{pmatrix}^{T}\right]=\begin{pmatrix}3.592 & -0.111 & -0.729\\ -0.111 & 2.309 & -0.035\\ -0.729 & -0.035 & 2.856\end{pmatrix} \quad (23)$$

E1 mode:

$$\sum_{k=21}^{27}\left[\begin{pmatrix}\cos\left(2\pi\cdot\frac{60}{360}\right) & 0 & -\sin\left(2\pi\cdot\frac{60}{360}\right)\\ 0 & 1 & 0\\ \sin\left(2\pi\cdot\frac{60}{360}\right) & 0 & \cos\left(2\pi\cdot\frac{60}{360}\right)\end{pmatrix}\begin{pmatrix}\cos\left(2\pi\cdot\frac{100\cdot k}{360}\right) & \sin\left(2\pi\cdot\frac{100\cdot k}{360}\right) & 0\\ -\sin\left(2\pi\cdot\frac{100\cdot k}{360}\right) & \cos\left(2\pi\cdot\frac{100\cdot k}{360}\right) & 0\\ 0 & 0 & 1\end{pmatrix}^{T}\cdot\right.$$

$$\left.\begin{pmatrix}0.624 & 0 & 0.4\\ 0 & 0.05 & 0\\ 0.4 & 0 & 0.577\end{pmatrix}\cdot\begin{pmatrix}\cos\left(2\pi\cdot\frac{100\cdot k}{360}\right) & \sin\left(2\pi\cdot\frac{100\cdot k}{360}\right) & 0\\ -\sin\left(2\pi\cdot\frac{100\cdot k}{360}\right) & \cos\left(2\pi\cdot\frac{100\cdot k}{360}\right) & 0\\ 0 & 0 & 1\end{pmatrix}\cdot\begin{pmatrix}\cos\left(2\pi\cdot\frac{60}{360}\right) & 0 & -\sin\left(2\pi\cdot\frac{60}{360}\right)\\ 0 & 1 & 0\\ \sin\left(2\pi\cdot\frac{60}{360}\right) & 0 & \cos\left(2\pi\cdot\frac{60}{360}\right)\end{pmatrix}^{T}\right]$$

$$\left[\begin{pmatrix} e^{i\cdot\frac{100(k-21)\pi}{180}} & 0 & 0 \\ 0 & e^{i\cdot\frac{100(k-21)\cdot\pi}{180}} & 0 \\ 0 & 0 & e^{i\cdot\frac{100(k-21)\cdot\pi}{180}} \end{pmatrix}\right] = \begin{pmatrix} -0.735 - 0.98i & 0.988 - 0.494i & -0.39 - 0.68i \\ 0.988 - 0.494i & 1.025\times10^{-3} + 0.19i & -0.714 + 0.406i \\ -0.39 - 0.68i & -0.714 + 0.406i & 0.592 + 1.035i \end{pmatrix}$$

(24)

$$\sum_{k=21}^{27}\left[\begin{pmatrix} \cos\left(2\pi\cdot\frac{60}{360}\right) & 0 & -\sin\left(2\pi\cdot\frac{60}{360}\right) \\ 0 & 1 & 0 \\ \sin\left(2\pi\cdot\frac{60}{360}\right) & 0 & \cos\left(2\pi\cdot\frac{60}{360}\right) \end{pmatrix}\begin{pmatrix} \cos\left(2\pi\cdot\frac{100\cdot k}{360}\right) & \sin\left(2\pi\cdot\frac{100\cdot k}{360}\right) & 0 \\ -\sin\left(2\pi\cdot\frac{100\cdot k}{360}\right) & \cos\left(2\pi\cdot\frac{100\cdot k}{360}\right) & 0 \\ 0 & 0 & 1 \end{pmatrix}^{T}\right]$$

$$\begin{pmatrix} 0.624 & 0 & 0.4 \\ 0 & 0.05 & 0 \\ 0.4 & 0 & 0.577 \end{pmatrix}\begin{pmatrix} \cos\left(2\pi\cdot\frac{100\cdot k}{360}\right) & \sin\left(2\pi\cdot\frac{100\cdot k}{360}\right) & 0 \\ -\sin\left(2\pi\cdot\frac{100\cdot k}{360}\right) & \cos\left(2\pi\cdot\frac{100\cdot k}{360}\right) & 0 \\ 0 & 0 & 1 \end{pmatrix}\begin{pmatrix} \cos\left(2\pi\cdot\frac{60}{360}\right) & 0 & -\sin\left(2\pi\cdot\frac{60}{360}\right) \\ 0 & 1 & 0 \\ \sin\left(2\pi\cdot\frac{60}{360}\right) & 0 & \cos\left(2\pi\cdot\frac{60}{360}\right) \end{pmatrix}^{T}$$

$$\left[\begin{pmatrix} e^{-i\cdot\frac{100(k-21)\pi}{180}} & 0 & 0 \\ 0 & e^{-i\cdot\frac{100(k-21)\cdot\pi}{180}} & 0 \\ 0 & 0 & e^{-i\cdot\frac{100(k-21)\cdot\pi}{180}} \end{pmatrix}\right] = \begin{pmatrix} -0.735 + 0.98i & 0.988 + 0.494i & -0.39 + 0.68i \\ 0.988 + 0.494i & 1.025\times10^{-3} - 0.19i & -0.714 - 0.406i \\ -0.39 + 0.68i & -0.714 - 0.406i & 0.592 - 1.035i \end{pmatrix}$$

(25)

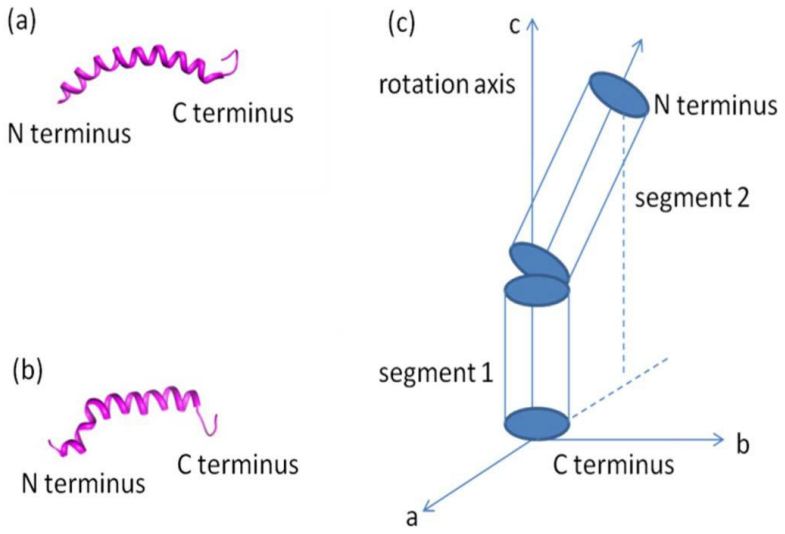

Figure 3.1 Structures of LL-37 (a) associated with SDS vesicles (PDB: 2K6O) (b) associated with SDS vesicles (PDB: reported by Ramamoorthy group) (c) A cartoon representation of the LL-37 molecular structure and the rotation axis.

3.2.3 Details in Orientation Calculation

First of all, we summarize the assumptions in deducing the orientation information.

1. SFG is surface sensitive only when the inversion symmetry is broken, therefore we assume that the SFG signal only comes from the peptides absorbed on the lipid bilayer rather than those in the bulk.
2. We assume a single δ-distribution for the tilt angles of the peptides.
3. In both models, we average the twist angle of the second segment as shown in Figure 6 when obtaining the SFG hyperpolarizability tensor for the peptide molecule.
4. When the LL-37 peptide is absorbed on POPC lipid bilayer, we assume it adopts the NMR structure in DPC vesicles. When the LL-37 peptide is absorbed on POPG lipid bilayer, we assume it adopts the NMR structure in SDS vesicles.

The SFG hyperpolarizability tensor is a third-rank tensor, a Kronecker product of the Raman polarizability tensor and the IR transition dipole moment. This microscopic hyperpolarizability tensor is associated with the macroscopic second-order nonlinear optical susceptibility by the Euler angle projection:

$$\chi_{ijk,q} = N_S \sum_{l,m,n} \langle (\hat{\imath} \cdot \hat{l})(\hat{\jmath} \cdot \hat{m})(\hat{k} \cdot \hat{n}) \rangle \beta_{lmn,q} \tag{26}$$

Experimentally, the SFG signals from the A (peak center: ~1650 cm^{-1}) and E1 modes (peak center: ~1652 cm^{-1}) cannot be resolved due to the spectral resolution of our SFG system. Thus the SFG signal is considered as arising from the contributions of both the A and E1 modes.

$$\chi = \chi_A + \chi_{E1} \tag{27}$$

Assuming the orientation angle distribution of the first segment to be a δ-distribution, if we average the twist angle of the second segment as shown in Figure 3.1, we can calculate different elements of the second order nonlinear optical susceptibility as a function of the orientation angle (of the first segment) .

3.2.4 Surface Plasmon Resonance (SPR) Measurements

In this research, we applied SPR to compare the adsorption amounts of LL-37 onto single substrate supported POPG and POPC bilayers using a home-built SPR equipment. The substrate surface for the lipid bilayers is SiO_2 deposited on gold. The lipid bilayers were prepared by vesicle fusion. The detailed SPR experiments and results are presented below.

3.2.4.1 Instrument Configuration

The configuration of a homemade SPR biosensing system is shown in Figure 3.2. Briefly, a 670 nm laser beam was incident upon the sample, driven by a galvo scanner which can be

scanned for about 10˚. The reflected beam was collected by a cylindrical lens pair. By detecting the resonance angle shift of the reflection beam, the binding process occurring on the sensing surface could thus be monitored. A two-channel flow chamber was used and all solutions were handled by two syringe pumps. In an actual experiment, one of the two channels was used as the reference to compensate the temperature drift.

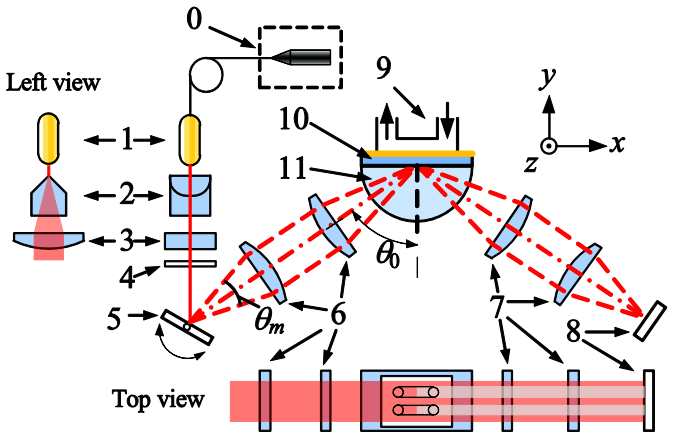

Figure 3.2 Optical schematic of our galvo scanner based SPR sensing setup: (0) 2 mW 670 nm laser diode (1) fiber collimator, (2) powell lens, (3) cylindrical lens, (4) polarizer, (5) galvo scanner, (6), (7) cylindrical lens pairs, (8) 1-D photodiode array, (9) 2-channel flow chamber, (10) sensing chip and (11) prism.

3.2.4.2 Sensing Chip Fabrication

A 50 nm-thick gold film was deposited on a BK7 glass slide with 1 nm Ti as the adhesion layer by sputtering. Then a 10 nm-thick SiO_2 film was deposited on top of the gold film with 1 nm Ti as the adhesion layer. Before every experiment, the chip was cleaned by piranha solution (98% H_2SO_4 and 30% H_2O_2, 7:3, v/v) and plasma cleaner.

3.2.4.3 Lipid Vesicle Preparation

3 mg phospholipid(s) dissolved in chloroform were dried under a stream of nitrogen gas in a glass test tube and then stored in a vacuum chamber for 1 h to evaporate all the residual solvent. The dried lipids were re-suspended in 1 mL PBS by vigorous vortexing. Large unilamellar vesicles (LUVs) were prepared by extruding the lipids suspension through a 100 nm pore size polycarbonate filter for 19 times.

3.2.4.4 Supported Lipid Bilayer Formation

150 μL vesicle suspension was injected to pass over the SiO_2 surface at a flow rate of 5 L/min at the room temperature. The immobilized lipid vesicles would fuse into lipid bilayers on the hydrophilic surface. In order to wash away unattached vesicles and multi lipid bilayers, 200 μL 100 mM NaOH aqueous solution was injected at 100 μL/min. After washing the NaOH solution, a stable baseline of the SPR signal can be acquired, indicating that a stable lipid bilayer was formed on the sensing surface. The peptide solution was injected at a flow rate of 50 μl/min. During the whole process, Millipore water was used as the running buffer.

3.3. Results

3.3.1 SFG Results of LL-37 Associated with a POPC/POPC and POPG/POPG Lipid Bilayer at Different Concentrations

Structures of LL-37 in SDS[12] and DPC[11] micelles were reported based on solution NMR studies (Figure 3.1). The continuous helical region includes the residues 2-31 in SDS with a bend between residues 14-16. The bend is caused by the hydrophobic interaction between residues Ile13 and Phe17 and the membrane. The angle between the two helical segments connected by the bend is about 143 ° (Figure 3.1a). We developed the “bend model” to determine the peptide orientation in POPG lipid bilayers for our SFG study (Figure 3.3). The structure of LL-37

associated with zwitterionic DPC micelles was also reported based on a solution NMR study.[4] The well-structured region is from residues 4 to 33 and the helix-break-helix motif was highlighted with a break at residue Lys-12 (Figure 3.2b). Both structural studies suggest a tight cluster formed by residue Ile13 and Phe17. In contrast to the LL-37 structure in SDS vesicles, where the N-terminal region is rigid, the N terminus of LL-37 was found to be dynamic in DPC micelles. Since there is a disruption in LL-37 helicity when associated with zwitterionic lipid vesicles, we adopt the "disruption model" to address the disruption in the LL-37 helical structure for SFG data analysis. Since the N terminus is dynamic, we calculated the orientation dependence of the nonlinear optical susceptibility components for structures with different residue numbers in the N terminal α-helical region to ensure that our model is reliable (Figure 3.3). A schematic of the LL-37 molecule and the molecular axes used for SFG data analysis is shown in Figure 3.1c. The details of the bend and disrupted mode have been described in Section 3.2.

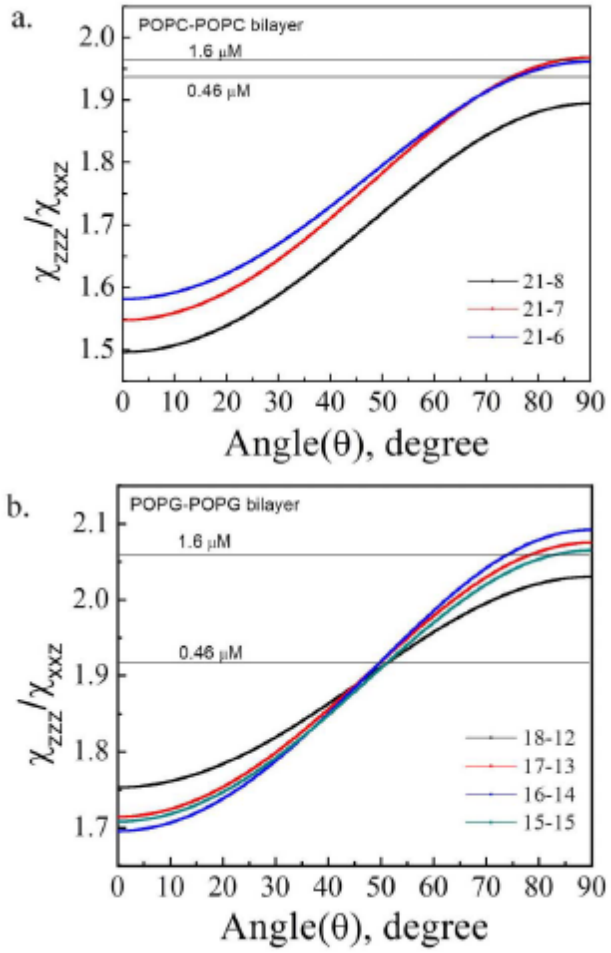

Figure 3.3 (a) Dependence of the calculated SFG $\chi^{(2)}_{zzz}/\chi^{(2)}_{xxz}$ ratio of LL-37 associated with a POPC/POPC bilayer on the helix tilt angle (first segment) relative to the bilayer surface normal. The first segment has 21 amino acid residues, and the second segment has 6, 7, and 8 amino acid residues respectively (the disruption model). (b) Dependence of the calculated SFG $\chi^{(2)}_{zzz}/\chi^{(2)}_{xxz}$ ratio of LL-37 associated with a POPG/POPG bilayer on the helix tilt angle (first segment) relative to the surface normal. 18-12, 17-14, 16-14, and 15-15 refer to the peptides with the first α-helical segment of 18, 17, 16, and 15 amino acid residues and the second α-helical segment of 12, 13, 14, and 15 amino acid residues respectively (the bend model).

Since LL-37 has a random coil structure for the N-terminal residues, we need to ensure that the detected SFG amide I signal is dominated by the contributions from the α-helical component. Contribution to the entire SFG signal from the unstructured region of the peptide

was calculated by NLOPredict developed by the Simpson group[35] for both the bent and disrupted structures of LL-37. We found that for both the membrane-surface and transmembrane orientations, the SFG signal contribution from random coil structured regions is less than 5% of the total SFG signal (even under the assumption that the peak of the random coil overlaps with that of the α-helical components). Therefore, it is reasonable to assume that the signal attributed to the a-helical structured region of the peptide is the main contributor to the measured SFG signal in the amide I region.

SFG spectra collected with ssp and ppp polarization combinations from LL-37 associated with POPC/POPC bilayers in the amide I frequency region at 0.46 μM and 1.6 μM concentrations are shown in Figure 3.4a. Here, for the SFG signals in the amide I frequency range, we collected spectra using two polarization combinations, ssp and ppp, in order to deduce the LL-37 orientation from the spectral fitting result $\chi_{eff,ppp}/\chi_{eff,ssp}$. The SFG spectra in Figure 3.4a exhibit a single peak centered around ~1647 cm^{-1}, indicating an α-helical structure. The SFG spectral intensities for the two studied concentrations are very similar, and the fitting results of $\chi_{eff,ppp}$ and $\chi_{eff,ssp}$ are displayed in Table 3.1a. Using the spectral fitting results and the "disruption model" (Figure 3.3a), the orientation analysis shows that the LL-37 peptide lies more or less parallel to the membrane surface with a tilt angle between 56° and 90° relative to the lipid bilayer normal at the peptide concentration of 0.46 μM and 68° to 90° at the peptide concentration of 1.6 μM. The similar orientation and SFG spectral intensities indicate that the adsorption amounts of LL-37 at 0.46 μM and 1.6 μM are similar.

(a)

POPC/POPC	Polarization	peakcenter (cm^{-1})	Peak Width (cm^{-1})	χ_{eff}	Ratio	Tilt angle	Adsorption amount

0.46Mm	ssp	1649	7.9	14.8	1.94±0.13	56-90	1.1
	ppp	1647	9.7	23.7			
1.6μM	ssp	1649	13.5	14.3	1.96±0.06	68-90	1.1
	ppp	1647	11.3	24.2			

(b)

POPG/POPG	Polarization	Peak center (cm^{-1})	Peak Width (cm^{-1})	χ_{eff}	Ratio	tilt angle	Adsorption amount
0.46μM	ssp	1648	13	33.6	1.92±0.04	44-58	1.0
	ppp	1650	12	56.5			
1.6 μM	ssp	1649	11	45.3	2.06±0.07	62-90	2.8
	ppp	1649	12	78.3			

(c)

POPC:POPG=7:3	Polarization	Peak center (cm^{-1})	Peak Width (cm^{-1})	χ_{eff}	Ratio	tilt angle
0.46μM	ssp	1645	13.8	17.11	2.02±0.01	63-80
	ppp	1648	13.7	30.6		
1.6 μM	ssp	1646	11.2	26.9	1.68±0.07	0-25
	ppp	1649	13.9	42.1		

(d)

POPC:POPG=3:7	Polarization	Peak center (cm^{-1})	Peak Width (cm^{-1})	χ_{eff}	Ratio	tilt angle
0.46μM	ssp	1648	14.0	20.3	1.72±0.01	0-15
	ppp	1646	11.5	30.8		
1.6 μM	ssp	1651	13.8	28.0	2.07±0.05	65-90
	ppp	1651	10.6	51.6		

Table 3.1 Fitting parameters of the SFG amide I spectra of LL-37 associated with (a) POPC/POPC, (b) POPG/POPG, (c) POPC:POPG=7:3, and (d) POPC:POPG=3:7 bilayers.

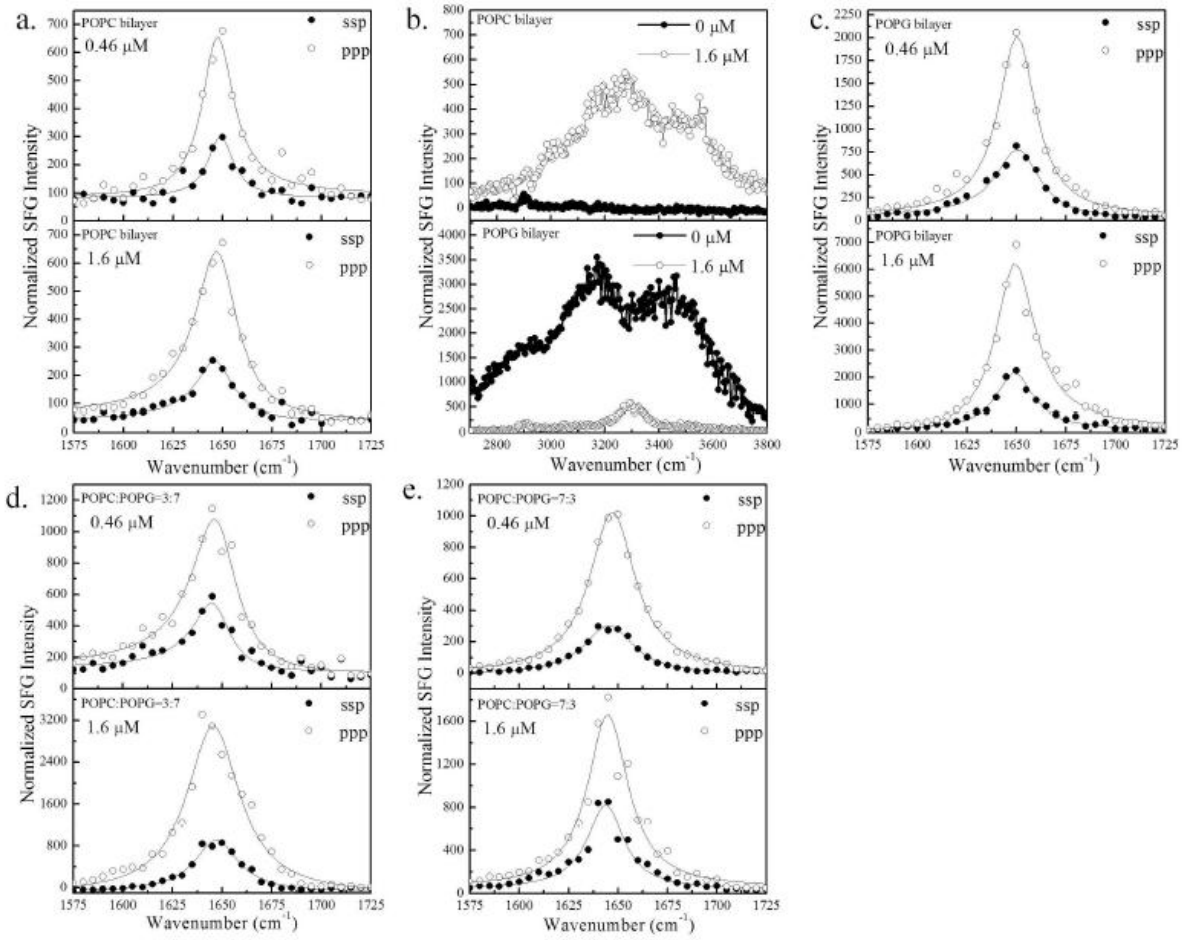

Figure 3.4 (a) SFG amide I spectra of LL-37 associated with POPC/POPC bilayer; (b) SFG O-H/N-H stretching signals collected from the POPC (top) and POPG (bottom) bilayers in contact with LL-37 solution (1.6 μM); SFG amide I spectra of LL-37 associated with (c) POPG/POPG bilayer, (d) 3:7 POPC:POPG and (e) 7:3 POPC:POPG lipid bilayers.

SFG signals detected in the frequency range of 3000-3600 cm^{-1} before and after the addition of LL-37 to the POPC/POPC bilayer are shown in Figure 3.4b. Since the POPC headgroup is neutral, the POPC/POPC bilayer associated water molecules do not have a preferred orientation, therefore no water O-H stretching SFG signal was detected prior to the

addition of the LL-37 stock solution into the subphase. After the addition of LL-37, a broad SFG signal in this frequency range was detected, which is mostly attributed to the water O-H stretching mode and the N-H stretching peak (centered at 3280 cm^{-1}) of LL-37. Because LL-37 is positively charged, the ordered LL-37 molecules associated with the POPC/POPC bilayers can induce ordering of surrounding water molecules that generate the SFG O-H stretching signal. Since the POPC/POPC bilayer is neutral, the observed SFG signal in this range suggests that LL-37 potentially interacts with the POPC/POPC bilayer by hydrophobic interaction instead of electrostatic interaction.

The membrane surface orientation of LL-37 associated with the POPC bilayer deduced by the SFG amide I signal in this study is in excellent agreement with solid-state NMR results.[8,14]

The amide I signals observed for LL-37 associated with POPG/POPG lipid bilayers (Figure 3.4c) feature a single peak at ~1649 cm^{-1}, similar to the POPC/POPC case. The SFG intensities for the high and low peptide concentrations are similar in both polarization combinations in a POPC/POPC system. However, there is a significant increase in the SFG intensity when the concentration is increased in the POPG/POPG system. The spectra were fitted with parameters displayed in Table 3.1b and the ratios of $\chi_{eff,ppp}$ and $\chi_{eff,ssp}$ were used to deduce the orientation angles. Since previous NMR studies indicated that LL-37 has a bend in the middle when associated with negatively charged vesicles, we adopt the "bend model" discussed above to examine LL-37's orientation associated with POPG/POPG lipid bilayers (Figure 3.3b). This model considers the phase continuity between the vibrational modes of the two segments in the data analysis; details can be found in the section 3.2. Our analysis shows that LL-37 orients with a tilt angle of 44 ° to 58 ° relative to the POPG/POPG surface normal for the 0.46 μM

peptide concentration case and 62° to 90° for the 1.6 μM concentration case. These results reveal that the membrane orientation of LL-37 in POPG/POPG bilayer is dependent on the peptide concentration and, at low concentrations, the peptides tilt to form a transmembrane orientation. This change in the peptide orientation could be attributed to the oligomerization of the peptide as observed from solid-state NMR experiments.[13]

SFG signals collected in the frequency range of 3000-3600 cm^{-1} before and after the addition of LL-37 (with the final concentration of 1.6 μM) to the POPG/POPG bilayer subphase are shown in Figure 3.8b. Before the addition of the LL-37, the spectra showed two broad peaks at ~3200 cm^{-1} and ~3500 cm^{-1} which can be explained as follows: the negatively charged lipid headgroups of the POPG/POPG bilayer facilitate the ordering of the associated water molecules, resulting in prominent water O-H stretching SFG signals. However, after LL-37 was added to the subphase, the two broad peaks diminished and a new peak centered at 3300 cm^{-1} appeared (Figure 3.4b). With LL-37 added, we expect the cationic peptide molecules associated with the negatively-charged POPG/POPG bilayer partially neutralized the bilayer charge. The originally ordered water molecules induced by the charged lipids would be less ordered, leading to a substantial decrease or even disappearance of the SFG water signal as shown in Figure 3.8b. The new 3300 cm^{-1} is likely from the N-H stretching mode of the peptide molecules due to the existence of ordered LL-37 molecules on the membrane surface.

3.3.2 SFG Results of LL-37 Associated with a Mixed Lipid Bilayer at Different Concentrations

In order to better simulate the real cell membrane which contains mixed lipids, we also investigated LL-37 interacting with mixed lipid bilayers with different negatively charged and zwitterionic lipid ratios. For a POPC: POPG= 3:7 bilayer, the interaction result with LL-37 has a similar trend as that with the pure POPG system (Figure 3.8d). After increasing the LL-37

peptide concentration from 0.46 μM to 1.6 μM, the peptide orientation changed from perpendicular to the membrane surface (0~15 ° vs. the surface normal) to parallel to the surface (70~90 ° vs. the surface normal) if we assume the peptide adopts the same structure as in negative charged SDS vesicles. This shows that when LL-37 interacts with the mixed bilayer, LL-37 molecules target the POPG component. The peptides inserted into the bilayer at low concentrations and previous research has shown that LL-37 has a tendency to oligomerize[8]. It is likely the inserted peptides can be pulled out from the bilayer by other peptide molecules at a higher peptide concentration via hydrophobic-hydrophobic interaction.

For a POPC: POPG= 7:3 lipid bilayer, the orientation information deduced is somewhat complicated (Figure 3.4e). When the peptide concentration is 0.46 μM, the peptide molecules show a parallel orientation to the surface (65~75 ° relative to the bilayer normal) if we assume that the peptide adopts the same structure as in the neutral charged DPC vesicles. Interestingly, at 1.6 μM peptide concentration, the peptide molecules have a transmembrane orientation (0~15 ° relative to the bilayer normal). After increasing the peptide concentration to 4.8 μM, 6.4 μM and 7.9 μM, the peptide molecules resumed the parallel orientation, nearly lying down on the bilayer surface.

3.3.3 SFG Results of LL-37 Associated with a Cholesterol-containing Lipid Bilayer at Different Concentrations

We further investigated interactions between LL-37 and two lipid bilayers containing cholesterol (CHO). 1:1 POPC:CHO lipid bilayer was used and we monitored the SFG signal in the amide I and O-H stretching frequency regions in the same way as in the above studies without cholesterol. The experimental results showed that after adding LL-37 peptides to the subphase, the SFG water signal increases (Figure 3.5a), but it is not as substantial as that observed from the pure POPC lipid bilayer system (Figure 3.4b). The SFG water signal is

induced by the positive charge of the adsorbed LL-37 molecules and therefore it is reasonable to believe it is related to the amount of adsorbed LL-37 molecules regardless of the ordering of these LL-37 molecules. With the presence of cholesterol in the lipid bilayer, fewer LL-37 molecules interact with the lipid bilayer. In addition to the much weaker water signal, there is a striking difference in the spectral feature since there is no 3300 cm^{-1} peak in the cholesterol-containing system. No amide I signal was detected in ssp or ppp spectrum (Figure 3.5b). Although we believe that the POPC/CHO system has fewer LL37 molecules adsorbed, we could not assess the ordering of the adsorbed LL-37 molecules due to the low SFG amide I signal we detected.

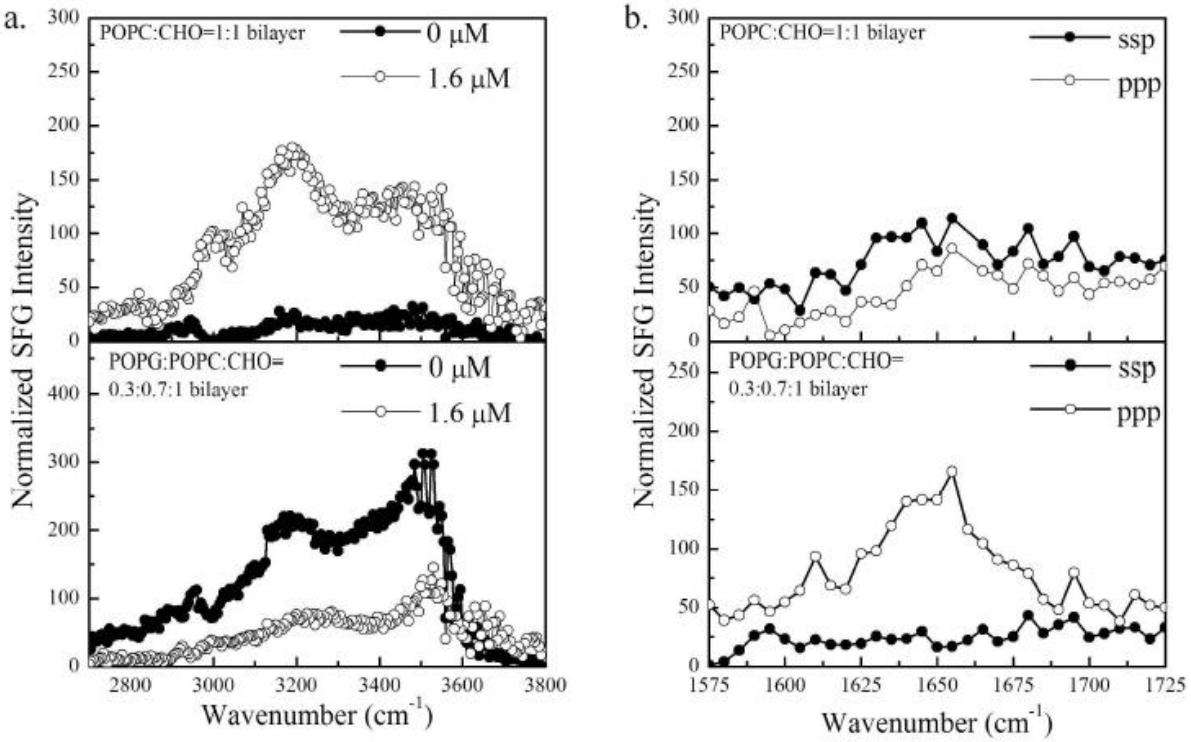

Figure 3.5 (a) SFG O-H/N-H stretching signals collected from the 1:1 POPC:CHO (top) and 0.3: 0.7:1 POPG:POPC:CHO (bottom) bilayers in contact with LL-37 solution (1.6 μM); (b) SFG amide I spectra of LL-37 associated with 1:1 POPC:CHO (top) and 0.3: 0.7:1 POPG:POPC:CHO (bottom) bilayers in contact with LL-37 solution (1.6 μM).

We also investigated the incorporation of cholesterol into a lipid bilayer containing an anionic lipid: POPG: POPC: CHO=0.3:0.7:1. After the injection of the LL-37 peptide solution into the subphase, neither discernible SFG N-H stretching signal (Figure 3.5a) nor SFG amide I ssp signal (Figure 3.5b) was detected. However, a small ppp SFG signal for the amide I band was observed. Compared to the 1:1 POPC:CHO lipid bilayer, this shows that the addition of negatively charged POPG to the lipid bilayer increases the surface coverage of associated LL-37 peptides. Still, the LL-37 surface coverage is significantly lower than that of LL-37 associated with the 3:7 POPG:POPC bilayer without CHO, suggesting that cholesterol suppresses the interaction of LL-37 with lipid bilayers. These results are in excellent agreement with solid-state NMR studies. [14,36]

3.4 Discussion

We compared the relative adsorption amounts of LL-37 molecules on POPC and POPG bilayers according to the observed SFG signal intensities, as summarized in Table 3.1a. The number of adsorbed molecules is proportional to χ_{xxz}/β_{aac}, where χ_{xxz} is deduced from the experimental SFG ssp spectrum (related to signal intensity) and β_{aac} is the microscopic hyperpolarizability component of the amide I signal of LL-37. The amount of LL-37 adsorption on the POPG bilayer is comparable to that on the POPC bilayer at 0.46 μM but it is ~2.6 times larger compared to that on the POPC bilayer at 1.6 μM. The adsorption amount of LL-37 interacting with POPG/POPG increased as the peptide concentration was raised, which can be attributed to the electrostatic interaction between the anionic lipid and the cationic peptide. The different adsorption amounts of LL-37 on POPG and POPC lipid bilayers were confirmed by surface plasmon resonance (SPR) experiments (Figure 3.6). It was shown by SPR that at the concentration of 1.6 μM, the initial adsorption amount of LL-37 on POPG is ~3 times larger than

that on POPC. Also, the peptides experience a certain degree of desorption on POPC but the adsorption amount remains stable on POPG. This indicates a weaker interaction between LL-37 and POPC compared to POPG. Since POPC is neutral, LL-37 only interacts with POPC via hydrophobic interactions. However, POPG is negatively charged and electrostatic interactions between the positively charged peptides and the membrane induce more peptide adsorption when the peptide concentration increases.

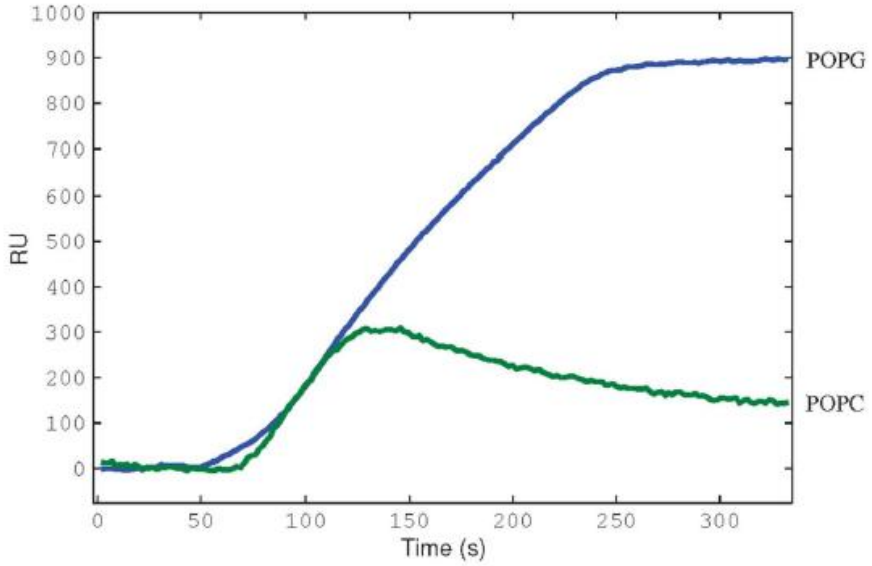

Figure 3.6 Time-dependent SPR signals observed before and after LL-37 peptide solutions with 1.6 M concentration in water were injected at 50 µL/min into the flow chambers to interact with the POPG (blue) and POPC (green) bilayers. For the POPG bilayer, the adsorption curve will reach a plateau at around 220 s. While for the POPC bilayer, peptides start to desorb from the lipid bilayer after 150 s, indicating a weaker interaction between LL-37 and the POPC bilayer compared to that with the POPG lipid bilayer.

The differences in the membrane orientation of LL-37 on POPC and POPG lipid bilayers facilitate the understanding of its membrane interaction mode. It was reported that lipid headgroup perturbation induced by LL-37 is larger in bilayers containing a negatively charged lipid (DMPG:DMPC=4:1) than in the zwitterionic DMPC bilayer, but the LL-37 molecules

adopt the same parallel orientation when associated with the lipid bilayers deduced using NMR spectroscopy.[38] It was proposed that LL-37 exhibits a non-pore formation carpet mode on zwitterionic DPC vesicles.[11] Our results for LL-37 associated with the POPC/POPC and POPG/POPG lipid bilayers with a high peptide concentration of 1.6 μM supports the above conclusions: for both cases, the peptides adopt an approximately parallel orientation. As we discussed above, the unique advantage of SFG study is that SFG can be used to study the interactions between LL-37 and model cell membranes at much lower (physiologically relevant) peptide concentrations. At a lower peptide concentration of 0.46 μM, SFG results indicate that the LL-37 molecules associated with the POPG/POPG bilayer tilted towards the membrane normal. Previous LL-37 research revealed that at ~0.5 and 1.5 μM, LL-37 molecules have both monomer and dimer forms in aqueous solution.[38] Trimers were detected when peptide concentration is increased to 50 μM. At our experimental condition, i.e. 0.46 μM and 1.6 μM, which is similar to 0.5 and 1.5 μM, it is most likely that LL-37 dissolve in water as monomers or/and dimers. We believe that for the POPC/POPC bilayer, the peptide molecules saturated at a low concentration of 0.46 μM as monomers/dimers and remain so at a higher peptide concentration of 1.6 μM. However, for the POPG/POPG bilayer, the peptides penetrate into the membrane at a low concentration. While at a higher peptide concentration, the domination of the peptide-peptide interaction could drag the initially inserted peptide molecules out of the membrane, which not only changes the overall membrane orientation of the peptides, but also induces the increase of the peptide adsorption amount.

For the systems with mixed lipids, we believe that the concentration-dependent behavior can be explained as follows: Initially, at a low peptide concentration, most of the LL-37 molecules interact with the POPC lipid, which is the major component of the POPC:POPG=7:3

bilayer. Therefore, the overall orientation of LL-37 is similar to that for the associated LL-37 with a pure POPC bilayer. At a slightly higher peptide concentration, more peptides can interact with the POPG lipids, which is the minor component in the bilayer. In this case, the interaction between LL-37 with the POPC:POPG=7:3 bilayer is similar to the situation when a pure POPG bilayer interacts with a lower concentration of LL-37 in which LL-37 can insert into the bilayer. At higher peptide concentrations, additional peptides that associated with the bilayer pulled the inserted LL-37 out of the membrane, as in the pure POPG bilayer case which leads to a parallel orientation.

3.5. Conclusion

In summary, we have examined the molecular interaction of the LL-37 peptide with a variety of lipid bilayers using SFG (Figure 3.7), and have developed a SFG orientation analysis methodology for bent and disrupted α-helices. We have demonstrated that SFG is sensitive enough to study peptide-lipid molecular interaction at low-peptide concentrations, which is beyond other techniques such as NMR. LL-37 is shown to saturate the pure POPC lipid bilayer at a low concentration (0.46 μM) with an orientation parallel to the membrane surface. However, in pure POPG or POPC/POPG mixed lipid bilayers, LL-37 exhibits a reorientation upon changing the peptide concentration, suggesting the peptide aggregation process. In cholesterol-containing systems, SFG results demonstrate that cholesterol has a significant suppression effect on the peptide-membrane interaction. We strongly believe that the experimental and data analysis approaches developed in this study would be highly applicable in studying other membrane active systems including other AMPs, cell penetrating peptides, fusion peptides and amyloid proteins.

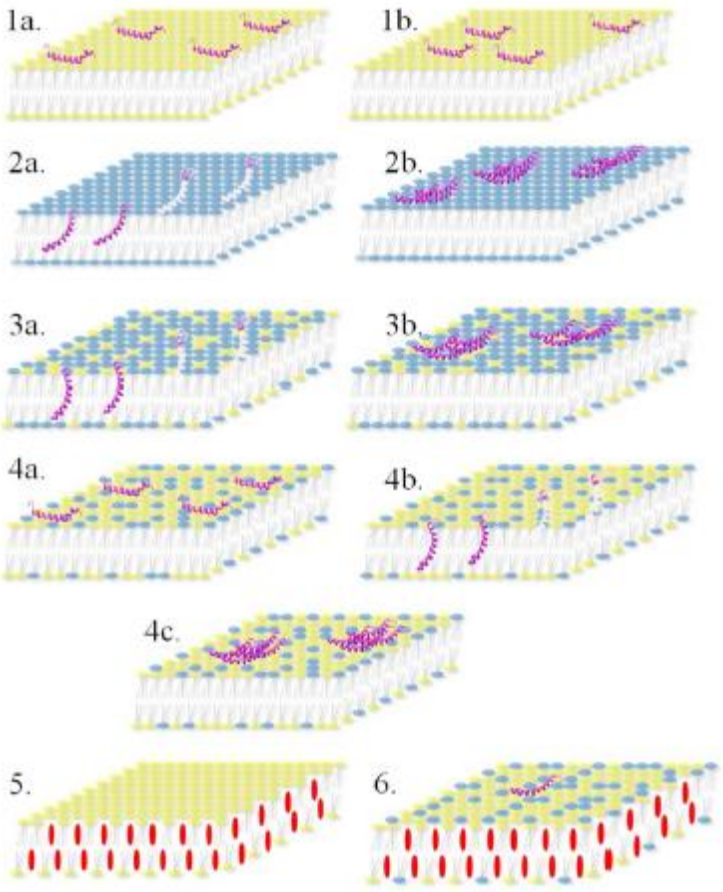

Figure 3.7 Schematics showing interactions between LL-37 and different lipid bilayers: (a) POPC bilayer at a low concentration (left) and a high concentration (right); (b) POPG bilayer at a low concentration (left) and a high concentration (right); (c) 3:7 POPC:POPG lipid bilayer at a low concentration (left) and a high concentration (right); (d) 7:3 POPC:POPG lipid bilayer at a low concentration (left) and a high concentration (right) and even higher concentrations (bottom); (e) 1:1 POPC:CHO lipid bilayer at a low concentration (left) and a high concentration (right); (f) 0.3: 0.7:1 POPG:POPC:CHO lipid bilayer at a low concentration (left) and a high concentration (right)

3.6 References

(1) Dürr, U. H. N., Sudheendra, U. S. & Ramamoorthy, A. *Biochim. Biophys. Acta.* **1758**, 1408-1425 (2006).

(2) Zasloff, M. *Nature.* **415**, 389 (2002).

(2) Ding, J. L.& Ho, B. *Drug Dev. Res.* **62**, 317 (2004).

(3) Matsuzaki, K. *Biochim. Biophys. Acta.* **1462**, 1(1999).

(4) Hancock, R. E.& Diamond, G. *Trends Microbiol.* 8, 402 (2000).

(5) Epand, R. M. & Vogel, H. J. *Biochim. Biophys. Acta.* **1462**, 11 (1999).

(6) Sitaram, N.; Nagaraj, R. *Biochim. Biophys. Acta*. **1462**, 29 (1999).

(7) Brogden, K. A. *Nat. Rev. Microbiol.* **3**, 238 (2005).

(8) Dürr, U. H. N., Sudheendra, U. S. & Ramamoorthy, A. *Biochim. Biophys. Acta.* **1758**, 1408-1425 (2006).

(9) Burton, M. F. & Steel, P. G. *Nat. Prot. Rep.* **26,** 1572-1584 (2009).

(10) Neville, F. *et al*. *Biophys. J.* **90,** 1275-1287 (2006).

(11) Porcelli, F., Verardi, R., Shi, L., Wildman, K. A. H., Ramamoorthy, A. & Veglia, G. *Biochemistry* **47,** 5565-5572 (2008).

(12) Wang, G. *J. Biol. Chem.* **283,** 32637-32643 (2008).

(13) Ramamoorthy, A., Lee, D.-K., Santos, J. S. & Wildman, K. A. H. *J. Am. Chem. Soc.* **130,** 11023-11029 (2008).

(14) Wildman, K. A. H., Lee, D-K. & Ramamoorthy, A. *Biochemistry* **42**, 6545-6558 (2003).

(15) Chen, Z., Shen, Y. R. & Somorjai, G. A. *Annu. Rev. Phys. Chem.* **53,** 437-465 (2002).

(16) Mermut, O., Phillips, D. C., York, R. L., McCrea, K. R., Ward, R. S. & Somorjai, G. A. *J. Am. Chem. Soc.* **128,** 3598-3607 (2006).

(17) Guyot-Sionnest, P., Hunt, J. & Shen, Y. *Phys. Rev. Lett.* **59,** 1597-1600 (1987).

(18) Baker, L. R. *et al*. *J. Am. Chem. Soc.* **134**, 14208-14216 (2012).

(19) Ye, H. K., Abu-Akeel. A., Huang, J., Katz. H.E. & Gracias, D. H. *J. Am. Chem. Soc.* **128,** 6528-6529 (2006).

(20) Yang, Z., Li, Q. F. & Chou, K. C. *J. Phys. Chem. C.* **113,** 8201-8205 (2009).

(21) Perry, A., Neipert, C. & Space, B. *Chem. Rev.* **106,** 1234-1258 (2006).

(22) Moore, F. G. & Richmond, G. L. *Accounts. Chem. Res.* **41,** 739-748, (2008).

(23) Weidner, T., Breen, N. F., Li, K., Drobny, G. P. & Castner, D. G. *P. Natl. Acad. Sci. USA.* **107,** 13288-13293 (2010).

(24) Jung, S.-Y. *et al*. *J. Am. Chem. Soc.* **125,** 12782-12786 (2003).

(25) Chen, X. *et al*. *Langmuir* **26,** 16447-16454 (2010).

(26) Liu, J. & Conboy, J. C. *J. Am. Chem. Soc.* **126,** 8376-8377 (2004).

(27) Ma, G., Chen, X. & Allen, H. C. *J. Am. Chem. Soc.* **129,** 14053-14057, (2007).

(28) vandenAkker, C. C., Engel, M. F. M., Velikov, K. P., Bonn, M. & Koenderink, G. H. *J. Am. Chem. Soc.* **133**, 18030-18033 (2012).

(29) Chen, X., Wang, J., Sniadecki, J. J., Even, M. A. & Chen, Z. *Langmuir* **21,** 2662-2664 (2005).

(30) Fu, L., Liu, J. & Yan, E. C. Y. *J. Am. Chem. Soc.* **133,** 8094-8097 (2011).

(31) Fu, L., Ma, G. & Yan, E. C. Y. *J. Am. Chem. Soc.* **132,** 5405-5412 (2010).

(32) Nguyen, K. T., Soong, R., Lm, S.-C., Waskell, L., Ramamoorthy, A. & Chen, Z. *J. Am. Chem. Soc.* **132**. 15112-15115 (2010).

(33) Nguyen, K. T., Clair, S. V. Le., Ye, S. & Chen, Z. *J. Phys. Chem. B.* **113,** 12358-12363 (2009).

(34) Chen, X., Wang, J., Boughton, A. P., Kristalyn, C. B. & Chen, Z. *J. Am. Chem. Soc.* **129,** 1420-1427 (2007).

(35) Moad, A. J. *et al. J. Comput. Chem.* **28.** 1996-2002 (2007).

(36) Ramamoorthy, A., Lee, D. K., Narasimhaswamy, T., & Nanga, R. P. *BBA-Biomembranes* **1798,** 223-227 (2010).

(37) Wildman, K. A. H., Martinez, G. V., Brown, M. F. & Ramamoorthy, A. *Biochemistry* **43,** 8459-8469 (2004).

(38) Oren, Z., Lerman, J. C., Gudmundsson, G. H., Agerberth, B. & Shai Y. *Biochem. J.* **341,** 501-513 (1999).

(39) Berg, M. J., Tymoczko, L. J. & Stryer, L. *Biochemistry*; (W. H. Freeman and Company, New York, 2007).

(40) Langelaan, D. N., Wieczorek, M., Blouin, C. & Rainey, J. K. *J. Chem. Inf. Model.* **50,** 2213-2220, (2010).

(41) Fanconi, B., Tomlinson, B., Nafie, L. A., Small, W. & Peticolas, W. L. *J. Chem. Phys.* **1969**, *51*, 3993-4005.

(42) Nguyen, K. T., Clair, S. V. Le., Ye, S. & Chen, Z. *J. Phys. Chem. B.* **113,** 12169-12180 (2009).

CHAPTER 4

UNVEILING THE MEMBRANE-BINDING PROPERTIES OF N-TERMINAL AND C-TERMINAL REGIONS OF G PROTEIN-COUPLED RECEPTOR KINASE 5 BY COMBINED OPTICAL SPECTROSCOPIES

In Chapters 2 and 3, both wild-type LL-37 and the entire length of Pep-1 were investigated. However, in peptides, different segments may play different roles according to the properties of the consisted amino acids which exist within the segments. In this chapter, in order to distinguish the different roles of the segments in the GRK5 N-terminal peptide, we truncated the peptide into two parts and investigated their membrane adsorption property and conformation under different conditions by using both SFG and ATR-FTIR spectroscopies. This work was completed in collaboration with Prof. John J. G. Tesmer, Alisa Glukhova, Prof. Henry I. Mosberg and Katarzyna Sobczyk-Kojiko. The peptide samples were provided by Mosberg lab and Prof. Tesmer and Alisa contributed tremendously in data interpretation. The work is published as: Ding, B.; Glukhova, A.; Sobczyk-Kojiro, K.; Mosberg, H. I.; Tesmer, J. J. G.; Chen, Z. *Langmuir* **2014**, *30*, 823–31.

4.1 Introduction

G protein-coupled receptors (GPCRs) are integral membrane proteins that transduce extracellular signals such as light, hormones and chemoattractants to downstream signal

pathways.[1] Activated GPCRs are phosphorylated by a family of serine/threonine kinases named G protein-coupled receptor kinases (GRKs), a process that initiates their desensitization. The ability to interact with membranes in which GPCRs are found is essential for GRK's function.[2] Various GRKs have different ways of associating with lipid bilayers.[3] GRK1 and GRK7 are post-translationally modified by prenyl groups at their C-termini. GRK2 and GRK3, on the other hand, bind to membranes by virtue of their C-terminal pleckstrin homology (PH) domains, which bind to acidic phospholipids and interact with heterotrimeric Gβγ subunits, which are prenylated. GRK4, GRK5, and GRK6 constitute a subfamily of GRKs that have 2-3 membrane-binding motifs. The first is a basic segment near the N-terminus that is believed to be responsible for binding phosphatidylinositol-4,5-bisphosphate (PIP_2). The second is an amphipathic helix located at the extreme C-terminus that is believed to interact with anionic lipid bilayers. GRK4 and GRK6 are in addition palmitoylated on cysteines immediately C-terminal to this helix. Proposed roles for these residues include either direct interaction with activated receptors[4] or with the phospholipid bilayer[5,6], either of which is proposed to induce helical character in this region and promote the formation of an activated form of the kinase domain.

Over the past several years, crystallographic studies have yielded new insights into the molecular mechanism for regulation of GRKs by their interactions with receptors and membranes.[4] However crystallographic analysis requires the removal of protein complexes from their native membrane environment and cannot provide direct information on how these molecules are arranged on the membrane surface *in situ*. Sum frequency generation (SFG) vibrational spectroscopy is a powerful tool to examine peptides and proteins at biointerfaces,[7-14] and in particular, associated with cell membranes.[15-21] For example, orientations of peptides with different secondary structures, such as linear α-helices, [22,23] bent α-helices,[24,25] β-sheets[26] and 3_{10}

helices[27] associated with solid substrate supported lipid bilayers were deduced using polarized SFG studies. SFG has also been applied to investigate the membrane orientations of Gβγ, the Gβγ-GRK2 complex, and Gαβγ heterotrimers *in situ*.[28,29] Recently, we showed that the use of both SFG and attenuated total reflectance-Fourier transform infrared (ATR-FTIR) spectroscopy can determine orientations of complex proteins with greater certainty.[30] In this research, we used SFG and ATR-FTIR to study the membrane interactions of the N-terminal and C-terminal segments of GRK5 to gain insight into which regions were most important for membrane binding and what structure and orientation they adopt while interacting with membranes.

GRK5 residues 2–31 ($GRK5_{2–31}$) are highly conserved in the GRK4 subfamily of GRKs (Figure 4.1), which includes GRK4, GRK5 and GRK6. In previous literature, it was suggested that residues 22–29, which include basic amino acids Lys22, Arg23, Lys24, Lys26, Lys28, and Lys29, bind to PIP_2.[31] An overlapping region (residues 20–39) has also been implicated in binding to calmodulin Ca^{2+} (CaM Ca^{2+}).[32] The structure of GRK6 (a close homolog of GRK5) determined by X-ray crystallography suggests that the N-terminal portion of the peptide (residues 2 to 23) is disordered when the enzyme is in an inactive state,[33] but residues 2–18 become ordered when the enzyme assumes a more active, presumably receptor-bound conformation.[4] However, it is not known if this region forms a platform for binding to lipid membranes or activated GPCRs. Therefore, elucidating the ability of different segments of the GRK5 N-terminus with the membrane is the key to understand how the membrane influences GRK5 function.

GRK5-2-31: 2-ELENIVANTVLLKAREGGGGKRKGKSKKWK-31
GRK5-2-24: 2-ELENIVANTVLLKAREGGGGKRK-24
GRK5-25-31: 25-GKSKKWK-31
GRK5-546-565: 546-PKKGL LQRLFKRQHQ NNSKS-565

Figure 4.1 Sequences of the human GRK5 N-terminal and C-terminal peptides used in this study. Residues highlighted in red adopt an α helical conformation in the structure of the GRK6 sangivamycin complex.

The C terminal residues 552–562 of GRK5 are believed to be another region that interacts with phospholipids. Deletion of these residues results in a 100-fold loss in membrane binding affinity.[34] Residues 549–557 are predicted to form an amphipathic helix when bound to membranes.[35] In the active conformation of the GRK6 crystal structure, an amphipathic helix (residues 548–557) is observed that docks to the core of the enzyme, but is far removed from the predicted membrane surface and the N-terminal segment believed to bind PIP_2.[4] Thus, either this structural element does not bind to membranes, or it only binds to membranes when GRK6 is in a more inactive state, or the structure represents a soluble form of the enzyme, such as when it is believed to translocate to the nucleus to phosphorylate transcription factors.[36]

By combining data from two complementary optical spectroscopic techniques, SFG and ATR-FTIR, we are seeking to answer the following questions. First, do peptides representing the N-terminal ($GRK5_{2–31}$) and C-terminal ($GRK5_{546–565}$) regions bind to membranes on their own, and, if so, what structure do they adopt? Second, does PIP_2 affect the binding properties of these two peptides? Finally, is CaM Ca^{2+} able to dissociate these GRK5 peptides from the membrane, as proposed to be required for nuclear translocation?

4.2 Experimental Details

4.2.1. Materials

Peptides $GRK5_{2–31}$, $GRK5_{2–24}$ and $GRK5_{546–565}$ (Figure 4.1) were synthesized by Mosberg lab at the University of Michigan. Protected amino acids and N-methylpyrrolidone

(NMP), 1-hydroxybenzotriazole (HOBt), and O-benzotriazole-N,N,N',N'-tetramethyluronium hexafluorophosphate (HBTU) were purchased from Creosalus. Acetonitrile, HPLC grade water, trifluoroacetic acid (TFA), diethyl ether, and phenol were from Fisher Scientific. Piperidine, N,N-diisopropylethylamine (DIPEA), dimethylformamide (DMF), thioanisole, and triisopropylsilane (TIPS), and calmodulin were from Sigma/Aldrich. Solid-phase synthesis resin NovaPEG Rink Amide Resin (0.5 mmol/g) was purchased from Novabiochem. Analytical HPLC analysis was done using an Alliance system with 250 x 5 mm C18 3 μm column (Vydac). Mass spectrometry analysis was done using a 6130 Quadrupole LC/MS (Agilent Technologies). Semipreparative HPLC purification was performed using a Delta 600 system (Waters) with 150 x 19 mm XBridge™ Prep C18 10 μm OBD column (Waters). HPLC analysis and purification were done using solvent system 0.1 % TFA in water and 0.1% TFA in acetonitrile. Peptides $GRK5_{2–24}$ and $GRK5_{2–31}$ were synthesized using 9-fluorenylmethoxycarbonyl (FMOC) chemistry. The syntheses of C-terminal sequences up to Ala^{15} were carried out on a CS336X automated synthesizer (C.S. Bio Co.) and the syntheses were then continued on a Discover SPS single mode manual microwave synthesizer (CEM Corp.) (power = 20 W, 5 min per coupling and power 20 W, 1.5 min per deprotection; temps. 70-75 ˚C). The synthesis scale was 0.2 mmol. The general protocol included double coupling and double deprotection as well as acetylation of the un-reacted amino groups. Coupling cycles were performed using 4 eq. of incoming amino acid, HOBt/HBTU in DMF and DIPEA in NMP. Fmoc deprotection was accomplished using 20% piperidine solution in NMP. Cleavage of the peptide from the resin and side-chain deprotection was performed using 10 ml of the mixture: D.I. water:phenol:thioanisole:TIPS:TFA (0.5 ml:0.7 g:0.5 ml:0.25 ml:8.75 ml). The reaction was left running at room temperature for 2 h. After filtration of the resin, crude peptide was precipitated with cold ethyl ether. The resulting crude

peptides were purified by semipreparative HPLC, as described above. The purity of the final peptide was analyzed using HPLC and molecular weight confirmed by MS. Peptide $GRK5_{25–31}$ was synthesized by Peptide 2.0 Inc by a similar approach. POPC (1-palmitoyl-2-oleoyl-sn-glycero-3-phosphocholine) and PIP_2 were purchased from Avanti Polar Lipids.

4.2.2. SFG Experiments

SFG theory[39-43], our experimental design and data analysis method[23,44] has been reported before. Supported POPC/POPC lipid bilayers were constructed on CaF_2 prisms by Langmuir-Blodgett/Langmuir-Schaefer method, as described in Chapter 2.[37,38] The concentration of each of the four peptides was 3.8 μM and the peptides were dissolved in 10 mM potassium phosphate buffer (pH 7.4). Because CaF_2 prisms were used as substrates to prepare the lipid bilayers, small amounts of Ca^{2+} may be dissolved in the subphase. 2 mM EDTA was added to the above buffer solution to minimize any influence of the Ca^{2+} released from the CaF_2 substrates. For each of the three N-terminal peptides studied here, we added the peptide into the subphase in contact with the substrate supported bilayer and after equilibration recorded the SFG signal in the water O-H stretching frequency range as well as in the peptide amide I frequency region. For all peptides we studied, the adsorption time on the POPC lipid bilayer in either 10 mM phosphate buffer or PBS buffer was less than 200 s. For the second step, we substituted the peptide solution subphase with potassium phosphate buffer (~6 ml in total) to wash off the loosely associated peptides and recorded the SFG signal in the water O-H stretching frequency range again. For the last step, we substituted the phosphate buffer subphase with a solution of buffer containing 40% TFE and again collected SFG spectra in the water O-H stretching frequency range and the amide I frequency range. For the C-terminal peptide, we only perform the first two steps of the above procedure. PIP_2 experiments were performed in the same way as POPC experiments except that

when making bilayers, lipids with a 9:1 molar ratio of POPC:PIP_2 were used. Because peptides were used at the same concentration in these experiments yet likely have different affinities, and because water signals are also strongly affected by net charge as well as charge distribution in the peptides (and other effects), we defined peptides as weakly membrane associated if the water signal recovered after the buffer wash, as opposed to direct comparison of changes in the SFG signals from water O-H stretching after addition of peptide.

4.2.3 ATR-FTIR Spectroscopy

ATR-FTIR experiments were performed on a Nicolet Magna 550 FTIR spectrometer. Lipid bilayers were deposited on a ZnSe crystal (Specac Ltd. RI, U.K.) with vesicle fusion method. One ml POPC toluene solution (5 mg/ml) was dried with nitrogen flow and then in vacuum for 2 h. The POPC power was then dissolved in 10 mM phosphate D_2O buffer pH 7.4 and the mixture was vortexed for 5 min before addition to the surface of the detachable ZnSe crystal to form bilayers. After 30 min, the vesicles floating in the subphase were washed away by excessive buffer. GRK5 peptides were then injected into the subphase (1.6 ml) to achieve a concentration of 11.4 μM. After the system reached equilibrium, spectra before and after extensive wash with D_2O buffer were recorded. For $GRK5_{546-565}$, s- and p- polarized spectra were taken so that data analysis on the peptide orientation can be performed. In the CaM-Ca^{2+} experiments, after peptides were associated with the lipid bilayers equimolar CaM (11.4 μM) and 50 μM $CaCl_2$ solution were added.

4.3 Results

4.3.1 SFG Studies on N-terminal Peptides

We first investigated molecular interactions between the GRK5 N-terminal peptides $GRK5_{2–31}$, $GRK5_{2–24}$, and $GRK5_{25–31}$ and a POPC/POPC lipid bilayer. The POPC/POPC bilayer is zwitterionic, and the electrostatic potential across the bilayer induces the water dipoles to orient near the bilayer surface.[45,46] The water region (detected between 2700 and 3700 cm^{-1}) [47,48] monitored by SFG spectroscopy can be used to determine the binding properties of ions[49,50] or peptides.[25] In our experiments, we observed two broad water O-H stretching peaks centered at ~3200 cm^{-1} and 3400 cm^{-1} in the SFG spectrum from the lipid bilayer/potassium phosphate buffer interface (Figure 4.2a). Peptides were then added into the subphase and the system was allowed to reach equilibrium. The water OH stretching signal decreased upon addition of the $GRK5_{2–31}$ or $GRK5_{25–31}$ peptides to the subphase, consistent with their interaction with the POPC/POPC bilayers (Figures 4.2a and 4.3a). SFG spectra were also collected after extensive washing, but no substantial changes were observed, suggesting that both $GRK5_{2–31}$ and $GRK5_{25–31}$ peptides are strongly associated with the bilayer. However, the SFG water O-H stretching signal only decreased slightly after the addition of the $GRK5_{2-24}$ peptide to the subphase, and the SFG water signal recovered after washing the interface with buffer (Figure 4.3c), consistent with $GRK5_{2–24}$ only being loosely associated with the POPC/POPC bilayer. Thus, the highly charged residues spanning residues 25–31 are primarily responsible for membrane binding in these peptides.

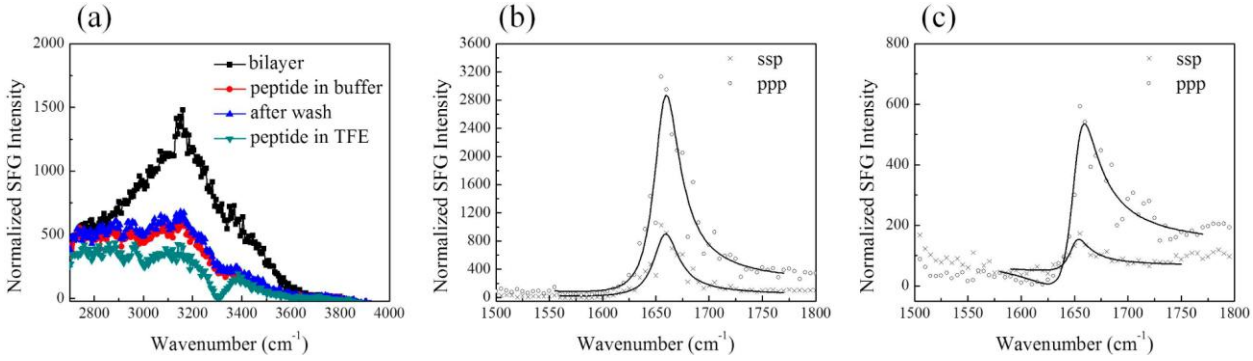

Figure 4.2 SFG signals from $GRK5_{2–31}$ indicate strong association with model membranes and helical character in a more hydrophobic environment. (a) Spectra in the C-H and O-H stretching frequency region detected from the interface between the POPC/POPC bilayer and buffer alone (black), $GRK5_{2–31}$ in 10 mM phosphate buffer pH 7.4 (red), after washing (blue), and in a mixture of 60% buffer/40% TFE (dark cyan). (b) SFG spectra of $GRK5_{2–31}$ associated with a POPC/POPC bilayer in contact with peptide solution in 60% 10 mM phosphate buffer pH 7.4/40% TFE in the amide I frequency region. (c) SFG spectra of $GRK5_{2–31}$ associated with a POPC/POPC bilayer in contact with 60% PBS/40% TFE.

For all the three GRK5 N-terminal peptides, no discernible SFG amide I signal could be detected from the lipid bilayer interfaces after their addition to the subphase solution. This suggests that the membrane associated peptides form either ordered structures but with random orientations, or essentially random structures. After replacing the subphase with a 40% TFE solution, a strong SFG amide I signal was detected from the $GRK5_{2–31}$ peptide (Figure 4.2b), but not from $GRK5_{25–31}$ or $GRK5_{2–24}$ (Figures 4.3b and 4.3d), consistent with only $GRK5_{2–31}$ forming α-helical structure when the subphase becomes more hydrophobic. This conclusion is also consistent with spectral features detected in the water O-H stretching frequency range after the subphase buffer was replaced by the TFE mixture. Figure 4.2a shows that only for $GRK5_{2–31}$, a negative peak at ~3300 cm^{-1} appeared, originating from the interference between the N-H stretching signals of well-ordered α-helices and the broad water background. This N-H stretch signal can be attributed to the backbone N-H stretch or/and the side chains such as Lys NH_3^+.[51] Although predicted helical propensity of $GRK5_{2-24}$ is the same as of - $GRK5_{2–31}$, no changes in the spectra upon addition of TFE were detected likely because the peptide was not strongly associated with the membrane and washed off in the previous step.

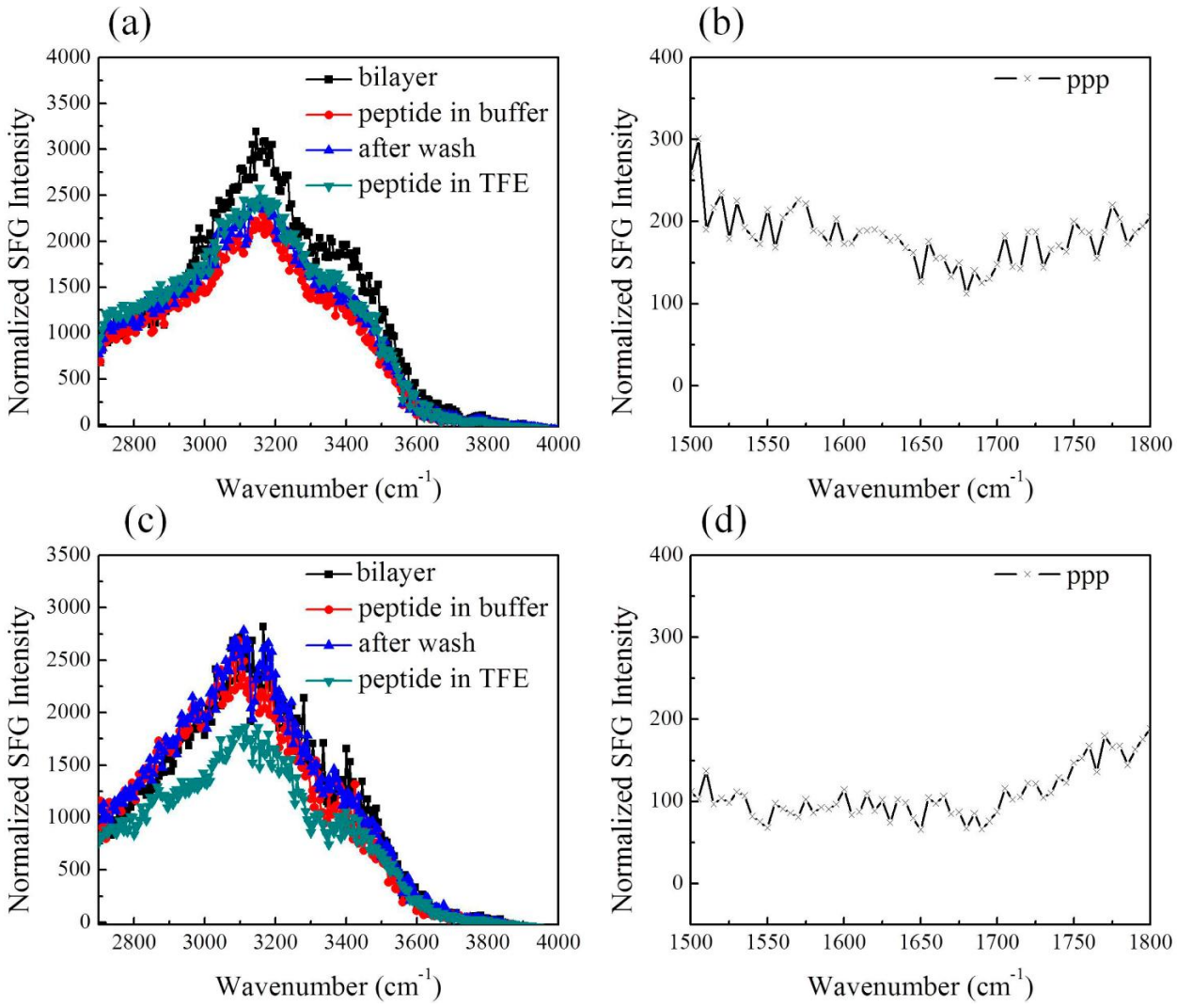

Figure 4.3 SFG ppp signals detected from the $GRK5_{25–31}$ and $GRK5_{2-24}$ peptides indicate that the latter peptide only weakly associates with model membranes. (a) SFG spectra in C-H and O-H stretching frequency region from the interface between the POPC/POPC bilayer and buffer alone (black), $GRK5_{25–31}$ in 10 mM phosphate buffer pH 7.4 (red), after washing (blue), and in a mixture of 60% buffer/40% TFE (dark cyan). (b) SFG spectra in the amide I frequency region from $GRK5_{25-31}$ associated with a POPC/POPC bilayer in 60% 10 mM phosphate buffer pH 7.4/40% TFE. (c) SFG spectra in C-H and O-H stretching frequency region from the interface between the POPC/POPC bilayer and buffer alone (black), $GRK5_{2–24}$ in 10 mM phosphate buffer pH 7.4 (red), after washing (blue), and in a mixture of 60% buffer/40% TFE. (d) SFG spectra in the amide I frequency region from $GRK5_{2-24}$ associated with a POPC/POPC bilayer in contact with peptide solution in 60% 10 mM phosphate buffer pH 7.4/40% TFE.

4.3.2 Orientation Analysis of the α-helical Segment in $GRK5_{2–31}$

After substituting the subphase with 40% TFE, a prominent α-helical signal centered at ~1655 cm^{-1} arises from $GRK5_{2–31}$. This could be interpreted as residues 2-18 adopting an α-helical conformation, consistent with a prior crystal structure of GRK6[4] and secondary structure predictions. This phenomenon also highlights that SFG, as a second order nonlinear spectroscopy, is much more sensitive to ordered structure (such as α-helices) than disordered molecules (such as random coils), which is not the case for linear vibrational spectroscopy such as ATR-FTIR.

SFG spectra collected from amide I modes of peptides and proteins using different polarization combinations can be used to determine membrane orientations of peptides and proteins, as shown in a previous publication.[22] The calculation details were described in Chapter 1. Using the measured signal strength ratio of the α-helical contribution in the ppp and ssp spectra, we deduced that in 40% TFE, the orientation angle of the helical segment (presumed to be residues 2-18) of $GRK5_{2–31}$ is ~46±1˚ relative to the membrane surface normal (with χ_{ppp}/χ_{ssp} =2.08±0.01) if we assume the peptides adopt a single orientation distribution. Interestingly, this orientation angle increases to ~78±11˚ (with χ_{ppp}/χ_{ssp} =2.43±0.06) when the ionic strength of the subphase is increased by use of PBS instead of phosphate buffer (Table 4.1). This result suggests that the increase in ionic strength does not change the conformation of the $GRK5_{2–31}$ but rather changes the charge distribution on the peptide surface and thus facilitates the interaction of helical elements of the peptide with the lipid head groups.

Subphase	Polarization	Peak center (cm^{-1})	Peak Width (cm^{-1})	χ_{eff}	Ratio	Tilt angle
60% phosphate buffer/40% TFE	ssp	1657	14.2	14.8	2.09±0.01	46±1 ˚
	ppp	1657	14.7	51.1		
PBS buffer/40% TFE	ssp	1650	11.0	8.8	2.43±0.06	78±11 ˚
	ppp	1652	14.0	17.6		

Errors represent standard deviations of four replicates obtained in each of two individual experiments.

Table 4.1 Fitting results for SFG spectra shown in Figure 4.2.

4.3.3 SFG Studies on the C-terminal Peptide

The SFG spectrum of $GRK5_{546–565}$ (Figure 4.4) is similar to that of $GRK5_{2–31}$, in that the two broad peaks at 3200 cm^{-1} and 3400 cm^{-1} decreased and remained so even after extensive washing, indicating strong interaction of $GRK5_{546–565}$ with the lipid bilayer. However, two new peaks centered at 2876 cm^{-1} and 2940 cm^{-1} appeared. These were also observed for $GRK5_{2–31}$, but were not as significant. These two peaks could be attributed to amino acid side chains[51], disruption of the lipid bilayer[52], or both. The SFG amide I spectra of $GRK5_{546–565}$, however, is very different from those of the N-terminal peptides. Without changing the subphase into 40% TFE, an amide I signal was readily detected. In the spectra, the peak at 1655 cm^{-1} is attributed to α-helical structure and the shoulder at ~1600 cm^{-1} is likely from amide groups of side chains.[53] The peak at 1720 cm^{-1} is from carbonyl groups in the disrupted lipid bilayer. This agrees with the CH stretching signal change mentioned above, supporting the hypothesis that the lipid bilayer is disrupted. Because the intensity is not as high as that of $GRK5_{2-31}$ in 40% TFE with 10 mM phosphate buffer, no discernible NH peak (~3300 cm^{-1}) in the water range (3000-4000 cm^{-1}) was detected. Orientation analysis was not performed here due to the low signal-noise ratio of the SFG spectra and because there are multiple contributions to the spectra. In summary, the main difference between $GRK5_{546-565}$ and $GRK5_{2–31}$ is that the former is partially α-helical when associated with lipid bilayers without need for TFE to induce helical structure.

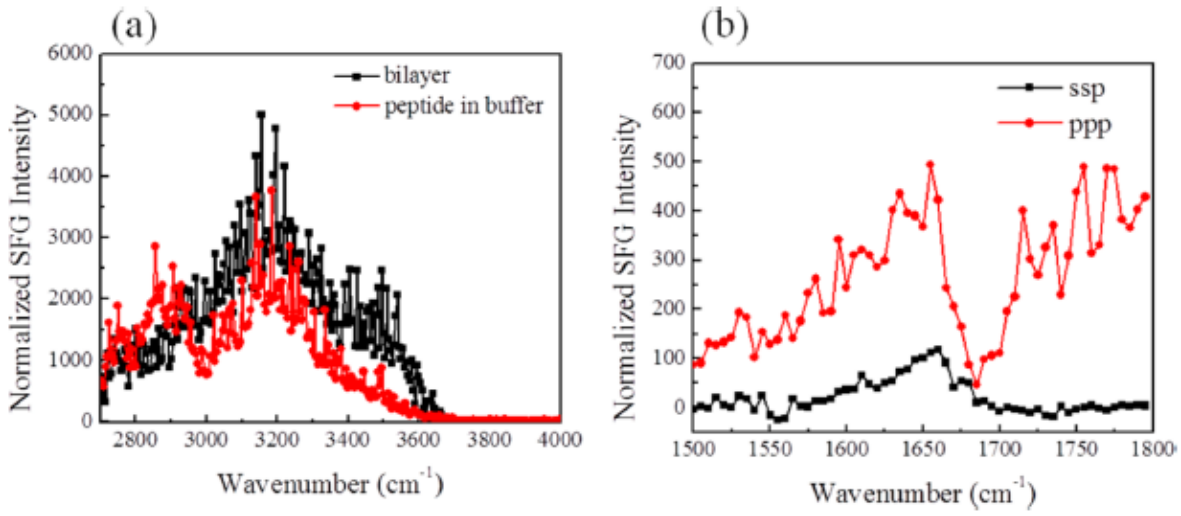

Figure 4.4 SFG ppp signals detected from $GRK5_{546–565}$ indicate strong binding to model membranes and helical character. (a) SFG spectra in the C-H and O-H stretching frequency region from the interface between the POPC/POPC bilayer and buffer alone (black), and $GRK5_{546–565}$ associated in 10 mM phosphate buffer pH 7.4 (red). (b) SFG spectra in the amide I frequency region from $GRK5_{546–565}$ associated with a POPC/POPC bilayer in 10 mM phosphate buffer pH 7.4.

4.3.4 SFG Studies on the Effect of PIP_2

PIP_2 is known to enhance the GRK5-mediated phosphorylation of GPCRs.[31] In order to test whether this enhancement is related to the membrane binding of the peptides we are studying herein, we constructed (9:1) POPC:PIP_2 lipid bilayers and studied its interaction with $GRK5_{2–31}$, $GRK5_{2–24}$ and $GRK5_{546–565}$. These results (see Figure 4.5) were then compared to those obtained when using a pure POPC lipid bilayer. The SFG intensities and signal strength ratios of the amide I signals detected in the amide I frequency range using different polarization combinations of the $GRK5_{2–31}$ associated with the two types of bilayers exposed to the solution with 40% TFE were observed to be similar, indicating that PIP_2 did not enhance the adsorption of $GRK5_{2–31}$ to the lipid bilayer. The interactions of $GRK5_{2–24}$ and $GRK5_{546–565}$ with (9:1) POPC:PIP_2 bilayers were also similar to those with the pure POPC system. This is reminiscent of protein MARCKS: neither the native protein nor a peptide representing its positive charged cluster requires PIP_2 for

binding to the membrane. However, PIP_2 is laterally sequestered in the presence of MARCKS and the peptide.[54] How PIP_2 can increase the autophosphorylation of GRK5 and phosphorylation of activated GPCRs calls for further investigation. However, it should be noted that residues 24-31 are well ordered in both available crystal structures of GRK6,[4,33] and that formation of a high affinity site for PIP_2 may require the assumption of tertiary structure by this polypeptide, as mandated by the fold of the enzyme. The study on the effect of PIP_2 suggests that the conclusions on peptide affinity drawn from our previously spectroscopy results doesn't require the existence of PIP_2.

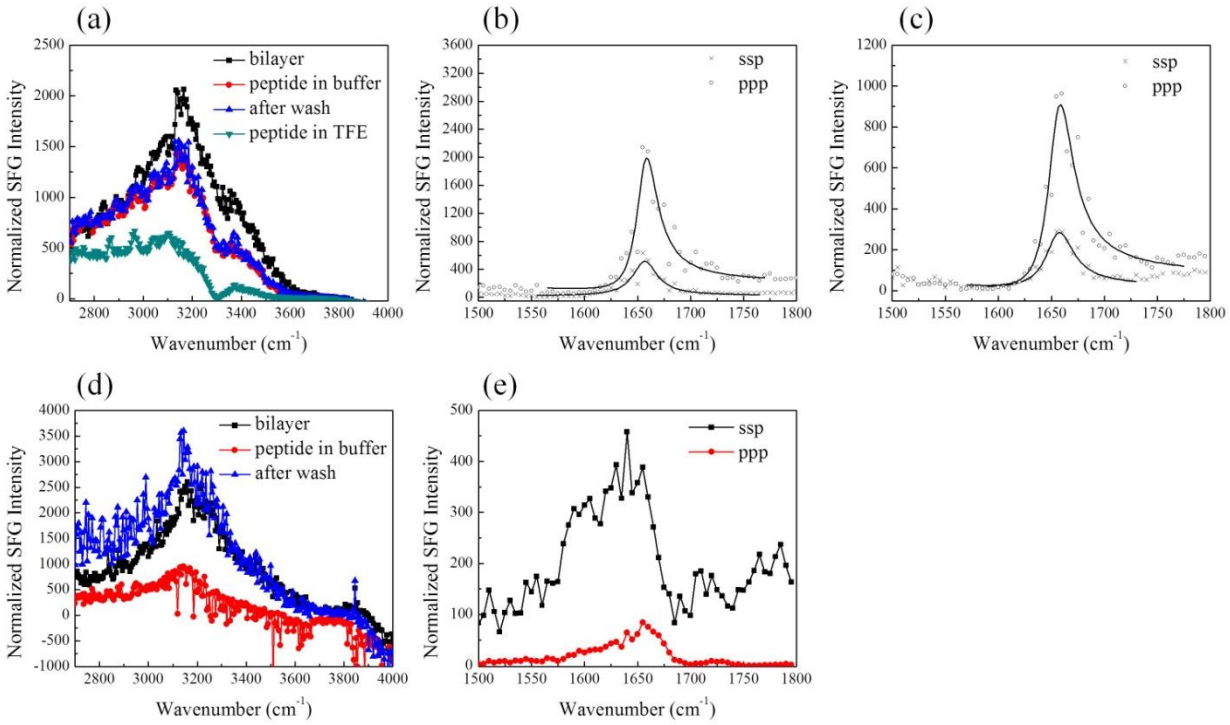

Figure 4.5 Influence of PIP_2 on membrane binding properties of GRK5 peptides. (a) SFG signals in the C-H and O-H stretching frequency region detected from the interface between the POPC:PIP_2 (9:1) lipid bilayer and buffer alone (black), upon addition of $GRK5_{2–31}$ in 10 mM phosphate buffer pH 7.4 (red), after washing (blue), and in 60% buffer/40% TFE (dark cyan). (b) SFG signals in the amide I frequency region from $GRK5_{2–31}$ associated with a POPC:PIP_2 (9:1) bilayer in contact with peptide solution in 10 mM 60% phosphate buffer pH 7.4/40% TFE. (c) SFG signals in the amide I frequency region from $GRK5_{2–31}$ associated with a POPC:PIP_2 (9:1) bilayer in contact with 60% PBS

buffer/40% TFE. (d) SFG signals in the C-H and O-H stretching frequency region from the interface between the POPC:PIP_2 (9:1) lipid bilayer and buffer alone (black), in the presence of $GRK5_{2–24}$ (red), and 10 mM phosphate buffer after washing (blue) (e) SFG amide I spectra for $GRK5_{546–565}$ associated with a POPC:PIP_2 (9:1) bilayer in 10 mM phosphate buffer pH 7.4.

4.3.5 ATR-FTIR Studies

Because SFG is sensitive to ordered structures, the signals generated from ordered α-helices are normally much stronger than those detected from random coil. On the other hand, ATR-FTIR spectroscopy detects amide I (1600 cm^{-1} to 1700 cm^{-1}) signals with similar sensitivities from different secondary structural motifs, such as α-helices, random coils and β-sheets from peptides and proteins.[55-59] We used ATR-FTIR spectra to confirm the peptide adsorption behavior detected by SFG. For the ATR-FTIR experiments, the concentrations of all peptides used were 11.4 μM, dissolved in 10 mM phosphate D_2O buffer (pD 7.1). For all the N terminal peptides, the amide I peak center is around 1642 cm^{-1} (Figure 4.5), indicating that the peptides are most likely random coils. For $GRK5_{2–31}$ and $GRK5_{25–31}$, the amide I peak intensities did not change after wash with buffer, but for $GRK5_{2–24}$ the amide I signal decreased to about half, again suggesting a weaker interaction between $GRK5_{2–24}$ and the lipid bilayer, as suggested by the SFG studies. The reason that membrane associated $GRK5_{2–24}$ did not disappear after washing, as observed in SFG, is likely because the peptide concentration is three times higher than that used in SFG measurements.

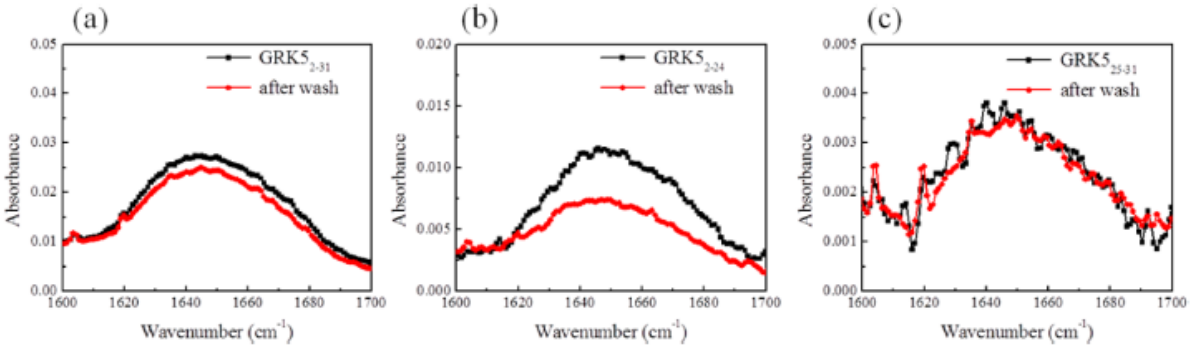

Figure 4.5 ATR-FTIR spectra of GRK5 N-terminal peptides confirm weak binding of $GRK5_{2–24}$. Spectra of (a) $GRK5_{2–31}$, (b) $GRK5_{2–24}$, (c) $GKR5_{25–31}$ associated with a POPC/POPC lipid bilayer in presence of 10 mM phosphate buffer pH 7.4 before (black) and after (red) buffer wash.

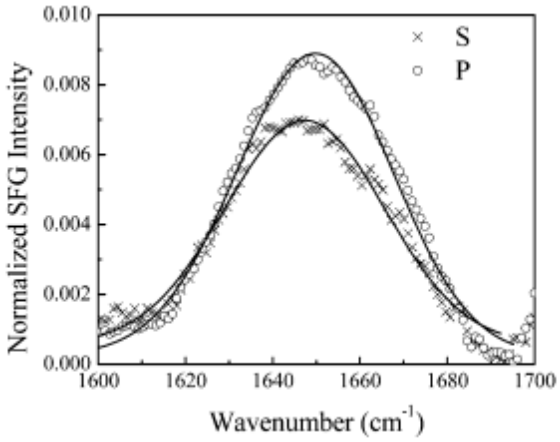

Figure 4.6 ATR-FTIR spectra of $GRK5_{546-565}$ associated with a POPC/POPC lipid bilayer in contact with 10 mM phosphate buffer pH 7.4.

By taking secondary derivatives of the ATR-FTIR spectra for $GRK5_{546-565}$ (Figure 4.6), we found two peaks centered at 1646 cm^{-1} and 1653 cm^{-1}, respectively. The average band position in D_2O is reported to be ~1652 cm^{-1} for α-helix and ~1645 cm^{-1} for disordered secondary structure.[57] Therefore, the peak centered at 1646 cm^{-1} is assigned to be contributed by random coil and the other at 1653 cm^{-1} is attributed to α-helices, consistent with SFG results indicating that the GRK5 C-terminal peptide forms an α-helical structure. After extensive washing, the ATR-FTIR signal remained, suggesting a strong interaction with the lipid bilayer, also compatible with the SFG data.

4.3.6 ATR-FTIR Studies of CaM Ca^{2+} Interactions with N-terminal and C-terminal Peptides

ATR-FTIR was further used to investigate the molecular interactions of $GRK5_{2-31}$ with calmodulin. CaM Ca^{2+} itself has very weak binding with the membrane. As shown in Figure 4.6a, the addition of equimolar amounts of CaM Ca^{2+} and $GRK5_{2-31}$ to the subphase decreased the ATR-FTIR amide I signal by about 50%. Further extensive washing with buffer led to a more substantial decline of the random coil ATR-FTIR signal. This clearly shows that CaM Ca^{2+} facilitates the extraction of $GRK5_{2-31}$ from the lipid bilayer. However, CaM Ca^{2+} could not extract $GRK5_{25-31}$ from the membrane (Figure 4.7), suggesting that the helix formed by residues 2-24 is important for high affinity binding to CaM Ca^{2+}.[60] CaM Ca^{2+} also was able to extract $GRK5_{546-565}$ from our model membranes (Figure 4.6b). The initial increase in the signal after addition of CaM Ca^{2+} to $GRK5_{546-565}$ was unexpected. However, this may simply reflect that when CaM Ca^{2+} forms a complex with this peptide, it remains associated with the membrane to a greater extent than when in complex with the $GRK5_{2-31}$ peptide. Notably, in either case, the subsequent buffer wash eliminates binding, indicating weak binding.

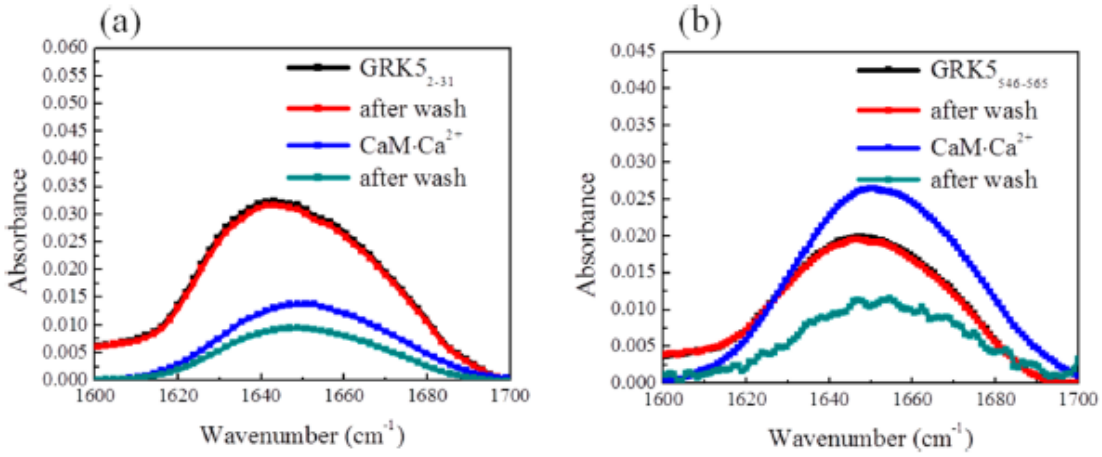

Figure 4.7 CaM Ca^{2+} decreases the association of GRK5 N and C-terminal peptides. ATR-FTIR signals detected before and after the addition of equimolar CaM Ca^{2+} to the

subphase for peptides a) GRK5$_{2–31}$ and b) GRK5$_{546–565}$. The spectra correspond to before (black), and after (red) washing, to the addition of CaM·Ca^{2+} to the subphase (blue), and after subsequent washing (dark cyan).

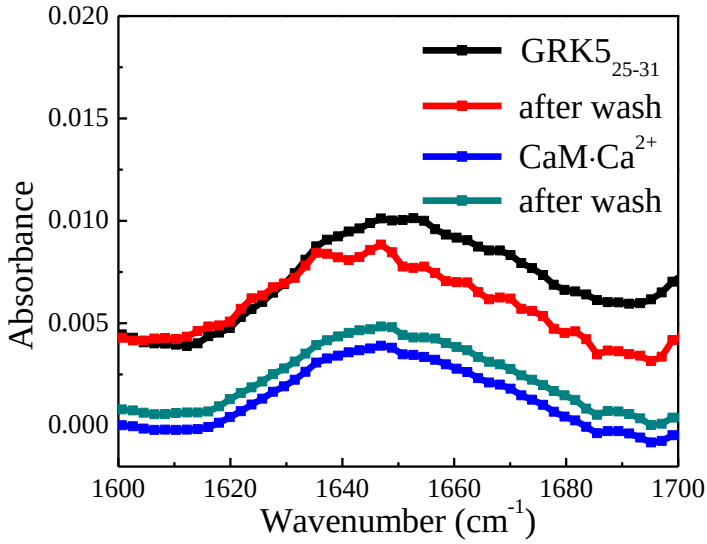

Figure 4.8 ATR-FTIR signals detected before and after the addition of equimolar CaM·Ca^{2+} to the subphase for GRK5$_{25–31}$. ATR-FTIR spectra represent signals collected from peptides associated with the lipid bilayer before (black), after washing (red), after the addition of CaM·Ca^{2+} to the subphase (blue), and after subsequent washing (dark cyan).

4.4. Discussion

Our study is a clear example of how SFG and ATR-FTIR spectroscopies complement each other as methods for interrogating the structure of proteins/peptides at membrane surfaces. Because SFG is a second order nonlinear optical technique, under the electric dipole approximation, it only detects signal where inversion symmetry is broken. Thus, SFG can minimize the interfering effects of proteins in the bulk solution. For example, in our studies, we measured well-defined amide signals using SFG from the GRK5$_{2–31}$ peptide associated with lipid bilayers in contact with solutions with 40% TFE, which generates a high background signal in ATR-FTIR spectroscopy. Another advantage of SFG is that measurements do not require D_2O, which is used in ATR-FTIR to minimize interference by H_2O absorption at ~1650 cm^{-1}. SFG is

also more sensitive to ordered secondary structures than disordered ones. We observed a drastic change of the amide I signal of $GRK5_{2–31}$ when its subphase was altered to contain 40% TFE. This change was more subtle in the ATR-FTIR spectra because random coils and α-helices have peak centers close to each other (~1647 cm^{-1} and ~1653 cm^{-1} respectively) and usually they make similar contributions to the spectra. For large proteins (e.g., GRK5), sometimes the switch from the active state to the inactive state is accompanied by conformational changes. The unique ability of SFG to distinguish random coils from α-helices might shed light on unveiling the mechanisms of these processes, which may not be easily distinguishable using ATR-FTIR spectra. On the other hand, ATR-FTIR can directly monitor the adsorption of unstructured peptides and proteins simply by inspecting the amide I signals. Because unstructured domains (e.g., random coils) cannot be readily detected by SFG spectroscopy, the adsorption of such molecules cannot be directly assessed using the SFG amide I signal. However, this goal can be achieved indirectly by monitoring the ordered water signal change in SFG spectra.

4.5 Conclusion

In this chapter we combined SFG and ATR-FTIR spectroscopies to study the *in situ* membrane binding potential of two regions of GRK5 previously implicated in binding to phospholipid bilayers. The uniform orientation of water molecules near the bilayer surface was exploited first, as the disappearance of SFG water signal suggests their displacement by peptide molecules. Whether or not the water signal would resume after washing the system with buffer was used to determine if the peptide molecules are weakly or strongly adsorbed. It was shown that of the three N-terminal peptides, only $GRK5_{2–24}$ binds weakly to the lipid bilayer, suggesting that $GRK5_{2–24}$ alone does not play a significant role in GRK5 membrane binding and that residues 25–31 of the $GRK5_{2–31}$ peptide, which are exceptionally basic and include a large

hydrophobic tryptophan residue, are primarily responsible for membrane binding in this region. This conclusion is also supported by monitoring the changes in the amide I signal from the peptides before and after washing with buffer using ATR-FTIR. From the amide I SFG signals, we found that the segment containing amino acid residues 2–24 of peptide $GRK5_{2–31}$ undergoes a conformational change from a random coil into a well-ordered α-helix when the hydrophobicity of the environment increases (in our experiment by substituting the buffer subphase with a solution containing 40% TFE). It is possible that TFE emulates what happens when this region encounters either an activated GPCR or its own activated kinase domain. Furthermore, the interaction of this region, or of an adjacent region (i.e. residues 25–31), with membranes is not enough to induce order in this segment. Our results are consistent with those reported previously that residues 2 to 18 play an important role in protein-protein interactions, such as those with activated GPCRs or with the catalytic core of the enzyme to stabilize a more active state.[4, 2] Polarization-dependent SFG measurements were used to determine the angle of the helical segment of this peptide to the surface normal. This angle was found to increase substantially upon an increase in ionic strength of the surrounding buffer solution. With a similar approach, both SFG and ATR-FTIR results showed that $GRK5_{546–565}$ was partially helical on POPC lipid bilayers, even in the absence of a helix-inducing agent such as TFE. A model summarizing the membrane interactions of the peptides is shown in Figure 4.8.

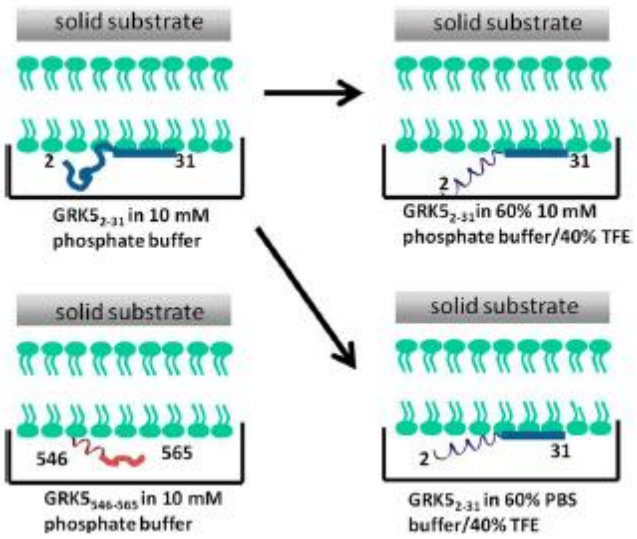

Figure 4.9 Schematic showing proposed membrane interaction mechanisms of the GRK5 N terminal peptide GRK5$_{2–31}$ and the GRK5 C terminal peptide GRK5$_{546–565}$.

Therefore, both N-and C-terminal peptide segments of GRK5 contribute to bilayer binding, and likely account for the constitutive localization of GRK5 on cell membranes, even though it lacks the palmitoylation found in the closely related enzymes GRK4 and GRK6. Both residues 25-31 and 546–565 bind strongly to membranes, as evidenced by their persistence even after exhaustive washing. However, residues 2–24 at the extreme N-terminus do not represent a strong membrane binding determinant. Instead, our results are most consistent with this highly conserved region only becoming ordered when it forms protein–protein interfaces, such as when in complex with an activated GPCR or when it interacts with the small lobe of the GRK kinase domain. Unexpectedly, PIP_2 does not affect the binding properties of the peptides we studied. It is possible that the N-terminal peptide does not fully recapitulate the binding site for this lipid because the peptide is unstructured when bound to membranes, as opposed to the analogous peptide in the context of the full-length enzyme, where its structure is imposed by the fold of the enzyme. The membrane interaction mechanisms of the N-terminal and C-terminal peptides are,

however, different. Previous biochemical studies showed that the C-terminal peptide likely forms an amphipathic helix that enhances GRK5 membrane binding.[35] The analogous C-terminal region has only been observed in one structure of GRK6 in a relatively active state,[4] wherein it forms the expected amphipathic helix. However, the hydrophobic residues bind to the catalytic core of the enzyme, and the helix seems too far from the predicted membrane surface to directly engage lipids. As phospholipids are not present in this crystal structure, the C-terminal structure could represent a crystallographic artifact. Alternatively, because the interactions of the C-terminus of GRK6 with the core of the enzyme are extensive (buried accessible surface area of 2400 $Å^2$), the packing of this helix could represent the situation when GRK6 is in a cytoplasmic and/or autoinhibited state. Because PIP_2 is believed to bind to the 25-31 region in the N-terminal region and this site is a structured part of the catalytic core in prior crystal structures, this interaction may be more important for achieving proper orientation of the enzyme at the membrane, whereas the C-terminal amphipathic helix, which is connected to the rest of the enzyme by a 21-amino acid linker, is merely important for maintaining its association at the membrane. CaM·Ca^{2+} is able to dissociate $GRK5_{2-31}$ and $GRK5_{546–565}$ peptides from the membrane, consistent with the ability of this protein to drive GRK5 off the membrane of cells and consequently to the nucleus, where it is believed to phosphorylate transcription factors controlling hypertrophic genes.[36]

4.6. References

(1) Neves, S. R.; Ram, P. T.; Iyengar, R. *Science* **2002**, *296*, 1636–1639.

(2) Homan, K. T.; Glukhova, A; Tesmer, J. J. G. *Curr. Med. Chem.* **2013**, *20*, 39–46.

(3) Gurevich, E. V.; Tesmer, J. J. G.; Mushegian, A.; Gurevich, V. V. *Pharmacol. Therapeut.* **2012**, *133*, 40–69.

(4) Boguth, C. A; Singh, P.; Huang, C.; Tesmer, J. J. G. *EMBO. J.* **2010**, *29*, 3249–3259.

(5) Noble, B.; Kallal, L. A.; Pausch, M. H.; Benovic, J. L. *J. Biol. Chem.* **2003**, *278*, 47466–47476.

(6) Pao, C. S.; Barker, B. L.; Benovic, J. L. *Biochemistry* **2009**, *48*, 7325–7333.

(7) Phillips, D. C.; York, R. L.; Mermut, O.; McCrea, K. R.; Ward, R. S.; Somorjai, G. A. *J. Phys. Chem. C* **2007**, *111*, 255–261.

(8) York, R. L.; Holinga, G. J.; Somorjai, G. A. *Langmuir* **2009**, *25*, 9369–9374.

(9) Weidner, T.; Apte, J. S.; Gamble, L. J.; Castner, D. G. *Langmuir* **2010**, *26*, 3433–3440.

(10) Weidner, T.; Castner, D. G. *Phys. Chem. Chem. Phys.* **2013**, *15*, 12516–12524.

(11) Breen, N. F.; Weidner, T.; Li, K.; Castner, D. G.; Drobny, G. P. *J. Am. Chem. Soc.* **2009**, *131*, 14148–14189.

(12) Weidner, T.; Breen, N. F.; Li, K.; Drobny, G. P.; Castner, D. G. *P. Natl. Acad. Sci.USA.* **2010**, *107*, 13288–13293.

(13) Jung, S.-Y.; Lim, S.-M.; Albertorio, F.; Kim, G.; Gurau, M. C.; Yang, R. D.; Holden, M. A; Cremer, P. S. *J. Am. Chem. Soc.* **2003**, *125*, 12782–12786.

(14) Campen, R. K.; Ngo, T. T. M.; Sovago, M.; Ruysschaert, J. M.; Bonn, M. *J. Am. Chem. Soc.* **2010**, *132*, 8037-8047.

(15) Engel, M. F. M.; vandenAkker, C. C.; Schleeger, M.; Velikov, K. P.; Koenderink, G. H.; Bonn, M. *J. Am. Chem. Soc.* **2012**, *134*, 14781–14788.

(16) Tong, Y.; Li, N.; Liu, H.; Ge, A.; Osawa, M.; Ye, S. *Angew. Chem. Int. Ed.* **2010**, *49*, 2319–2323.

(17) Fu, L.; Liu, J.; Yan, E. C. Y. *J. Am. Chem. Soc.* **2011**, *133*, 8094–8097.

(18) Fu, L.; Ma, G.; Yan, E. C. Y. *J. Am. Chem. Soc.* **2010**, *132*, 5405–5412.

(19) Diaz, A. J.; Albertorio, F.; Daniel, S.; Cremer, P. S. *Langmuir* **2008**, *24*, 6820–6826.

(20) Volkov, V.; Bonn, M. *J. Phys. Chem. B.* **2013**, Article ASAP.

(21) Roeters, S. J.; Dijk, C. N. van; Torres-Knoop, A; Backus, E. H. G.; Campen, R. K.; Bonn, M.; Woutersen, S. *J. Phys. Chem. A.* **2013**, *117*, 6311–6322.

(22) Nguyen, K. T.; Clair, S. V Le; Ye, S.; Chen, Z. *J. Phys. Chem. B.* **2009**, *113*, 12169–12180.

(23) Ding, B.; Chen, Z. *J. Phys. Chem. B.* **2012**, *116*, 2545–2552.

(24) Chen, X.; Wang, J.; Boughton, A. P.; Kristalyn, C. B.; Chen, Z. *J. Am. Chem. Soc.* **2007**, *129*, 1420–1427.

(25) Ding, B.; Soblosky, L.; Nguyen, K.; Geng, J.; Yu, X.; Ramamoorthy, A.; Chen, Z. *Sci. Rep.* **2013**, *3*, 1854.

(26) Xiao, D.; Fu, L.; Liu, J.; Batista, V. S.; Yan, E. C. Y.*J. Mol. Biol.* **2012**, *421*, 537–547.

(27) Ye, S.; Nguyen, K. T.; Chen, Z. *J. Phys. Chem. B.* **2010**, *114*, 3334–3340.

(28) Boughton, A. P.; Yang, P.; Tesmer, V. M.; Ding, B.; Tesmer, J. J. G.; Chen, Z. *P. Natl. Acad. Sci.USA.* **2011**, *108*, E667–E673.

(29) Chen, X.; Boughton, A. P.; Tesmer, J. J. G.; Chen, Z. *J. Am. Chem. Soc.* **2007**, *129*, 12658–12659.

(30) Yang, P.; Boughton, A.; Homan, K. T.; Tesmer, J. J. G.; Chen, Z. *J. Am. Chem. Soc.* **2013**, *135*, 5044−5051.

(31) Pitcher, J. A.; Fredericks, Z. L.; Stone, W. C.; Premont, R. T.; Stoffel, R. H.; Koch, W. J.; Lefkowitz, R. J.*J. Biol. Chem.* **1996**, *271*, 24907–24913.

(32) Pronin, A. N.; Satpaev, D. K.; Slepak, V. Z.; Benovic, J. L. *J. Biol. Chem.* **1997**, *272*, 18273–18280.

(33) Lodowski, D. T.; Tesmer, V. M.; Benovic, J. L.; Tesmer, J. J. G. *J. Biol. Chem.* **2006**, *281*, 16785–16793.

(34) Pronin, A. N.; Carman, C. V; Benovic, J. L. *Biochemistry* **1998**, *273*, 31510–31518.

(35) Thiyagarajan, M. M.; Stracquatanio, R. P.; Pronin, A. N.; Evanko, D. S.; Benovic, J. L.; Wedegaertner, P. B. *J. Biol. Chem.***2004**, *279*, 17989–17995.

(36) Gold, J. I.; Martini, J. S.; Hullmann, J.; Gao, E.; Chuprun, J. K.; Lee, L.; Tilley, D. G.; Rabinowitz, J. E.; Bossuyt, J.; Bers, D. M.; Koch, W. J. *PLoS One.* **2013**, *8*, e57324.

(37) Ye, S.; Nguyen, K. T.; Clair, S. V Le; Chen, Z.*J. Strut. Biol.* **2009**, *168*, 61–77.

(38) Liu, J.; Conboy, J. C. *J. Am. Chem. Soc.* **2004**, *126*, 8376–8377.

(39) Gan, W.; Wu, D.; Zhang, Z.; Feng, R.; Wang, H. *J. Chem. Phys.* **2006**, *124*, 114705.

(40) Chen, Z.; Shen, Y. R.; Somorjai, G. A. *Annu. Rev. Phys. Chem.* **2002**, *53*, 437–465.

(41) Zhuang, X.; Miranda, P.; Kim, D.; Shen, Y. *Phys. Rev. B.* **1999**, *59*, 12632–12640.

(42) Moad, A. J.; Simpson, G. J. *J. Phys. Chem. B.* **2004**, *108*, 3548–3562.

(43) Moad, A. J.; Moad, C. W.; Perry, J. M.; Wampler, R. D.; Goeken, G. S.; Begue, N. J.; Shen, T.; Heiland, R.; Simpson, G. J. *J. Comput. Chem.* **2007**, *28*, 1996-2002.

(44) Nguyen, K. T.; Clair, S. V Le; Ye, S.; Chen, Z. *J. Phys. Chem. B.* **2009**, *113*, 12358–12363.

(45) Böckmann, R. A; Hac, A.; Heimburg, T.; Grubmüller, H. *Biophys. J.* **2003**, *85*, 1647–1655.

(46) Gurtovenko, A. A; Vattulainen, I. *J. Phys. Chem. B.* **2008**, *112*, 1953–1962.

(47) Jena, K. C.; Hore, D. K. *J. Phys. Chem. C.* **2009**, *113*, 15364–15372.

(48) Jena, K. C.; Hore, D. K. *Phys. Chem. Chem. Phys.* **2010**, *12*, 14383–14404.

(49) Okur, H. I.; Kherb, J.; Cremer, P. S. *J. Am. Chem. Soc.* **2013**. 135, 5062-5067.

(50) Yang, Z.; Li, Q.; Chou, K. C. *J. Phys. Chem. C* **2009**, 8201–8205.

(51) Mermut, O.; Phillips, D. C.; York, R. L.; McCrea, K. R.; Ward, R. S.; Somorjai, G. A. *J. Am. Chem. Soc.* **2006**, *128*, 3598–3607.

(52) Ge, A.; Wu, H.; Darwish, T. A; James, M.; Osawa, M.; Ye, S. *Langmuir* **2013**, *29*, 5407–5417.

(53) Tamm, L. K.; Tatulian, S. A. *Q. Rev. Biophys.* **1997**, *30*, 365–429.

(54) McLaughlin, S.; Murray, D. *Nature* **2005**, *438*, 605–611.

(55) Frey, S.; Tamm, L. K. *Biophys. J.* **1991**, *60*, 922-930.

(56) Tamm, L. K,; Tatulian, S. A. *Q. Rev. Biophys*. **1997**, *30*, 365-429.

(57) Barth, A.; Zscherp, C. *Q. Rev. Biophys*, **2002**, *35*, 369-430

(58) Heimburg, T.; Schunemann, J.; Weber, K.; Geisler, N. *Biochemistry* **1999**, *38*, 12727-12734.

(59) Wang, J.; Chen, J.; Hochstrasser, R. M. *J. Phys. Chem. B.* **2006**, *110*, 7545-7555.

(60) Rhoads, R.; Friedburg, F. *FASEB* **1997**, *11*, 331–340.

CHAPTER 5

SITE-SPECIFIC ORIENTATION OF AN α-HELICAL PEPTIDE OVISPIRIN-1 DEDUCED FROM ISOTOPE LABELED SFG SPECTROSCOPY

In Chapter 4, we used a method to study the interfacial behaviors of different segments within one peptide by investigating each peptide segment using SFG and ATR-FTIR. Now we further ask whether SFG is sensitive enough to detect structural information, such as the orientation of one single amino acid segment in a peptide backbone, so that we can probe local structures of biomolecules at interfaces. We will address this question by examining a peptide ovisprin-1 by combining SFG and isotope labeling techniques. Ovisprin-1 is an 18-residue α-helix with antimicrobial activity and serves as a model molecule to demonstrate that SFG has the ability to elucidate the interfacial orientation of a single-residue within a peptide. I have successfully detected SFG signal from a $^{13}C=O$ labeled residue of ovisprin-1 on polymer surfaces. This is the first time that signal contributed by a single $^{13}C=O$ group in an amino acid residue within a peptide was detected by SFG. This work will greatly enhance SFG's capability for site-specific orientation determination and will be a powerful tool in studying the local environment of small peptides as well as large proteins at interfaces. This work has been published as: Ding, B.; Laaser, J. E.; Liu, Y.; Wang, P.; Zanni, M. T.; Chen, Z. *The Journal of*

Physical Chemistry. B **2013**, *117*, 14625–34. Z.M.T. ,C.Z and B.D. designed the project. B.D. carried out the experiment. L. J. E. and B. D performed data analysis. W. P and L. Y. participated in the sample preparation.

5.1. Introduction

Isotope labeling and vibrational spectroscopy provides site-specific structural information on polypeptides and proteins.[1,2] Of the intrinsic vibrations inherent to proteins, the amide I band (mainly contributed by the backbone C=O stretching mode) is most often utilized in structural studies because its frequency and line shape are characteristic of the secondary structures and solvent environments of the backbone. Residue specific structural and environmental information can be obtained using isotope labeling. Labeling the backbone carbonyl with ^{13}C, the amide I band is shifted by ~40 cm^{-1}. A shift of ~66 cm^{-1} can be achieved with $^{13}C=^{18}O$ labeling. [1,3] Isotope labeling has been used in conjunction with 1D (FTIR) and 2D IR studies to obtain residue-by-residue backbone structural information about soluble proteins,[4-6] protein/peptide folding kinetics,[7-9] and amyloid aggregation and structure,[10, 11] to name only a few studies.

Isotope labeling and vibrational spectroscopy are particularly valuable for studies of membrane proteins since they do not easily crystallize and are difficult to study with solution NMR. Solid-state NMR is a powerful technique but it is challenging to study membrane interactions of proteins and peptides in real time. The samples for solid state NMR studies are pre-mixed lipids and proteins/peptides and usually contain multiple layers of lipids, not a single lipid bilayer. Vibrational spectroscopy has been used to probe the structure of membrane bound alpha-helical bundles[12], ion channels[4], transmembrane alpha-helices [13-15] and helical dimers [5]. In fact, the polypeptide that is the focus of this study, ovispirin, was previously $^{13}C^{18}O$ labeled for

2D IR experiments on its membrane bound structure. In that experiment, residue-by-residue structural resolution revealed the backbone orientation, tilt and secondary structure of each residue along nearly its entire length. [3] Another approach is to measure the angles of individual transition dipoles relative to the normal of the bilayer, which is done by macroscopically aligning the bilayers on an FTIR sample cell. Polarized light is then used to measure the linear dichroism of the isotope labels to back out the absolute angles. By isotope labeling a series of amino acids, this approach was used to obtain the structure of the CD3-ζ helical bundle [12] and to study the conformation gating of the M2 ion channel from the Influenza viral protein.[4]

While orientational constraints derived from FTIR spectroscopy are very valuable, as solid state NMR, FTIR dichroism studies cannot be performed on single monolayers because the signal is too small to deduce accurate angles. For adequate signal strength, hundreds or thousands of bilayers are stacked on top of one another. Lipid bilayer stacking works well for equilibrated structures, but precludes experiments involving kinetics, drug binding, applied potentials, or systems that cannot be stacked such as solid interfaces. Moreover, since linear dichroism is attenuated by disorder, x-ray-reflectivity must be used to independently assess the disorder of the lipid stacks.[16] Thus, it would be quite beneficial to have a technique that is sensitive enough to measure the transition dipole angles of isotope labeled peptides associated with a single monolayer.

In contrast to FTIR, sum-frequency generation (SFG) vibrational spectroscopy has the sensitivity to observe peptides at sub-monolayer surface coverages, which has been discussed in the previous chapters. Since 2003, SFG has been successfully used to study biological molecules with various secondary structures and on different types of surfaces, including α-helices[17-20], 3_{10} helices,[21, 22] anti-parallel β-sheets[23,24] and extended β sheets [25,26]. However, there are often many

approximations that go into the interpretation of the SFG spectra of a peptide. For example, to back out the tilt of an alpha-helix at an interface, one often assumes that the peptide has a rotational freedom about its helical axis.[17-20] This is possible for peptides which insert perpendicularly into a cell membrane because the interior of the membrane lipid bilayer is quite homogeneous (hydrophobic), but this is certainly unlikely for amphipathic and many other types of peptides at a hydrophobic substrate/aqueous solution interface. This assumption is required because there are not enough SFG observables to obtain unique tilt and internal rotation angles of the peptides. Other assumptions are also common, such as that random coil regions generate weak SFG signals or have different peak centers in SFG spectra and that the vibrational modes follow symmetry rules.[17-20] In this chapter, we show that a single residue can be resolved using ^{13}C isotope labeling in the 18-residue antibiotic ovispirin at a polystyrene/peptide solution interface. The additional observables that this label provides eliminate the need for rotational averaging. We also learn that coupling to the isotope label may need to be considered. Previously, SFG spectroscopy was used in conjunction with NMR spectroscopy to provide a structural model of the synthetic LKα14 peptide, by measuring isotope labeled side chains. [27, 28] Here, we demonstrate for the first time that SFG spectroscopy can also be used to site-selectively probe the backbone carbonyl groups themselves, thereby providing a more direct measure of peptide secondary structure.

Ovispirin-1 is an ideal target for our initial SFG experiments because its structure has been studied extensively in solution and on model phospholipid membranes. Solution NMR experiments showed that in 33% 2,2,2-trifluoroethanol (TFE)/67% PBS buffer at pH 6.5 ovispirin-1 forms a slightly curved α-helix over residues 4 to 16, with random coil outside of this region.[29] Solid-state NMR experiments showed that on membrane bilayers, ovispirin-1 is still

predominantly α-helical, but lies primarily in the plane of the bilayer, with the helix tilted approximately 84° from the surface normal [30]. Two-dimensional infrared spectroscopy (2DIR) and molecular dynamics (MD) simulations similarly support the α-helical structure and planar orientation, and additionally showed that its hydrophobic residues face into the membrane interior, consistent with its amphipathic sequence [3].

However, it is unknown what structure ovispirin-1 will take or how it will interact with a purely hydrophobic surface such as the polystyrene surface we utilize here. As mentioned above, in 33% TFE/67% PBS buffer at pH 6.5 ovispirin-1 forms an α-helix over residues 4 to 16 [29]. Similarly, our choice of solvent (40% TFE and 60% 10 mM PBS buffer of pH=7.1) should promote helix formation similar to the solution structure (which will be confirmed later), but the tilt angle relative to the substrate surface may be considerably different than in the membrane bilayer systems, and interaction with the highly hydrophobic surface may perturb the overall peptide secondary structure. In this research, we find that the peptide backbone is tilted 138° with respect to the surface normal and the hydrophobic residues face polystyrene. Thus, the combination of isotope labeling and SFG spectroscopy brings new light to this system and enables many new systems to be studied that were not previously possible.

5.2 Experimental Details

5.2.1 Materials and Methods

SFG theory and experimental details have been reported previously[31-35] and discussed in the previous chapters. SFG has been applied to study peptides and proteins at interfaces by several research groups.[36-39] In our experiment, two laser beams, one visible beam at 532 nm and

an infrared beam with tunable frequency (1300 to 4300 cm^{-1}) are overlapped spatially and temporally at the bottom of a right-angled prism.[40] The polystyrene (PS) thin film on the prism surface was prepared by spin coating 1 wt% PS solution in toluene on the CaF_2 prism surface at 2500 rpm with a spin coater from Specialty coating systems. During every SFG experiment, the PS film was initially in contact with a 2 mL reservoir filled with 40% TFE and 60% 10 mM phosphate buffer (pH=7.1) in H_2O or D_2O. Then 20 μL ovispirin-1 peptide stock solution (1mg/mL in the same solvent) was injected into the 2 mL reservoir. The final subphase peptide solution concentration in the reservoir was 10 μg/mL and the equilibration time for the peptide-PS interaction was about 1.5 hrs. In order to ensure the homogeneously distributed peptides in the subphase in contact with PS, a magnetic stirrer was used during the data collection process. SFG ssp (s-SFG, s-IR, p-visible) and ppp spectra in the amide I frequency range were collected from ovispirin-1 peptide molecules at the PS/subphase peptide solution interface using a near total reflection geometry.[23] Regular ovispirin-1 (with the sequence of KNLRRIIRKIIHIIKKYG) and isotope labeled ovispirin-1 (with the α-carbonyl group of residue 11 Ile being isotope labeled into $^{13}C=^{16}O$) were synthesized by Peptide 2.0 Inc. PS, toluene, TFE, PBS, D_2O were obtained from Sigma-Aldrich.

A Nicolet 550 spectrometer (Thermo Fisher Scientific. Inc., MA) was used to collect ATR-FTIR spectra of isotope-labeled and regular ovispirin-1 adsorbed on PS surfaces. A thin PS polymer was deposited on the ZnSe crystal surface by casting 1 wt% polymer solution in toluene and then drying it under a nitrogen gas flow. 160 μL 1 mg/mL ovispirin-1 peptide solution in D_2O was injected into the ATR-FTIR trough (~1.6 mL) and the final concentration of the ovispirin-1 peptide solution is ~100 μg/mL (ten times larger than that used in the SFG experiment). The spectra with P and S polarizations were collected at ~2 hrs after the injection of

the peptide stock solution to the ATR-FTIR trough. The ATR-FTIR sample chamber was purged with nitrogen before and through the measurements.

SFG spectra were simulated using the transition dipole coupling model and an excitonic Hamiltonian, as described in Section 5.2.2. Briefly, peptide or ideal helix structures were loaded from a protein databank file. A transition dipole and Raman polarizability were assigned to each amide I local mode. Transition dipole coupling was used to calculate couplings between all pairs of local amide I modes. The resulting Hamiltonian was diagonalized to yield the eigenstates of the system[41], whose coefficients were used to calculate the normal modes by taking appropriate linear combinations of the local mode of the transition dipoles and Raman polarizabilities. These responses were rotated to the laboratory frame, and summed to give overall SFG intensities for the labeled and unlabelled peaks.[42]

5.2.2 Calculation Details of Hamiltonian approach

5.2.2.1 Definition of the Molecular Response for a Single Amide-I unit

The molecular axes for an individual amide-I unit are defined such that the C(O)N bond lies in the bc-plane (molecular yz plane), with the CO bond tilted 34 degrees from the c axis, as shown in Fig. 5.1.

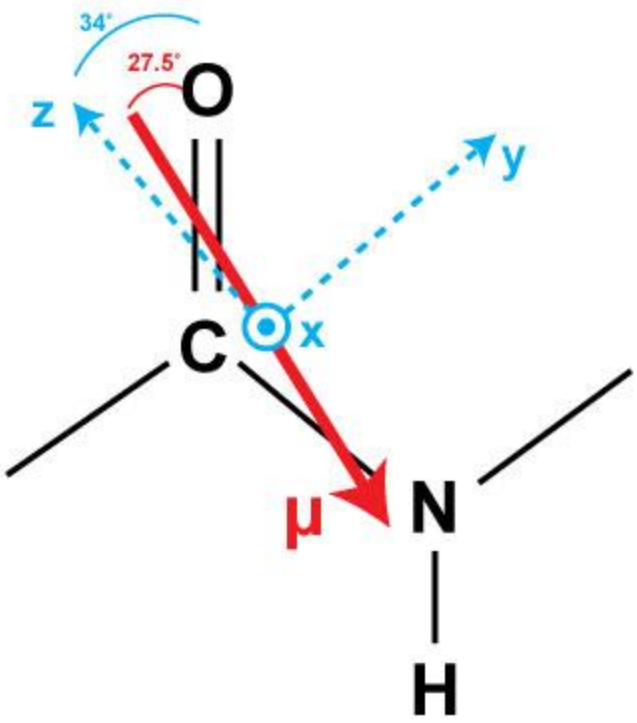

Figure 5.1 Diagram illustrating the orientation of the molecular response with respect to the amide-I bond. The red arrow indicates the direction and effective location of the transition dipole; the blue axes indicate the principle axes of the Raman polarizability.

In this frame, the transition dipole is defined as

$$\mu = \begin{pmatrix} 0 \\ -\sin\frac{6.5\pi}{180} \\ -\cos\frac{6.5\pi}{180} \end{pmatrix}$$

such that it is oriented 27.5 degrees from the CO bond. This angle was chosen to ensure that the angle of a single amide-I transition dipole relative to the axis of an ideal alpha helix was 42 degrees (see below), consistent with prior calculations.

The molecular-frame transition polarizability is defined as

$$\alpha = \begin{pmatrix} 0.25 & 0 & 0 \\ 0 & 1 & 0 \\ 0 & 0 & 5 \end{pmatrix}$$

as reported[19]. Thus the chromophore is most polarizable along the molecular c-axis, 34 degrees from the CO bond, and least polarizable along the molecular a-axis, out of the plane of the C(O)N bond.

The "center", or effective position, of the vibrational mode is defined to be

$$\vec{r}_{amide-I} = \vec{r}_C + 0.665\hat{r}_{CO} + 0.256\hat{r}_{CN}$$

where $\vec{r}_C$ is the position of the carbon atom, $\hat{r}_{CO}$ is the unit vector along the CO bond, and $\hat{r}_{CN}$ is the unit vector along the CN bond, with all positions given in Angstroms[41]. This position is used to calculate the distance between coupled modes, as necessary for the transition dipole coupling calculations as described below.

5.2.2.2 Transition Dipole Coupling and Normal Mode Calculations

For each C(O)N bond in the peptide structure, the single-residue response defined above was rotated and translated into the helix (or peptide) molecular frame, as described previously[42]. For the ideal helix structure, with the helix axis oriented along the z-axis and the transition dipole of the first mode lying in the xz plane, the single-residue response in the helix frame is

$$\mu = \begin{pmatrix} 0.67 \\ 0 \\ 0.74 \end{pmatrix}$$

corresponding to a transition dipole tilted 42 degrees from the helix axis, and

$$\alpha = \begin{pmatrix} 0.64 & 0.03 & 0.40 \\ 0.03 & 0.06 & -0.01 \\ .40 & -0.01 & 0.55 \end{pmatrix}$$

which corresponds closely to previous reports[19].

Once each local mode was rotated into the peptide frame, their couplings were calculated using the transition dipole coupling model,

$$\beta_{ij} = \frac{1}{4\pi\epsilon_0}\left[\frac{\vec{\mu}_i \cdot \vec{\mu}_j}{r_{ij}^3} - 3\frac{(\vec{r}_{ij} \cdot \vec{\mu}_i)(\vec{r}_{ij} \cdot \vec{\mu}_j)}{r_{ij}^5}\right]$$

where β_{ij} is the coupling between modes i and j, the $\vec{\mu}$'s are the transition dipoles of the two modes, and $\vec{r}_{ij}$ is the vector connecting the center positions of the two modes. Coupling values for $|i - j| = 1$ were multiplied by a factor of 0.73 to give better agreement with typical coupling constants for alpha helices[41].

The Hamiltonian was then constructed in the local mode system, using the calculated couplings for the off-diagonal elements and the local mode frequencies for the on-diagonal elements. We used a local mode frequency of 1645 cm^{-1} for unlabeled ($^{12}C=^{16}O$). For the labeled mode, we used a frequency of 1600 cm^{-1}. This frequency is slightly lower than the 1608 cm^{-1} frequency observed in the experimental spectra, but the larger frequency separation was necessary to easily distinguish the labeled peak from the unlabeled peak in the ensuing calculations, and did not seem to significantly affect our analysis.

The Hamiltonian was diagonalized, and the normal mode transition dipoles were calculated using

$$\mu_N = \sum_m C_{Nm}\mu_m$$

where $\mu_m$is the local mode transition dipole, μ_N is the normal mode transition dipole, and C_{Nm} is the element of the eigenvector giving the contribution of local mode m to normal mode N. The normal mode Raman tensors were calculated using an analogous formula (replace μ with α). The normal mode hyperpolarizabilities β were then calculated by taking the outer product of μ and α:

$$\beta = \alpha \otimes \mu$$

The normal mode hyperpolarizabilities were then rotated into the lab frame to calculate the lab-frame responses χ, as has been described previously[42].

To calculate simulated spectra, we summed a series of Lorentzians centered at the normal mode frequencies and multiplied by the mode's χ value. To calculate the total χ value for the labeled peak, we summed over all normal modes with frequencies less than 1610 cm^{-1}. The unlabeled peak χ values were correspondingly determined by summing over all normal modes with frequencies >= 1610 cm^{-1}. A more accurate method would be to fit the simulated spectra to a pair of peaks, but applying a simple cutoff was computationally much faster and did not yield significantly different results.

5.3 Results

In what follows, we will begin by presenting the experimental data. The data will then be interpreted with detailed orientation analyses. First, we will use conventional formulas to determine the tilt of the alpha-helix from the SFG polarization dependence of the unlabeled spectral region of the amide I band, assuming that the helix is isotropic (with a free rotation with the helix principal axis). Second, a similar analysis will be applied to the isotope labeled region. But as we will show, these two analyses are incongruent. To understand this dilemma, our third analysis will use the ratio of the unlabeled to labeled amide I bands which provides an additional observable that improves the structural analysis, suggesting that the peptide has a preferred orientation on the surface without free rotation. Finally, we will highlight that the Hamiltonian approach can address the coupling effect and structural disorder issues.

5.3.1 Experimental Spectra

SFG spectra in the amide I frequency range (1500-1800 cm^{-1}) were collected from both isotope labeled and unlabeled ovispirin-1 adsorbed at the PS/peptide solution interface. (Figure 5.2) A strong peak at ~1650 cm^{-1} was detected from both systems at the interface when a peptide H_2O/TFE buffer solution was used to contact PS. With a peptide D_2O/TFE buffer solution for a separate experiment, the amide I band appears at 1642 cm^{-1}, with a similar intensity. The 8 cm^{-1} difference is typical for an amide I band detected from proteins/peptides in H_2O and in D_2O [43, 44] because the amide I vibrational mode involves the N-H stretch to a small degree. Although SFG signal in this spectral frequency range overlaps with that contributed by the vibrational mode of random coils, we believe here random coils have little contribution to the SFG signal because 1) SFG signal requires the ordering of the chemical groups and thus the amide I signals from the random coils likely cancel with each other. In other words, SFG spectroscopy is much more sensitive to α-helices than random coils.[45] In fact, to the best of our knowledge, amide I signal from a peptide with random coiled structure on the surface has not been observed by SFG spectroscopy. 2) In both H_2O and D_2O cases, the main amide I peak has a symmetric feature with a similar bandwidth. If the 1650 cm^{-1} peak in the H_2O case contained two different components with comparable SFG signal intensity contributed from the α-helical structure and the random coiled structure, the deuteration of the peptide solvent would lead to a different spectral feature for the 1642 cm^{-1} peak,[44] which was not observed experimentally here. 3) We used NLOPredict[46] developed by Simpson group to estimate the contribution of the α-helical structure and the random coiled structure to the SFG amide I signal and found that the contribution of the random coiled structure is minimal for two typical orientations and thus can be ignored in the analysis. For the isotope labeling case in H_2O, a well-separated and weak peak at ~1607 cm^{-1} was also

detected, which is the Ile11 isotope labeled amide I band (Figure 5.2b). Interestingly, the peak center of the isotope labeled C=O appears at ~1607 cm^{-1}, appearing to be a shoulder to the 1642 cm^{-1} amide I main peak when D_2O was used in the solvent (Figure 5.2d). Previous research on a helical dimer showed that ^{13}C=O Leu in a solvent protected region exhibited a peak at ~1606 cm^{-1} whereas the ^{13}C=O of a solvent exposed Ala absorbed at ~1585 cm^{-1}. [47] For ovispirin-1 on polystyrene, we found that the ^{13}C=O of Ile11 remains at ~1607 cm^{-1} regardless of solvent. Thus, Ile11 is not exposed to the solvent, which we will discuss below is because this residue faces the polystyrene surface.

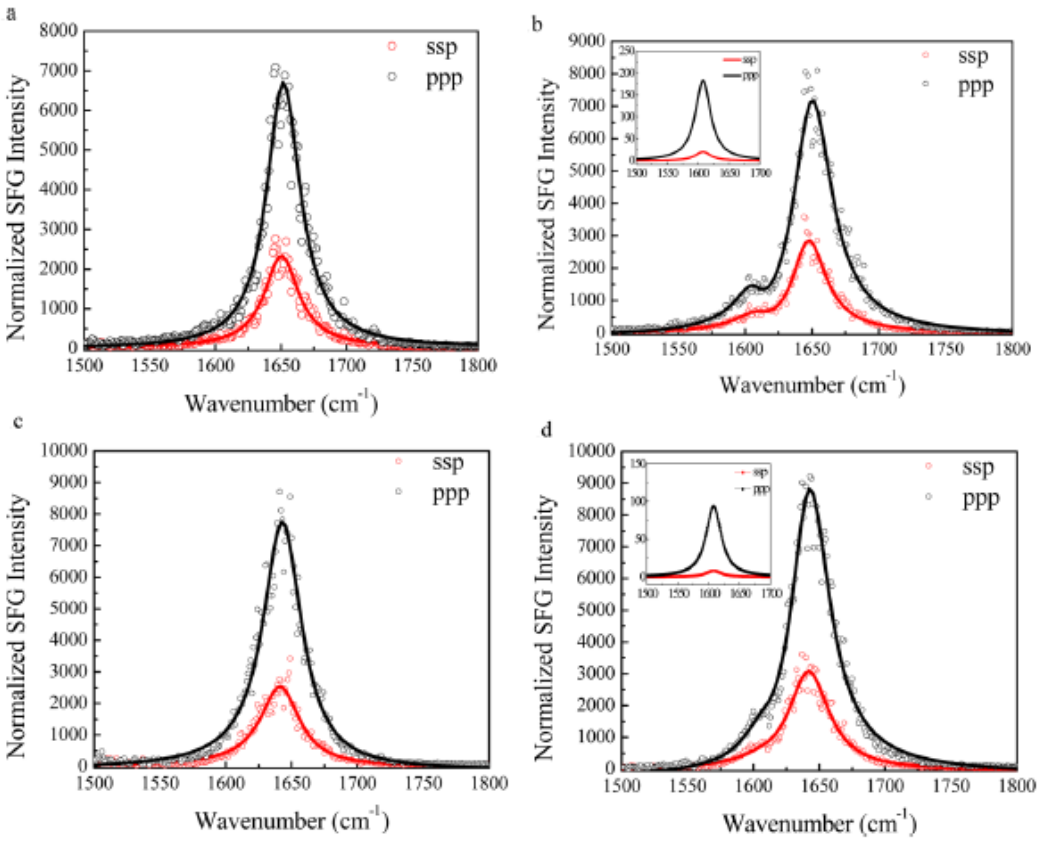

Figure 5.2 The ssp and ppp SFG amide I spectra of (a) regular ovispirin-1 adsorbed at the PS/peptide solution (with H_2O) interface; (b) isotope labeled ovispirin-1 adsorbed at the PS/peptide solution (with H_2O) interface; (c) regular ovispirin-1 adsorbed at the PS/peptide solution (with D_2O) interface; (d) isotope labeled ovispirin-1 adsorbed at the PS/peptide solution (with D_2O) interface.

We fit the SFG spectra shown in Figure 5.2 to extract out the intensities of the isotope labeled peak, since there exist interferences with the unlabeled amide I band. The experimentally deduced χ_{zzz}/χ_{xxz} is 2.03±0.03 for the 1650 cm^{-1} band in H_2O for the regular ovispirin-1. For the isotope labeling case, we fit the spectra considering two peaks with peak centers at 1650 cm^{-1} and 1607 cm^{-1}, respectively. The fitting result of the 1650 cm^{-1} peak shows a χ_{zzz}/χ_{xxz} ratio of 1.95±0.09. For the 1607 cm^{-1} peak, we obtained an experimentally measured χ_{zzz}/χ_{xxz} ratio of 3.7±0.2. The spectral fitting results obtained from peptides at the PS/peptide D_2O solution interface are similar to the H_2O cases (Table 5.1): 2.08±0.02 (regular) and 1.97±0.06 (isotope labeled) for the 1650 cm^{-1} signal; 4.1±0.1 for the 1607 cm^{-1} peak. To take both solvent cases into consideration, we averaged χ_{zzz}/χ_{xxz} ratios for the main backbone amide I peak of ovispirin-1 (2.00±0.10) and for the isotope labeled peak (3.85±0.35). Comparing the relative helix and labeled peak signal strength, we find that χ_{zzz} (helix)/χ_{zzz} (label) = 6.18.

	Amide I	Single residue
	χ_{zzz}/χ_{xxz}	χ_{zzz}/χ_{xxz}
C12 in H_2O	2.03±0.03	N/A
C12 in D_2O	2.08±0.02	N/A
C13 in H_2O	1.95±0.09	3.7±0.2
C13 in D_2O	1.97±0.06	4.1±0.1

Table 5.1 Fitting results for SFG spectra shown in Figure 5.2

5.3.2 Orientational Analysis of the Helix

Having acquired the data above, the standard approach (see Chapter 1) is to interpret the χ_{zzz}/χ_{xxz} ratio as a measure of the tilt angle of the helix at the surface. For an ideal helix, the transition dipole of each amide I local mode points 42 degrees from the helix axis, there is a 100 degree rotation about this axis from one reside to the next, and each local mode has a Raman tensor associated with it. [19]. Using this ideal structure, one generates the normal modes of the helix by diagonalizing a vibrational Hamiltonian built from the local modes of the coupled amide I oscillators. The χ_{zzz}/χ_{xxz} ratio is then calculated from the transition dipoles of the normal modes as a function of the tilt (θ) and twist (ψ) angles (defined in Figure 5.3). Doing so for a 13-residue ideal helix produces the χ_{zzz}/χ_{xxz} ratio shown in Figure 5.3(a) when ψ is rotationally averaged around the helix axis. Rotationally averaging around ψ is necessary because there is only one experimental observable (the χ_{zzz}/χ_{xxz} ratio), but two unknowns (θ and ψ). For a perfect and infinitely long helix, one obtains the same θ-dependence whether or not ψ is averaged. For a real helix longer than a few turns one can in practice treat the structure as fully symmetric around the helix axis. Here we chose 13 residues for the helix because that is the length of the ovispirin-1 alpha-helix in solution. As discussed above, we believe that the peptide retains its α-helical structure at the polymer/solution interface because the SFG spectra are dominated by a single α-helical characteristic peak at ~1650 cm^{-1}. This can be further confirmed by the intensity ratio of the main peak and the signal detected from the isotope labeled unit, which will be discussed in detail in section 5.4. With these considerations in mind, the experimental ratio of χ_{zzz}/χ_{xxz} = 2.00 gives a helix tilt angle of θ =43 (or 137) +/- 5 degrees relative to the polystyrene surface normal.

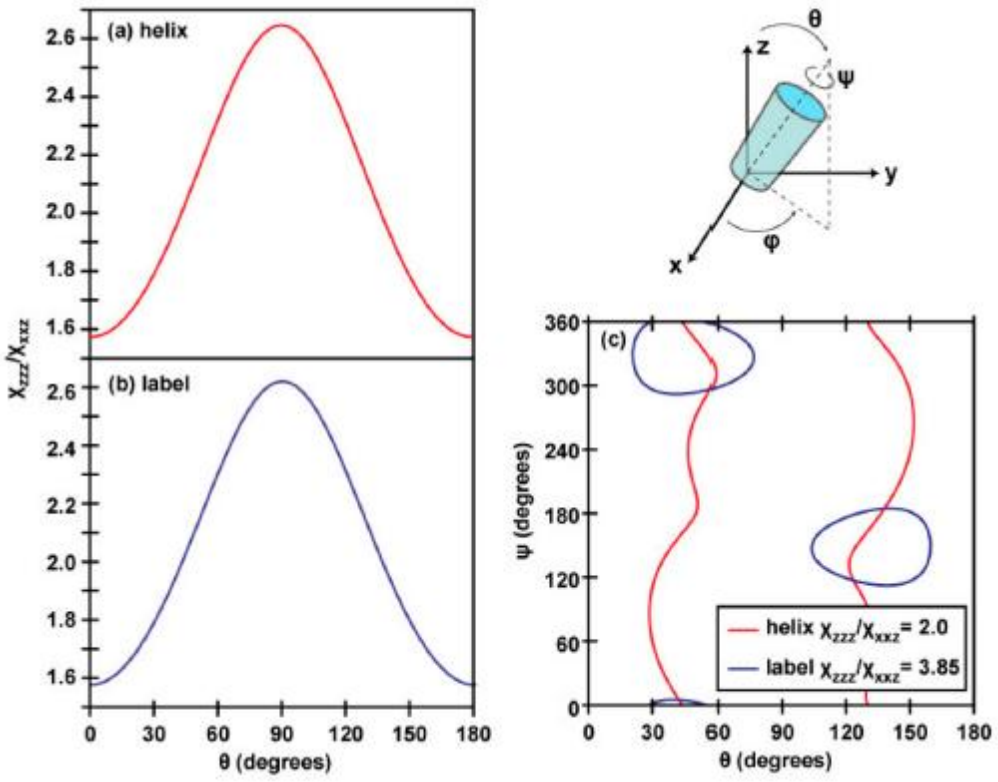

Figure 5.3 χ_{zzz}/χ_{xxz} ratios for (a) the unlabeled segment of an ideal alpha helix and (b) the isotope labeled peak, assuming full rotational averaging around the helix axis. (c) Contours indicating ψ/θ pairs giving the experimentally-measured values for the unlabeled and labeled peak χzzz/χxxz ratios. In this figure, the tilt angle θ indicates the angle between the helix axis and the surface normal.

5.3.3 Orientational Analysis of the Isotope Label

One could apply a similar analysis to that above for just the independent isotope label. In this case, the analysis is much simpler, because one does not need to construct or diagonalize a Hamiltonian. One would use the same transition dipole and Raman polarizability tensors as above to calculate the tilt-angle dependence of the χ_{zzz}/χ_{xxz} ratio for a single amide-I residue, as shown in Figure 5.3(a). Here, we have defined θ_{label} as the angle between the transition dipole and the surface normal and we rotationally average around the label transition dipole, ψ_{label}. Note,

that averaging around ψ_{label} is not equivalent to averaging around ψ for the helix or around the labeled C=O bond because the rotation axis is different. The tilt-angle dependence for both the ψ-averaged and the individual ψ_{label}=0 and ψ_{label}=90 deg. cases are very similar, because the Raman tensor's major axis points almost directly along the transition dipole with much smaller (though unequal) components along the perpendicular axes (see Section 5.2). The consequence is that there is a maximum of about 10 degrees difference in tilt angles calculated from ψ-fixed or ψ-averaged curves. Thus, while ψ averaging is necessary to eliminate an unknown variable just as for the helix analysis, it does not influence the θ_{label} more than a few degrees. Using this curve and the experimentally-measured χ_{zzz}/χ_{xxz} ratio of 3.85 +/- 0.35 for the isotope-labeled peak, we find θ_{label} = 26 or 154 degrees from the surface normal. In order to do this analysis, we have to use the ψ average because otherwise there are too many unknowns. However, that approximation is not physically reasonable because rotating around the label's axis swings the entire peptide structure, since ψ_{helix} is not equal to ψ_{label}. Taking the internal rotational average about ψ_{helix} for the unlabeled band (as done in the last section) makes sense if the helix is long and perfect, because ψ averaging is equivalent to the symmetry modes. Thus, the analysis of a single label by itself makes no physical sense, and what needs to be done is to solve for tilt and twist angles that simultaneously give the correct ratios for the both the labeled and unlabeled peaks.

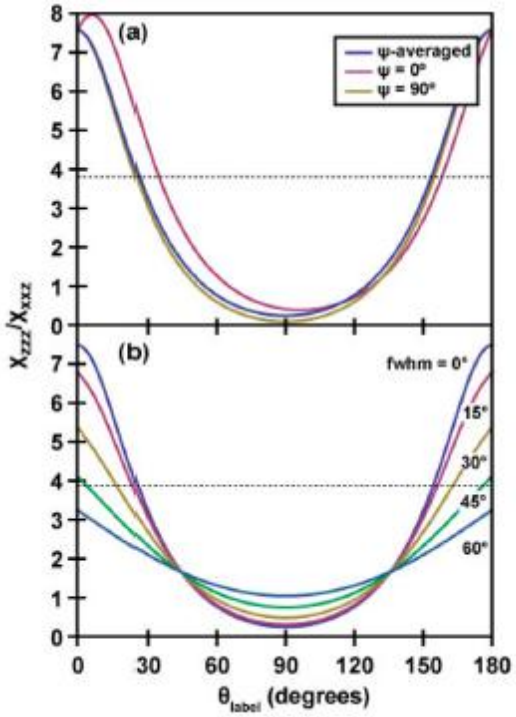

Figure 5.4 Tilt-angle dependence of the χ_{zzz}/χ_{xxz} ratio for a single amide-I residue, for (a) the ψ-averaged case and two fixed-ψ cases (ψ=0 corresponds to the C(O)N bond lying in the yz plane) and (b) the ψ-averaged case for Gaussian distributions of tilt angles with different full-width-at-half-maxima (indicated). In (a) and (b), the tilt angle θ is defined as the angle between the transition dipole and the surface normal.

While ψ averaging an unlabeled helix is acceptable because of the symmetry, including the isotope label destroys the rotational symmetry, and the rotational average is no longer a valid approximation. This can be shown by calculating the χ_{zzz}/χ_{xxz} ratio for the label predicted by a fully internally rotationally-averaged helix. When applied to the label, the orientational analysis above predicts that the χ_{zzz}/χ_{xxz} ratio of the label should match that of the unlabeled amide I band (Figure 5.3b), because symmetry dictates that in helical molecules the responses of the parallel and perpendicular normal modes (A and E1 modes) are closely related to the parallel and perpendicular components of a single local mode's response. [52, 53] Thus, for a ψ-averaged helix tilted at 43 (or 137) degrees from the surface normal, one would also predict that a χ_{zzz}/χ_{xxz} ratio

of 2.00 would be measured for the label. But the experimentally-measured ratio is actually 3.85, which far exceeds the experimental uncertainty. In fact, a χ_{zzz}/χ_{xxz} ratio of 3.85 cannot be matched by a rotationally averaged helix at any tilt angle. That is, the ratios of the unlabeled and labeled amide I bands are incongruous for an analysis that requires rotational averaging around the helix axis.

5.3.4 Orientational Analysis of the Entire Peptide including Structural Disorder and Coupling

How does one reconcile the ratios of the labeled and unlabeled amide I bands? We need to consider the possibility that the helix is not isotropic about ψ_{helix}. That is to say, the helix does not have a free rotation around the principal axis. In order to determine the orientation of such an α-helix, we need to determine both the tilt angle and the twist angle. We retain a perfect helix with the label uncoupled from the rest of the helix and simultaneously calculate the χ_{zzz}/χ_{xxz} ratios for both the labeled and unlabeled peaks as a function of tilt and twist angles. Using the two measured χ_{zzz}/χ_{xxz} ratios for the labeled and unlabeled peaks, we can deduce two unknowns: the tilt angle and the twist angle. As shown in Figure 5.5(c), we find that our measured χ_{zzz}/χ_{xxz} ratios are consistent with helix tilt/twist angles of (θ, ψ) = (41°, 5°), (57°, 297°), (123°, 117°), or (138°, 184°). Homodyne-detected SFG cannot distinguish between the 90+x and 90-x degree tilt angles[27], though future phase-sensitive or heterodyne-detected experiments may resolve this difficulty [48-51]. However, we can narrow the possibilities using physical intuition and the experimentally observed solvent accessibility of Ile11. Before rotation, our ideal helix is defined such that the hydrophilic region extends from -60 to +120 degrees around the helix axis. Thus the (41°, 5°) orientation corresponds predominantly to having the hydrophilic region of the

peptide facing the polystyrene surface, while the (138°, 184°) orientation corresponds to having the hydrophobic region of the peptide facing the polystyrene surface; in the remaining two orientations, the hydrophobic and hydrophilic regions have roughly the same extent of interaction with the surface. Of these tilt-angle possibilities, the (138°, 184°) pair is most physically reasonable, since the solvent dependence of the peak center of the labeled unit indicates that the residue is buried at the hydrophobic interface and the interaction of the hydrophobic side of the peptide with the hydrophobic polystyrene surface should inherently be more favorable than the interaction of the hydrophilic side of the peptide with this surface. The following reasons further support that the (138°, 184°) orientation is the most likely orientation (Figure 5.5): First, this helix orientation also gives a χ_{zzz} (helix)/χ_{zzz} (label) ratio of approximately 6.2, consistent with our experimental value of 6.18, a criterion which is not met by the (57°, 297°) and (123°, 117°) orientations (which both yield χ_{zzz} (helix)/χ_{zzz} (label) ratios of less than 5). Second, at this orientation, the transition dipole of the isotope labeled unit is calculated to be tilted 23 degrees relative to the surface normal, in good agreement with the value calculated from our preceding analysis of the isolated label. To further clarify the final orientation of (138°, 184°), we also present the reference peptide orientation (0°, 0°) along with the final orientation in Figure 5.5.

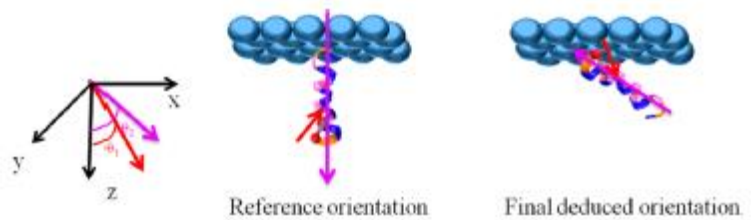

Figure 5.5 Schematic (right panel) showing the final deduced orientation of ovispirin (tilt angle = 138°, twist angle = 184°) at the polystyrene/water interface. Left panel defines the reference orientation (tilt angle = 0°, twist angle = 0°) where the hydrophilic region (blue) extends from -60 to +120 degrees around the helix axis. θ_1 is the angle between the

transition dipole of $^{13}C=O$ chemical group (purple arrow) and the z axis and θ_2 is the angle between the peptide helix axis (from N to C terminus) (red arrow) and the z axis. For the reference orientation, $\theta_1=138^\circ$ and $\theta_2=0^\circ$ and for the final deduced orientation, $\theta_1=23^\circ$ and $\theta_2=138^\circ$

Thus, analyzing the labeled and unlabeled peaks within the framework of an ideal helix provides insight into the overall orientation of the ovispirin peptide at the solution/polystyrene interface. However, perhaps analyzing the angles alone is not sufficient, because ovispirin is far from an ideal helix at the interface, which we learn from the observations listed below and leads to additional considerations about the interpretation of the spectra. First, comparing the intensities of the labeled and unlabeled amide I bands reveals that only a subset of the residues can contribute to the helical structure. For the (138°, 184°) tilt/twist angles calculated above, in which the angular dependence of the labeled and unlabeled peaks were considered independently, a full 18- residue helix would give a χ_{zzz}(helix)/χ_{zzz}(label) value of 7.0, which deviates by almost 15% from the experimental value of 6.18. Reducing the length of the helical section to anywhere between 13 to 15 residues gives the χ_{zzz}(helix)/χ_{zzz}(label) value between 6.1 and 6.3. Further reducing the length of the helical section causes the χ_{zzz}(helix)/χ_{zzz}(label) ratio to drop far below the experimentally measured value. While this result is consistent with the 13-residue helix analyzed above, it reveals that the entire 18-residue ovispirin peptide cannot form a perfectly ordered helix, because if it did, then the intensity of the isotope label would be much smaller as compared to the unlabeled amide I band (Intensity is proportional to the square of the χ value).

We want to highlight here that the Hamiltonian approach we present in this chapter can be used to calculate the coupling between the label and the rest of the peptide, including these couplings in the Hamiltonian disrupts the transition dipoles of the helix, which changes the strength of many of the SFG-active normal modes. Shown in Figure 5.6(a, b) are spectra for a

13-residue labeled helix at the (138 °, 184 °) tilt/twist angle. Figure 5.6(a) shows the response of an isolated label added to that of an un-disrupted helix, while Figure 5.6(b) shows the spectrum when the isotope label is incorporated into and coupled with the rest of the helix. The stick spectrum shows significant contributions from new SFG-active modes, indicating that the label and the helix cannot be treated as independent vibrational modes. In this regard, $^{13}C=^{18}O$ isotope labeling is preferable, because the labeled amide group has better decoupling, although both $^{13}C=^{16}O$ and $^{13}C=^{18}O$ labels will affect the unlabeled spectrum about the same amount. This effect will be important when the isotope labeled unit is incorporated into different sites of the peptide or more than one isotope labeled units are incorporated.

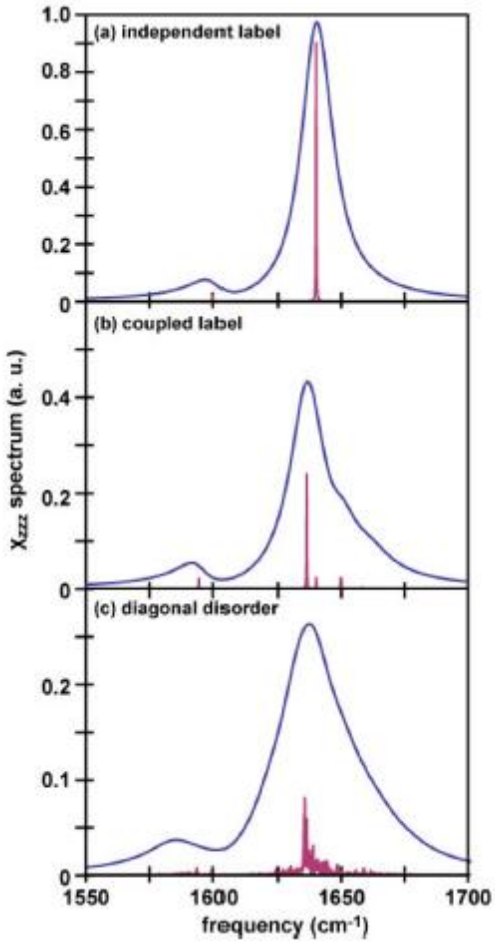

Figure 5.6 Simulated spectra showing (a) a 13-residue ideal helix, with the isotope label calculated independently of (or uncoupled from) the rest of the helix, (b) a 13-residue ideal helix with the isotope label incorporated into and coupled with the other residues in the helix, and (c) a 13-residue ideal helix summed over 50 spectra with 16 cm^{-1} random disorder in the local mode frequencies. Spectra were simulated using a 15 cm^{-1} Lorentzian for each mode. Stick spectra (purple) are also included to emphasize how the normal mode structure changes as the couplings are broken.

Second, the Hamiltonian approach can be used to access the effect of the structural disorder. Random disorder along the diagonal of the Hamiltonian occurs in many systems where the individual chromophores have different local mode frequencies due to different local environments in different molecules, for example if the local solvation environment of the amide-I modes varies from amide to amide bond [54, 55]. In Figure 5.6(c), we show the spectrum expected for a 13-residue labeled helix with 16 cm^{-1} standard deviation random variation in the local mode frequencies added before diagonalizing the Hamiltonian, averaged over 50 different disordered Hamiltonians. 16 cm^{-1} is about the disorder one expects due to differences in hydrogen bonding for soluble polypeptides. We see that the SFG spectrum of the disordered helix is broader and less intense than that of the ordered helix, because all different members of the ensemble now have slightly different normal modes. The overall calculated tilt angle from the labeled and unlabeled peaks does not change significantly with this added disorder, but the helix/label ratio increases. Thus, disorder that is created by the typical environment surrounding a polypeptide does not change the interpretation of the angular measurements, but does alter the relative intensities of the labeled and unlabeled amide I modes. However, the spectrum shown in Figure 5.6 (c) is not very similar to the spectra we observed in Figure 5.2. Therefore in this study, we believe that the effect of the structural disorder is not substantial. At this stage, we cannot quantify this effect in our current measurements because it requires dynamic knowledge of the linewidths, which will be the subject of future work. Nonetheless, the point being made is that

disorder breaks the symmetry of the helix, and so in real systems one can no longer think of the normal modes purely as the fully symmetric A and E1 modes.

Interestingly, the tilt angles deduced in this work (138 degrees) indicate that the ovispirin is much more steeply angled away from the plane of the polystyrene surface than it is when adsorbed to a planar lipid bilayer. Using multiple label sites in future experiments will provide residue-by-residue structural information that can be used to obtain a complete backbone structure through constrained molecular dynamics simulations, as has been done with oriented polypeptides and FTIR spectroscopy.[56]

Last but not least, we want to mention a few other considerations that should be taken into account in future simulations. As revealed by previous NMR, 2D IR, and MD studies, ovispirin exhibits significant structural disorder as well. For example, in the solution NMR studies it is found that the helical portion of the peptide is somewhat curved, and the N- and C-terminal ends disordered. The curve breaks the symmetry of the helix and adds off-diagonal disorder to the Hamiltonian. The disordered ends will have both diagonal and off-diagonal disorder. Therefore such structures may contribute to SFG signals. In the future, we will calculate such contributions and validate the calculation method using multiple label sites in experiments. Also, we calculated the transition dipole and Raman response of a single amide-I mode using values derived from polarized FTIR and Raman experiments[23]. However, some models use slightly different molecular responses for a single amide-I mode [55,56], which will yield slightly different single-residue tilt angles. We have also assumed a delta-function orientational distribution. If the residues or peptides are instead distributed over a wider range of tilt angles, the tilt-angle dependence flattens out, as shown in Figure 5.4(b) for a series of Gaussian tilt-angle distributions of varying widths for a single vibrationally isolated label. This

flattening of the tilt-angle dependence means that the same experimental χ_{zzz}/χ_{xxz} ratio yields a center tilt angle closer to the surface normal as the distribution gets broader. Developments underway on modeling SFG spectra of peptides will help to better define these parameters. [57-59]

5.3.5 ATR-FTIR Experiments

For comparison purposes, we also performed ATR-FTIR experiments. The concentration of ovisiprin-1 is 10 times higher because no signal was detected from the isotope labeled group when lower peptide solution concentrations were used. The ATR-FTIR spectra collected from the PS/peptide solution interface are shown in Figure 5.7. We found that the PS polymer can generate a strong background ATR-FTIR signal at ~1602 cm^{-1} from one of the benzene ring modes[60], appearing as either a positive or negative peak. For both isotope labeled and regular ovispirin-1 samples, there is a broad peak at around ~1647 cm^{-1} (Figure 5.7), indicating the existence of both α-helical and random coil components. For isotope labeled sample, besides the negative peak at ~1602 cm^{-1}, an additional peak at ~1612 cm^{-1} can be assigned to the isotope-labeled C=O chemical group. Data analysis shows that this C=O is ~38 degree vs. the surface normal (Figure 5.7c) given that the dichroic ratio R of the isotope labeled C=O stretching peak is ~4.13.[61] Interestingly the 1602 cm^{-1} background signal of the PS polymer is silent in SFG spectra because this benzene ring mode is Raman inactive and thus SFG inactive. Besides, ATR-FTIR spectra have multiple contributions from the α-helix, the random coil and the polymer background which made the orientation determination of the single C=O chemical group by ATR-FTIR subject to large errors. Even so and even at a larger peptide concentration, the deduced orientation is not substantially different from the SFG result.

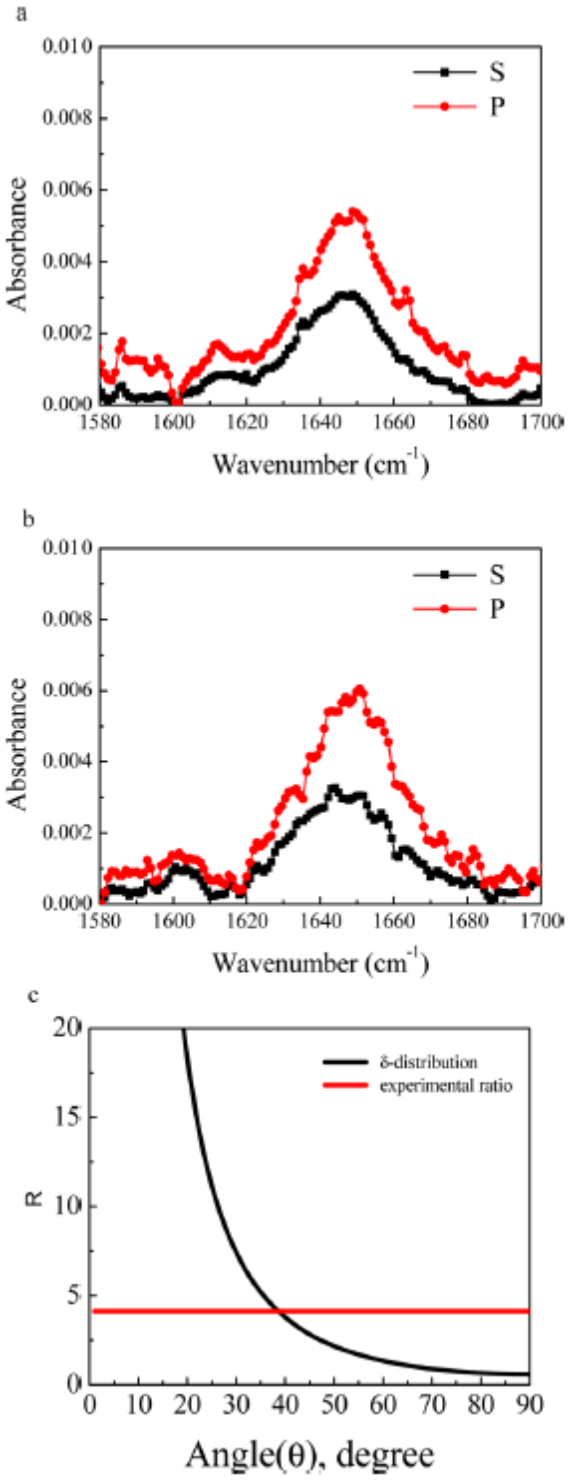

Figure 5.7 (A) ATR-FTIR spectra of isotope labeled ovispirin-1 molecules at the PS/peptide solution interface. (B) ATR-FTIR spectra of regular ovispirin-1 molecules at the PS/peptide solution interface. (C) The relationship between the dichroic ratio R of the isotope labeled C=O stretching peak and the tilt angle of the C=O bond direction relative to the surface

normal. The dichroic ratio R of the isotope labeled C=O stretching peak detected at the PS/peptide solution interface is shown as a horizontal line.

5.4. Discussion

Compared to ATR-FTIR, SFG studies on the C=O isotope labeled peptides have several advantages: 1) SFG spectra are free of background contribution from the polymer substrate as well as other media in our study. For peptides and proteins, SFG spectra have minimum contributions from random coils. Unlike in IR spectra, where H_2O absorption band overlaps with the peptide/protein amide I band, SFG spectra has minimum H_2O signal contribution and thus the experiment could be performed in H_2O and separate the signals from the isotope unit and the main amide I peak. 2) SFG is more sensitive than ATR-FTIR for detecting well-oriented α-helices, thus can detect signals from peptides from a single monolayer instead of bilayer stacks.

While solid-state NMR (e.g. PISEMA) is a well-established technique in obtaining orientation restraints for membrane bound peptides [62], isotope labeled SFG has some unique advantages: 1. SFG can monitor the interaction process *in situ* (~several minutes per spectrum) while NMR techniques such as PISEMA suffer from long-time data accumulation (~several hours per experiment), therefore the isotope labeled SFG technique can be used to monitor the dynamics of a single residue in biological processes such as ligand titration, fibril formation, GPCR-G protein interaction, ion channel opening and so on. 2. Only one bilayer is required, which allows very precise difference experiments, such as with ligand binding. 3. A typical solid-state NMR experiment on short peptides requires ~100 μg sample while an SFG experiment only needs ~10μg sample.

In this chapter we demonstrated the approach on a synthesized polypeptide that is isotope labeled using commercially available compounds. But the method is also applicable to proteins using exciting methods developed in the past few years. One set of approaches is native chemical ligation and expressed protein ligation.[63, 64] In these techniques, proteins are semi-synthesized from fragments using a thiol-ene chemistry. Thus, one can isotope label a fragment (e.g., a helix instead of a single peptide unit) in the same manner as we did here for ovispirin, and then ligate it to another fragment to form the full protein. Expressed protein ligation has recently been used in conjunction with 2D IR spectroscopy.[65] It is also possible to arbitrarily isotope label amino acids in proteins by using a cell free expression system and a stop codon that matches an isotope labeled t-RNA.[66] It is now also possible to put in non-natural isotope labels which might be SFG chromophores, such as nitriles, by using a tRNA synthetase pair system, like has been developed for phenylalanine.[67] With these new and exciting methods in hand, it is now possible to isotope label and thus monitor the structures of precise locations in nearly arbitrarily sized proteins. It is also important to point out that SFG spectroscopy requires a tiny amount of sample. For example, in the ovispirin-1 case, one SFG experiment only requires 20 μg sample. As a result, experiments are possible even on poorly expressing proteins or systems in which the ligation is inefficient. Furthermore, heterodyne detection can also improve signal-to-noise ratio, [46-49] and thus we believe that in the future, this technique will shed lights on larger protein systems.

5.5. Conclusion

We have shown that isotopic labeling enables SFG spectroscopy to detect polarized amide I signals from a single peptide unit in an α-helical peptide at buried polymer/solution interface. Such SFG signals can be used to study the microenvironment and interfacial orientation of the isotope labeled residue. If we assume a single distribution, the backbone helix

of ovispirin-1 on PS surface is 138 degrees relative to the surface normal with a twist angle of 184 degrees, and the transition dipole of the isotope labeled C=O group is tilted 23 degrees relative to the surface normal. Our result show that using the ^{13}C=O isotope labeling, SFG can be used to obtain residue-specific orientation information. In the future, using multiple label locations will allow us to measure the exact structure and orientation of surface-bound peptides without requiring assumptions about the expected secondary structure. This capability makes SFG a powerful technique for structural analysis and will bring new insight to many biophysical systems.

5.6. References

(1) Decatur, S. M. *Accounts Chem. Res.* **2006**, *39*, 169-175.

(2) Ganim, Z.; Chung, H. S.; Smith, A. W.; Deflores, L. P.; Jones, K. C.; Tokmakoff, A. *Accounts Chem. Res.* **2008**, *41*, 432-441.

(3) Woys, A. M.; Lin, Y.-S.; Reddy, A. S.; Xiong, W.; Pablo, J. J. de; Skinner, J. L.; Zanni, M. T. *J. Am. Chem. Soc.* **2010**, *132*, 2832-8.

(4) Manor, J.; Mukherjee, P.; Lin, Y.-S.; Leonov, H.; Skinner, J. L.; Zanni, M. T.; Arkin, I. T. *Structure* **2009**, *17*, 247-254.

(5) Remorino, A.; Korendovych, I. V.; Wu, Y.; DeGrado, W. F.; Hochstrasser, R. M. *Science* **2011**, *332*, 1206-1209.

(6) Deng, H.; Vu, D. V.; Clinch, K.; Desamero, R.; Dyer, R. B.; Callender, R. *J. Phys. Chem. B.* **2011**, *115*, 7670-7678.

(7) Pozo Ramajo, A.; Petty, S. A; Starzyk, A.; Decatur, S. M.; Volk, M. *J. Am. Chem. Soc.* **2005**, *127*, 13784-13785.

(8) Smith, A. W.; Lessing, J.; Ganim, Z.; Peng, C. S.; Tokmakoff, A.; Roy, S.; Jansen, T. L. C.; Knoester, J. *J. Phys. Chem. B.* **2010**, *114*, 10913-10924.

(9) Huang, C.-Y.; Getahun, Z.; Zhu, Y.; Klemke, J. W.; DeGrado, W. F.; Gai, F. *P. Natl. Acad. Sci. USA.* **2002**, *99*, 2788-2793.

(10) Petty, S. A; Decatur, S. M. *P. Natl. Acad. Sci. USA.* **2005**, *102*, 14272-14277.

(11) Kim, Y. S.; Liu, L.; Axelsen, P. H.; Hochstrasser, R. M. *P. Natl. Acad. Sci. USA.* **2008**, *105*, 7720-7725.

(12) Lin, Y.-S.; Shorb, J. M.; Mukherjee, P.; Zanni, M. T.; Skinner, J. L. *J. Phys. Chem. B.* **2009**, *113*, 592-602.

(13) Alfieri, K. N.; Vienneau, A.R.; Londergan, C. H. *Biochemistry.* **2011**, *50*, 11097-11108.

(14) Earnest, T. N.; Herzfeld, J.; Rothschild, K. J. *Biophys. J.* **1990**, *58*, 1539–1546.

(15) Beevers, A. J.; Kukol, A. *Protein Sci.* **2006**, *15*, 1127-1132

(16) Manor, J.; Khattari, Z.; Salditt, T,; Arkin, I. T. *Biophys. J.* **2005**, *89*, 563-571

(17) Chen, X.; Wang, J.; Boughton, A. P.; Kristalyn, C. B.; Chen, Z. *J. Am. Chem. Soc.* **2007**, *129*, 1420-1427.

(18) Boughton, A. P.; Yang, P.; Tesmer, V. M.; Ding, B.; Tesmer, J. J. G.; Chen, Z. *P. Natl. Acad. Sci. USA.* **2011**, *108*, E667-673.

(19) Nguyen, K. T.; Clair, S. V. Le; Ye, S.; Chen, Z. *J. Phys. Chem. B.* **2009**, *113*, 12169-12180.

(20) Ding. B.; Chen, Z. *J. Phys. Chem. B*, **2012**, *116*, 2545–2552

(21) Ye, S.; Nguyen, K. T.; Boughton, A. P.; Mello, C. M.; Chen, Z. *Langmuir* **2010**, *26*, 6471-6477.

(22) Ye, S.; Li, H.; Wei, F.; Jasensky, J.; Boughton, A. P.; Yang, P.; Chen, Z. *J. Am. Chem. Soc.* **2012**, *134*, 6237-43.

(23) Nguyen, K. T.; King, J. T.; Chen, Z. *J. Phys. Chem. B.* **2010**, *114*, 8291-8300.

(24) Wang, J.; Chen, X.; Clarke, M. L.; Chen, Z. *P. Natl. Acad. Sci. USA.* **2005**, *102*, 4978-83.

(25) Fu, L.; Ma, G.; Yan, E. C. Y. *J. Am. Chem. Soc.* **2010**, *132*, 5405-5412.

(26) Fu, L.; Xiao, D.; Wang, Z.; Batista, V. S.; Yan, E. C. Y. *J. Am. Chem. Soc.* **2013**, *135*, 3592-3598.

(27) Weidner, T.; Breen, N. F.; Li, K.; Drobny, G. P.; Castner, D. G. *P. Natl. Acad. Sci. USA.* **2010**, *107*, 13288-13293.

(28) Weidner, T.; Apte, J. S.; Gamble, L. J.; Castner, D. G. *Langmuir* **2010**, *26*, 3433-3440.

(29) Sawai, M. V.; Waring, A. J.; Kearney, W. R.; McCray, P. B.; Forsyth, W. R.; Lehrer, R. I.; Tack, B. F. *Protein Eng.* **2002**, *15*, 225-232.

(30) Yamaguchi, S.; Huster, D.; Waring, A.; Lehrer, R. I.; Kearney, W.; Tack, B. F.; Hong, M. *Biophys. J.* **2001**, *81*, 2203-2214.

(31) Mermut, O.; Phillips, D. C.; York, R. L.; McCrea, K. R.; Ward, R. S.; Somorjai, G. *J. Am. Chem. Soc.* **2006**, *128*, 3598-3607.

(32) Perry, A.; Neipert, C.; Space, B. *Chem. Rev.* **2006,** *106*, 1234-1258.

(33) Liu, J.; Conboy, J. C. *J. Am. Chem. Soc.* **2004**, *126*, 8376-8377.

(34) Ma, G.; Chen, X.; Allen, H. C. *J. Am. Chem. Soc.* **2007,** *129*, 14053-14057.

(35) Roeters, S. J.; van Dijk, C. N.; Torres-Knoop, A.; Backus, E. H. G.; Campen, R. k.; Bonn, M.; Woutersen, S. *J. Phys. Chem. A.* **2013,** Article ASAP.

(36) Sagle, L. B.; Cimatu, K.; Litosh, V. A; Liu, Y.; Flores, S. C.; Chen, X.; Yu, B.; Cremer, P. S. *J. Am. Chem. Soc.* **2011**, *133*, 18707-18712.

(37) Chen, X.; Flores, S. C.; Lim, S.-M.; Zhang, Y.; Yang, T.; Kherb, J.; Cremer, P. S. *Langmuir* **2010**, *26*, 16447-16454.

(38) Engel, M. F. M.; vandenAkker, C. C.; Schleeger, M.; Velikov, K. P.; Koenderink, G. H.; Bonn, M. *J. Am. Chem. Soc.* **2012**, *134*, 14781-14788.

(39) Li, H.; Ye, S.; Wei, F.; Ma, S.; Luo, Y. *Langmuir*. **2012**, *28*, 16979-16988.

(40) Wang, J.; Even, M. A; Chen, X.; Schmaier, A. H.; Waite, J. H.; Chen, Z. *J. Am. Chem. Soc.* **2003**, *125*, 9914-9915.

(41) Hamm, P.; Zanni, M. *Concepts and Methods of 2D Infrared Spectroscopy*; Cambridge University Press: Cambridge, U.K., 2011.

(42) Laaser, J. E.; Zanni, M. T. *J. Phys. Chem. A.* **2013**, Article ASAP

(43) Tamm, L. K.; Tatulian, S. A. *Q. Rev. Biophys.* **1997**, *30*, 365-429.

(44) Starzyk, A.; Barber-Armstrong, W.; Sridharan, M.; Decatur, S. M. *Biochemistry* **2005**, *44*, 369-376.

(45) Nguyen, K. T.; Soong, R.; Lm, S.-C.; Waskell, L.; Ramamoorthy, A.; Chen, Z. *J. Am. Chem. Soc.* **2010**, 132, 15112-15115.

(46) Moad, A. J.; Moad, C. W.; Perry, J. M.; Wampler, R. D.; Goeken, G. S.; Begue, N. J.; Shen, T.; Heiland, R.; Simpson, G. J. *J. Comp. Chem.* **2007**, *28*, 1996-2002.

(47) Manas, E. S.; Getahun, Z.; Wright, W. W.; DeGrado, W. F.; Vanderkooi, J. M. *J. Am. Chem. Soc.* **2000**, *122*, 9883-9890.

(48) Ji, N.; Ostroverkhov, V.; Chen, C.-Y.; Shen, R.-Y. *J. Am. Chem. Soc.* **2007**, *129*, 10056–10057

(49) Stiopkin, I.V.; Jayathilake, H. D.; Bordenyuk, A. N.; Benderskii, A. V. *J. Am. Chem. Soc.* **2008**, *130*, 2271–2275

(50) Nihonyanagi, S.; Yamaguchi, S.; Tahara, T. *J. Chem. Phys.***2009**,*130*, 204704

(51) Laaser, J. E.; Xiong, W.; Zanni, M. T.; *J. Phys. Chem. B.* **2011**,115, 2536-2546.

(52) Higgs, P. W. *Proc. R. Soc. Lond.* **1953**,220, 472-485.

(53) Moffitt, W. *J. Chem. Phys.* **1956**, 25, 467.

(54) Choi, J.-H.; Hahn, S.; Cho, M. *Int. J. Quantum Chem.* **2005**, *104*, 616-634.

(55) Mukherjee, P.; Kass, I.; Arkin, I. T.; Zanni, M. T. *J. Phys. Chem. B.* **2006**, *110*, 24740–24749

(56) Kuko1, A.; Torres, J.; Arkin, I. T. *J. Mol. Biol.* **2002**, *320*, 1109–1117

(57) Wang, L.; Middleton, C. T.; Singh, S.; Reddy, A. S.; Woys, A. M.; Strasfeld, D. B.; Marek, P.; Raleigh, D. P.; Pablo, J. J. D.; Zanni, M. T.; Skinner, J. L. *J. Am. Chem. Soc.* **2011**, *133*, 16062-16071.

(58) Pieniazek, P. a; Tainter, C. J.; Skinner, J. L. *J. Chem. Phys.* **2011**, *135*, 044701.

(59) Skinner, J. L.; Pieniazek, P. A.; Gruenbaum, S. M. *Accounts Chem. Res.* **2012**, *45*, 93-100.

(60) Krimm, S. *Fortschr. Hochpolym.-Forsh.,Bd.* **1960**, *2*, 241-254.

(61) Hubner, W.; Mantsch, H. H.; *Biophys. J.* **1991**, *59*, 1261-1272.

(62) Ramamoorthy, A.; Wei, Y.; Lee, D-K,; *Annu. Rep. NMR Spectrosc*. **2004**, *52*, 1-52.

(63) Flavell, R. R.; Muir, T.W.; *Acc. Chem. Res.***2009,** *42*, 107-116.

(64) Dawson, P.E.; Muir, T.W.; Clark-Lewis, I.; Kent, S. B.; *Science* **1994,** *266*, 776-779.

(65) Moran, S. D.; Decatur, S. M.; Zanni, M. T.; *J. Am. Chem. Soc.* **2012,** *134*, 18410-18416.

(66) Wang, L.; Schultz, P. G.; *Angew. Chem. Int. Ed. Engl.***2004**, *44*, 34-66.

(67) Taskent-Sezgin, H.; Chung, J.; Patsalo, V.; Miyake-Stoner, S. J.; Miller, A. M.; Brewer, S. H.; Mehl, R. A.; Greene, D. F.; Raleigh, D. P.; Carrico, I. *Biochemistry* **2009,** *48*, 9040-9046.

(68) Wang, J.; Lee, S.-H.; Chen, Z. *J. Phys. Chem. B.* **2008**, *112*, 2281-2290.

(69) Ye, S.; Nguyen, K. T.; Le Clair, S. V.; Chen, Z., *J. Struct. Biol.* **2009**, 168, 61-77.

CHAPTER 6

UNIQUE SITE-SPECIFIC STRUCTURAL INFORMATION OF A BIOMOLECULE AT MODEL MEMBRANE INTERFACE BY INCORPORATING ISOTOPE-LABELED SUM FREQUENCY GENERATION PROBES

Membrane structures of polypeptides and proteins are of essential importance to the biological scientific society. However, microscopic structure determination at the interface in situ is difficult due to the lack of appropriate analytical techniques. In this work, we demonstrated for the first time that, the isotope-labeled SFG technique we developed in Chapter 5 can serve as a new route for structure determination of a peptide associated with a single lipid bilayer *in situ*.

6.1. Introduction

Interfacial properties and functions of peptides and proteins are determined by molecular structures of peptides and proteins at the interfaces. It is important to obtain structural information of peptides and proteins at interfaces, which of biologically relevant research fields such as enzyme engineering, drug delivery and membrane biology [1-3].

Vibrational spectroscopic studies on isotope labeled samples have been successfully used to obtain site-specific structural knowledge on peptides and proteins. Because the peak frequency and linewidth are indicators for protein secondary structure and backbone solvation, the amide I band which mainly consists of the C=O stretching mode is often analyzed in the vibrational

spectroscopy. Isotope labeling 1-$^{12}C=^{16}O$ group into $^{13}C=^{16}O$ or $^{13}C=^{18}O$ isolates an amide I oscillator by a frequency shift of ~40 cm^{-1} or ~66 cm^{-1}, respectively [4]. One-dimensional infrared spectroscopy has utilized the amide I peak centers of the isotope labeled segment to study a variety of topics: α-helix stability, amyloid formation and local environmental differences in the hydrogen bonding for coiled-coil peptides.[4] Two-dimensional infrared spectroscopy can measure both the homogeneous and inhomogeneous linewidths of isotope labeled amino acids in the peptides, thus providing information about backbone disorder and local environment fluctuations. [5-8] By comparing the coupling constants between various isotope labeled vibrational pairs, 2DIR has been proved with a capability to shed light on the 3D tertiary structure of a transmembrane protein. [9] Besides the information provided by frequency and linewidth analysis, the intensities of the signal generated by the isotope labeled unit (we will refer it to isotope peak throughout this chapter) detected using light with different polarizations can be used to calculate the angles of individual amino acid dipole moment relative to the surface normal of the stacked bilayer in a FTIR cell. [10]

As described in the previous chapters, SFG is a vibrational spectroscopy based on the second-order nonlinear optical process. It measures the second-order nonlinear optical susceptibility $\chi^{(2)}$, which is nonzero only when the inversion symmetry of the sample is broken. This makes SFG an intrinsically surface-sensitive technique excluding the contribution from the bulk. During the past decade, SFG has been used to investigate the conformation and orientation of peptides and proteins at the biointerface. [11-16] More recently, assisted by deuterium isotope labeling on the side chains of a model peptide LKα14 and calculation of the individual side chain orientation, Castner, Weidner and their colleges showed that isotope labeling SFG has the potential to serve as a new route for structural determination at the interface, such as on an

inorganic surface, which is difficult to do using traditional X-ray diffraction or NMR spectroscopy.[17, 18]

Previously we have successfully demonstrated the feasibility of detecting SFG signal from a single isotope-labeled $^{13}C=O$ unit in the α-helical region of peptide ovispirin-1 (Figure 6.1) at the polystyrene/peptide solution interface. We showed that the amplitude of isotope peak can be used to obtain the twist angle of the peptide backbone. [19] In this chapter, we will focus on a more biological-relevant system than the polystyrene surface: ovispirin-1 associated with a lipid bilayer (serving as a model cell membrane). Solid-state NMR results showed that ovispirin-1 lies primarily in the plane of the POPC/POPG bilayer with a tilt angle of ~84 degrees relative to the surface normal.[20] 2DIR, combined with molecular dynamics simulation, similarly suggested the α-helical structure and planar orientation of ovispirin-1 associated with POPC/POPG vesicles. The trend in the 2DIR linewidths of different isotope labeled residues in the peptide provided the additional information that the hydrophilic residues of ovisprin-1 were facing the lipid headgroups.[6]

Here we used ten different ovispirin-1 mutants, each isotope labeled at a specific site in the α-helical region of the peptide. We investigated the variations of the SFG signal generated from these mutants, including linewidth, frequency and intensity as a function of the residue number. The unique site-specific information from SFG results was compared with the subsequently performed molecular dynamics simulations. We found that the dependence of the SFG peak linewidths and frequencies on the isotope labeled amino acid residue number indicated that ovispirin-1 is lying beneath the headgroups of the DPPG/dDPPG bilayer, and the positive \constructive interference of all the isotope peaks suggests that the peptide tilts more towards the surface normal in the DPPG/dDPPG bilayer than in the POPC:POPG=3:1 vesicles previously

reported [6]. The MD simulation results suggested that the C terminus of peptide was tilted towards the lipid headgroups due to the electrostatic interaction between the negative charged headgroups and the positive Lys 15 and Lys 16 amino acids.

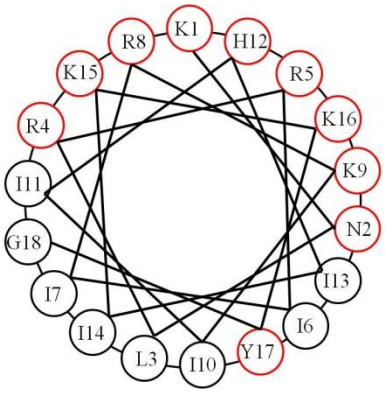

Figure 6.1 Helical wheel diagram of ovispirin-1. The polar amino acids are circled by red while the nonpolar one by black.

6.2. Experimental Details

6.2.1 Materials

Regular ovispirin-1 (with the sequence H_2N-KNLRR IIRKI IHIIK KYGCOOH) and isotope labeled samples were synthesized by Peptide 2.0 Inc. We isotope labeled the 1-^{12}C=O of I6, I7, I10, I11, I13 and I14 into ^{13}C=O. For R4, R5, R8, H12, we mutated them into ^{13}C=O isotope labeled G4, G5, G8 and G12 to reduce the synthesis expense. Previously research with MD simulations has shown that the mutation will not change the property and behavior of ovispirin-1 peptide [21].

6.2.2 SFG Spectroscopy

Details on SFG theory [22] and our near-total-reflection SFG experimental geometry [23,24] have been presented in previous publications and previous chapters. In the SFG experiment, we

overlap two laser beams (i.e. one visible beam at 532 nm and one frequency tunable infrared beam from 1300 cm^{-1} to 4300 cm^{-1}) spatially and temporally at the bottom side of a right-angle CaF_2 prism. The DPPG/dDPPG bilayer was deposited on the CaF_2 prism with Langmuir-Blodgett and Langmuir-Schaefer method for the outer and inner leaflets, respectively [24,25]. After the deposition, the lipid bilayer was immersed in a 2 mL reservoir throughout the SFG spectra collection process. The water subphase was changed into 0.2 mM pH= 7.1 buffer before adding ovisipirin-1 peptide. 20 μL ovisipirin-1 stock solution (1 mg/mL) was added into the subphase to achieve a final concentration of 10 μg/mL. A magnetic microstirrer was used to facilitate the homogenous distribution of the ovispirin-1 molecules in the subphase in contact with the lipid bilayer. The experiments were carried under room temperature (~20 ˚C) and the DPPG/dDPPG bilayer remained in the gel phase. Time dependent SFG signal at 1655 cm^{-1} was used to monitor the *in situ* adsorption time-scale of the ovispirin-1 to the lipid bilayer. SFG spectra in the amide I range were subsequently collected in the ppp polarization of the sum frequency, visible and IR beams with a step of 1 cm^{-1}. The optics set-up was placed in a nitrogen chamber to minimize the sharp spectra dips in the amide I range resulted from the absorption of the IR beam in the optical pathway by water vapor. The SFG spectrometer we used is picosecond (YAG-based) from Altos. Inc. The pump laser is Nd:YAG at 1064 nm and the pulse width is 20ps with a repetition rate of 20Hz. The spectra resolution is 4 cm^{-1} ensuring the accuracy in the frequency and lineshape observation of the isotope labeled peaks.

6.2.3 Calculation with the Hamiltonian Approach

The parameters in the calculation with the Hamiltonian approach were described in detail Chapter .[19] The one exciton Hamiltonian is constructed with the amide I vibrational modes of each residue as the local oscillators. The couplings between local modes were calculated by

transition-dipole coupling model. The transition dipole is defined to oriented 27.5 degrees while the Raman tensor is 34 degrees away from the CO bond of a local mode. The vibrational frequency for an isolated un-labeled oscillator is~1650 cm $^{-1}$ which corresponds to a diagonal force constant (DFC) of 1.605 mdyn Å^{-1} cm^{-1} [26]. The frequency for the isotope labeled mode is set to be 1600 cm^{-1} to better distinguish the isotope peak. This frequency is slightly lower than the observed frequencies of the isotope peaks in the SFG experiment but the sinusoidal trend of the isotope label mode amplitude does not change when shifting the labeled oscillator frequency and does not change the conclusion of our analysis.

6.2.4 SFG Signal from Lipid Bilayers

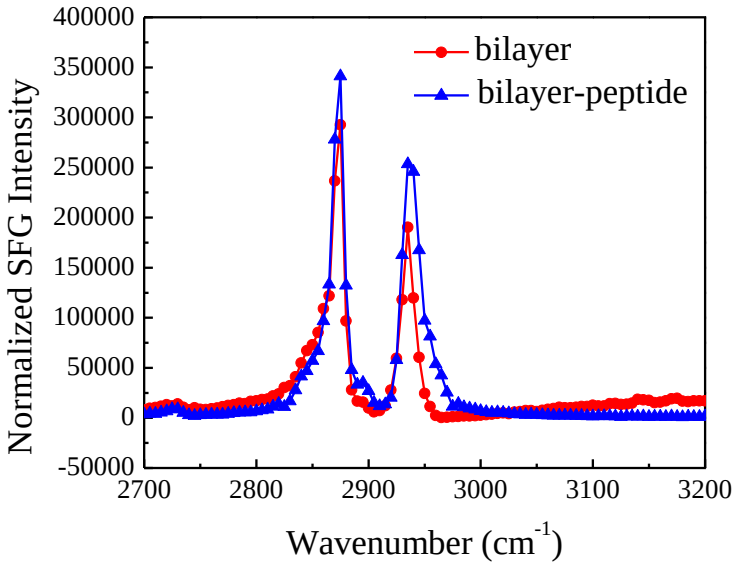

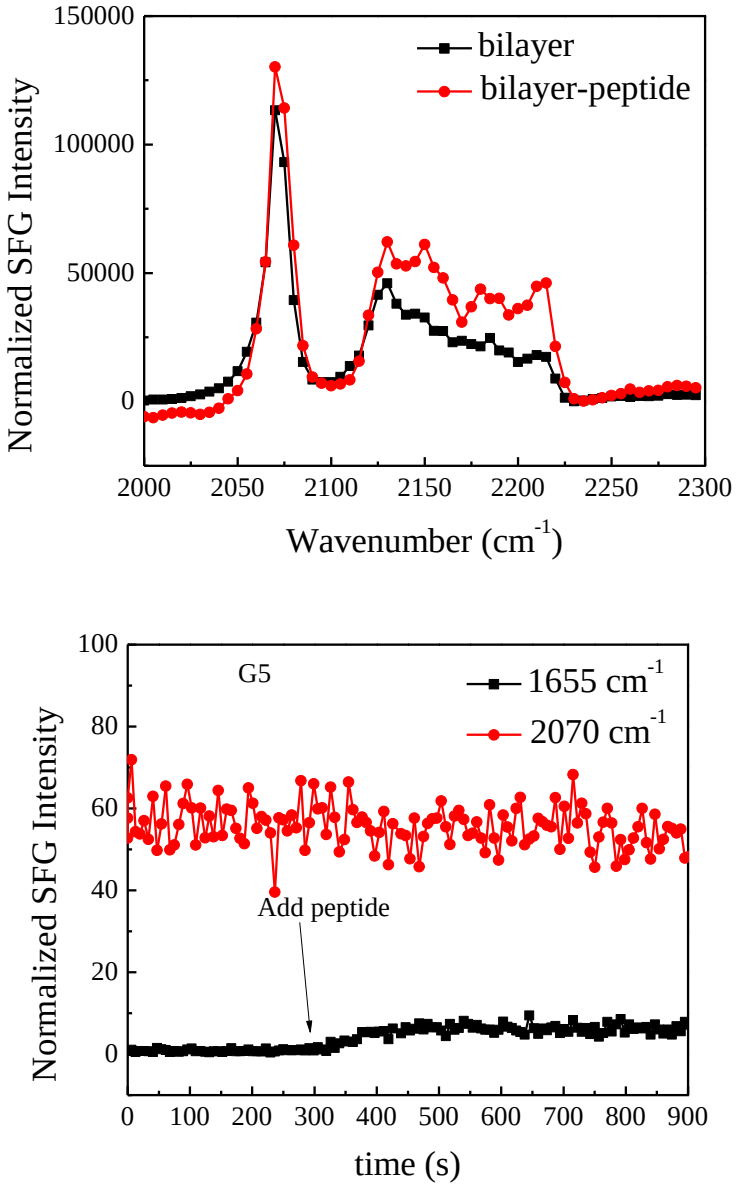

Figure 6.2 SFG spectra in ssp polarization collected from lipid bilayers a) for the inner layer DPPG in the CH stretching frequency region b) for the outer layer dDPPG in the CD stretching frequency region when after adding isotope labeled peptide G5 into the subphase and equilibrating for 2hrs. c) Time-dependent SFG signal in ssp polarization at 1655 cm^{-1} (from the peptide) and 2070 cm^{-1} (from the outer layer dDPPG) after the addition of the peptide stock solution.

6.2.5 SFG Signal from Amide I Range

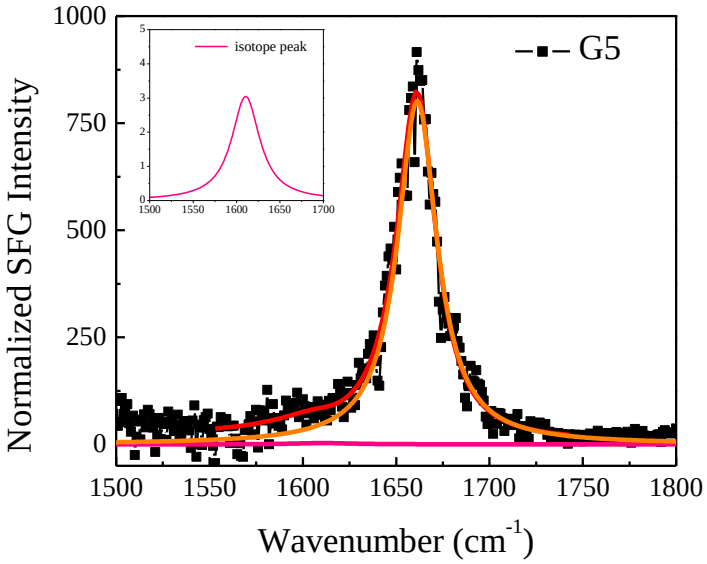
G5
isotope peak
Normalized SFG Intensity
Wavenumber (cm-1)
1000
750
500
250
0
1500
1550
1600
1650
1700
1750
1800

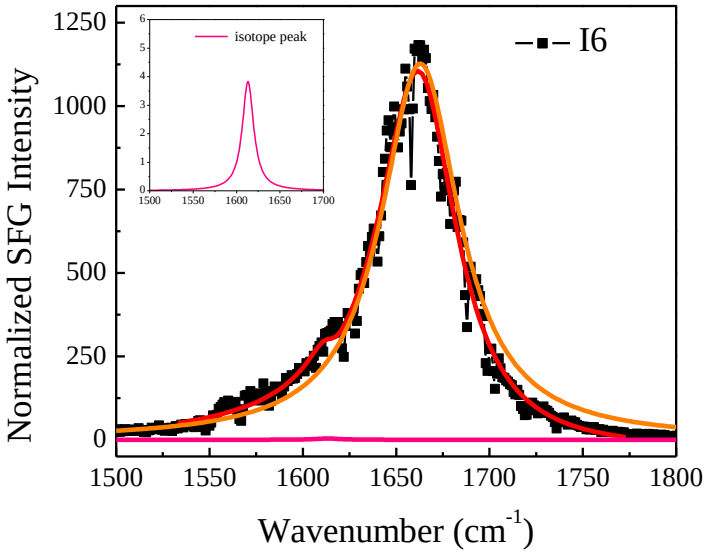
I6
isotope peak
Normalized SFG Intensity
Wavenumber (cm-1)
1250
1000
750
500
250
0
1500
1550
1600
1650
1700
1750
1800

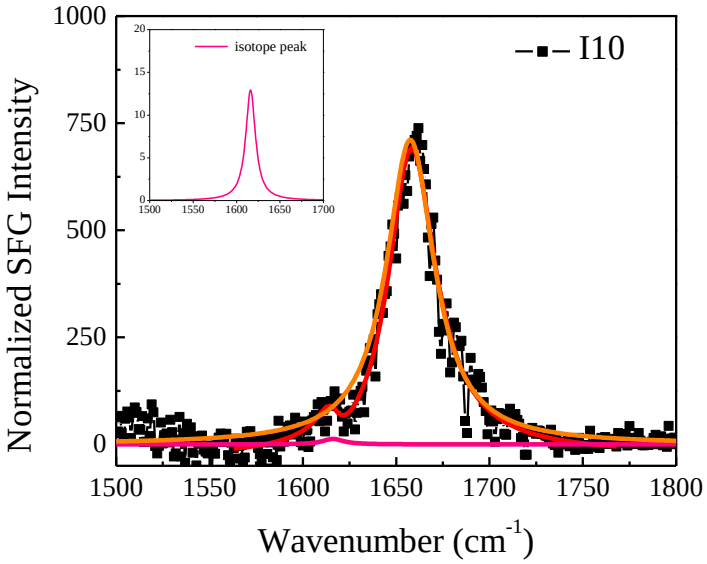
Normalized SFG Intensity
Wavenumber (cm-1)
I10
isotope peak

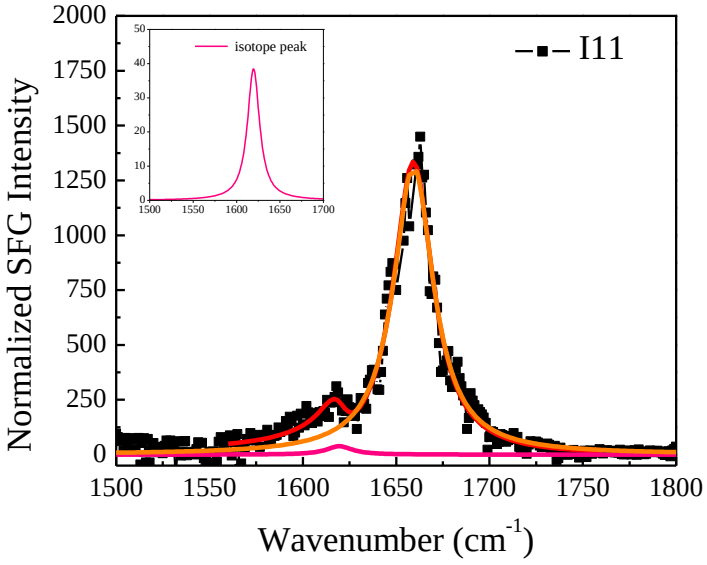
Normalized SFG Intensity
Wavenumber (cm-1)
I11
isotope peak

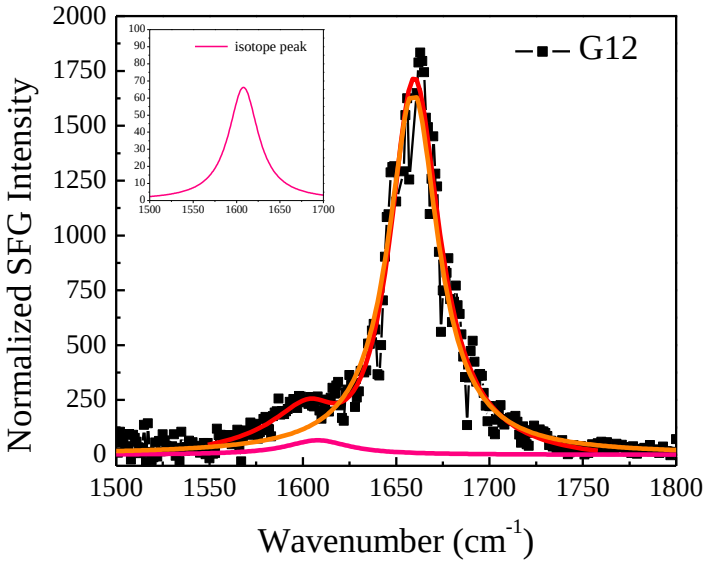
G12
isotope peak
Normalized SFG Intensity
Wavenumber (cm-1)

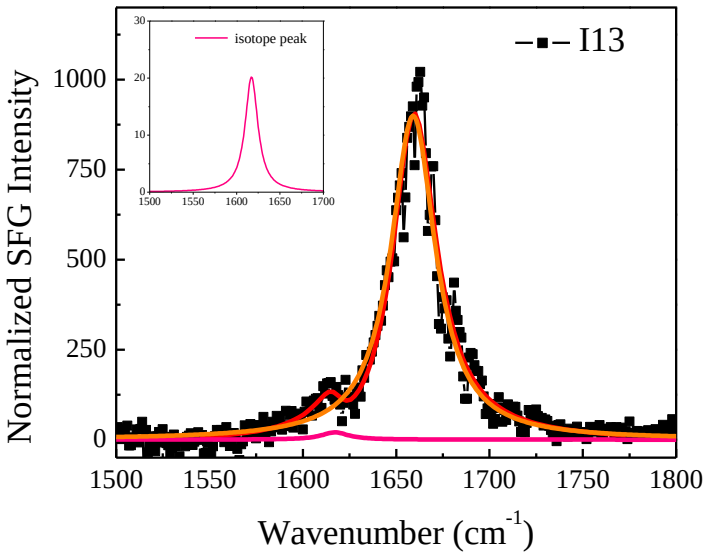
I13
isotope peak
Normalized SFG Intensity
Wavenumber (cm-1)

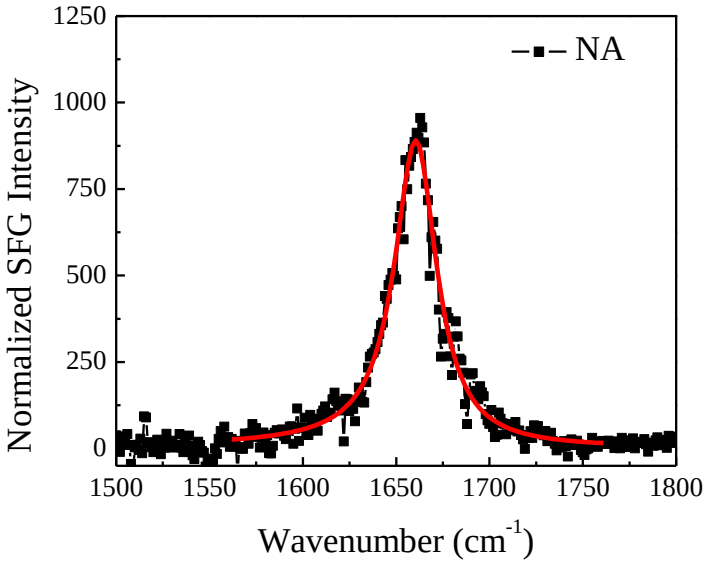

Figure 6.3 SFG spectra collected from ovispirin-1 isotope labeled at different sites (G5, I6, I10, I11, G12 and I13 - from top to bottom) and non-isotope labeled ovispirin (NA) in the amide I frequency range when associated with a DPPG/dDPPG bilayer in the ppp polarization.

6.2.6 Simulation Details

The starting structure of the ovispirin-1 was obtained from PDB entry 1HU5. The starting configuration of the DPPG bilayer was constructed by the CHARMM-GUI membrane builder. The initial XY dimensions of the DPPG bilayer were 65 Å × 65 Å, which are large enough to accommodate the ovispirin-1 peptide. Each of the top and bottom leaflets of the DPPG bilayer consists of 64 lipids (total 2 × 64 = 128 lipids). To match our SFG spectra observations, the model of the ovispirin-1 was initially buried near the lipid head group of the DPPG bilayer.

In the presented work, all MD simulations were performed using NAMD2.8 package with CHARMM36 force field. For our MD simulations, the CHARMM36 lipidforce field parameters were used for the DPPG bilayer system, CHARMM27 force field parameters were used for ovispirin-1 peptide, and the modified TIP3P force field were used to model water molecules.. In the initial equilibrium stage, the MD runs were done using the NPT ensemble

(constant number of atoms, pressure, and temperature). Production simulations were performed for 35 ns using the NPγT (Scott E. Feller & Richard W. Pastor 1999) ensemble (constant number of atoms, pressure, surface tension, and temperature). The Nose-Hoover method was applied to maintain a constant temperature of 303.15 K, in which the DPPG (transition temperature is 314 K) bilayer can exist in a gel phase. The Langevin-piston algorithm was employed to maintain a constant pressure at 1 atm along the Z direction, while the XY area varied with a constant surface tension of γ = 34.0 dyn/cm for NPγT ensemble.The short-range van der Waals interactions were smoothly switched off by a force-switching function at a twin range cutoff between 10 Å and 12 Å. The long-range electrostatic interactions were calculated using the Particle Mesh Ewald method, with a mesh of 72×72×90 grid points for fast Fourier transformation and a sixth-order B-spline interpolation to compute the potential and forces between grid points. All covalent bonds involving hydrogen atoms were constrained using the RATTLE method. The velocity Verlet method was used to integrate Newton's equations with a time step of 2.0 fs.

6.3. Results

6.3.1 SFG spectra of isotope labeled ovispirin-1 samples

After adding the ovispirin-1 peptide stock solution into the subphase in contact with the bilayer, the SFG signal at 1655 cm^{-1} contributed by the α-helical component increases for 200 s and remains stable for the next few hours (for the full duration of SFG experiments). SFG spectra collected in the CH and CD stretching frequency ranges, which are generated by the lipid chains of the hydrogenated inner leaflet and deuterated outer leaflet, respectively, were collected before adding peptides to the subphase and after the 1655 cm^{-1} signal became stable. For both

lipid leaflets, the SFG spectra have minimal changes (Figure 6.2). Since ovispirin-1 is an antimicrobial peptide, above a certain solution concentration, it would disrupt the model lipid bilayer severely. In that case, the ovispirin-1 molecules are likely to adopt multiple orientations[27,15], making our site-specific observations difficult to interpret. In that situation, the bilayer leaflets would undergo fast flip-flop and result in the decrease of SFG signals detected from each leaflet. Clearly, this is not the case here which suggested that during the peptide interaction process, the lipid bilayer remains largely intact. We showed previously, when the peptide solution concentration is low, the peptides are more likely to adopt a relatively uniform orientation than in the case where the peptides disrupt the membrane lipid bilayer [27,15].

SFG spectra in the amide I range were collected from ten isotope-labeled ovispirin-1 mutants as well as the non-isotope-labeled ovispirin sample associated with the lipid bilayer (Figure 6.3 and 6.4). The fitting parameters for these SFG spectra are summarized in Table 6.1. For all the peptide samples, the peaks are centered at ~1660 cm^{-1} which agrees with the typical peak center for α-helices[28]. The isotope peak appears as a shoulder to the main peak. The isotope peak center varies from 1606 cm^{-1} to 1620 cm^{-1} and the peak width spans from 6 cm^{-1} to 24 cm^{-1} with isotope labels at different amino acid postions. Also the intensity of the isotope peak changes with different isotope labeling sites. In order to quantify this effect, we fit the spectra with two peaks and calculated the $\chi_{\text{isotope peak}}/\chi_{\text{main peak}}$ ratio (Table 6.1). Next we will explain what the peak center, peak width and $\chi_{\text{isotope peak}}/\chi_{\text{main peak}}$ ratio variations imply in terms of peptide location, structural disorder and site-specific orientation.

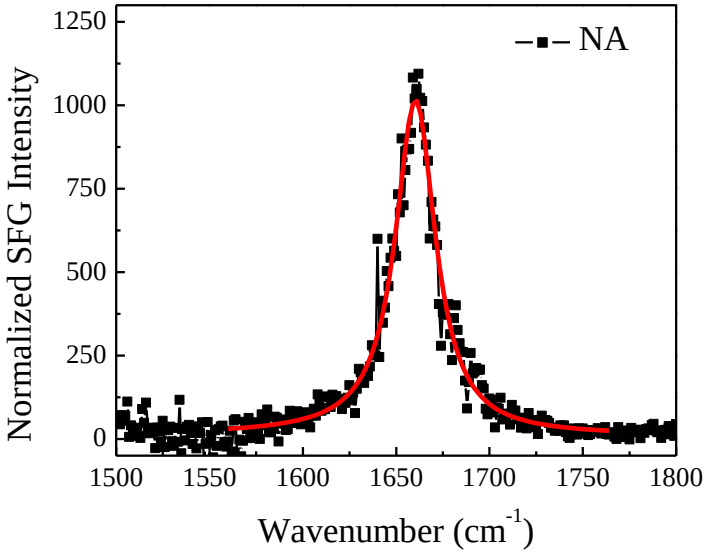
NA
Normalized SFG Intensity
Wavenumber (cm-1)
1250
1000
750
500
250
0
1500
1550
1600
1650
1700
1750
1800

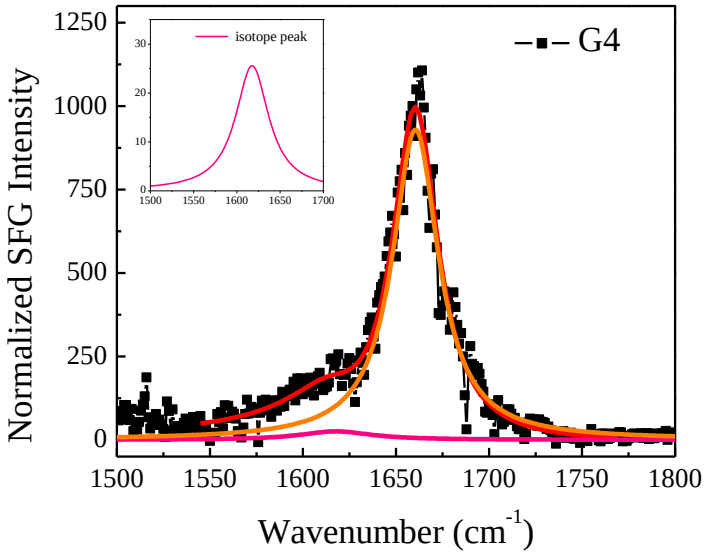
G4
isotope peak
Normalized SFG Intensity
Wavenumber (cm-1)
1250
1000
750
500
250
0
1500
1550
1600
1650
1700
1750
1800

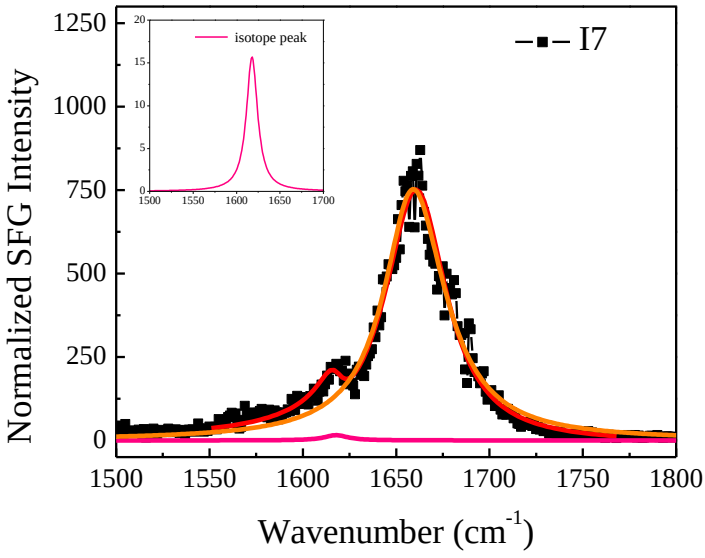
I7
isotope peak
Normalized SFG Intensity
Wavenumber (cm-1)
1250
1000
750
500
250
0
1500
1550
1600
1650
1700
1750
1800

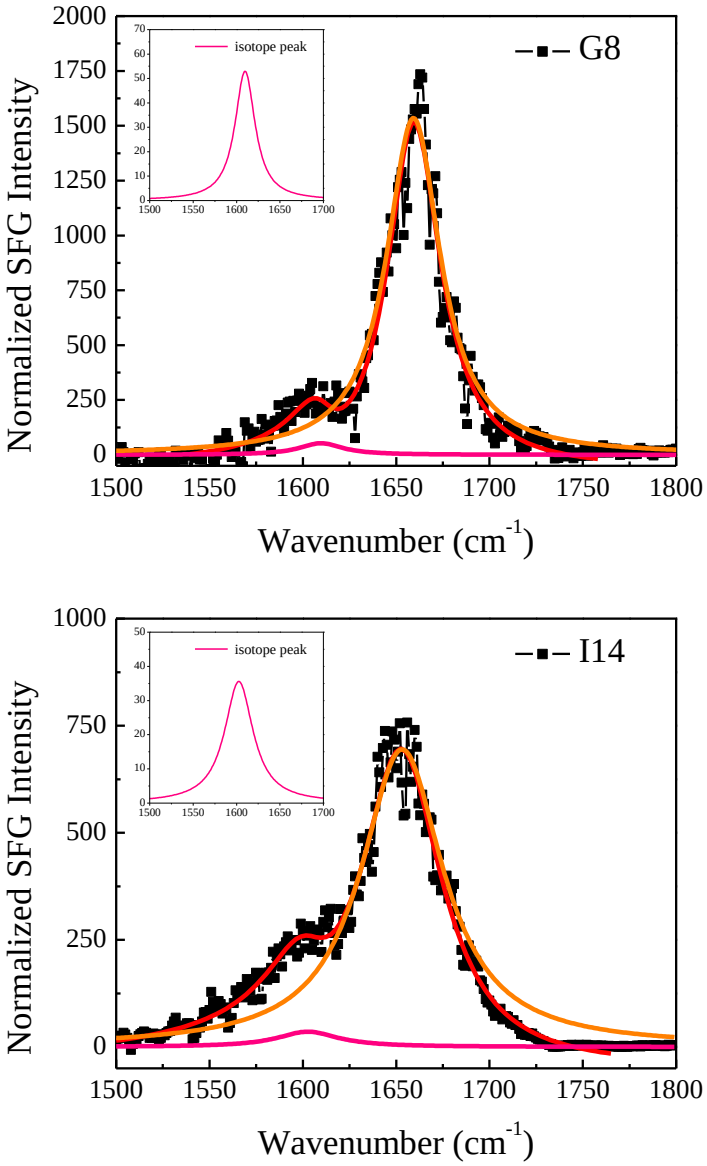

Figure 6.4 SFG spectra collected from ovispirin-1 isotope labeled at different sites (G4, I7, G8, I14- from top to bottom) in the amide I frequency range when associated with a DPPG/dDPPG bilayer in the ppp polarization.

	Isotope peak center(cm^{-1})	Isotope peakwidth (cm^{-1})	Main peak center (cm^{-1})	Main peak width (cm^{-1})	$\chi_{isotope\ peak}/\chi_{main\ peak}$
NA	NA	NA	1660.5±0.5	13.4±0.6	0

G4	1618 ±3	23 ±8	1659 ±1	15.1 ±0.6	0.20 ±0.03
G5	1608 ±2	14 ±6	1661.8 ±0.5	13.0 ±0.1	0.068 ±0.005
I6	1614 ±3	8 ±6	1662.7 ±0.5	25.6 ±0.6	0.059 ±0.004
I7	1618 ±2	8 ±3	1660.7 ±0.7	19.8 ±0.8	0.148 ±0.006
G8	1610 ±2	15 ±5	1659.3 ±0.7	16.8 ±0.7	0.184 ±0.002
I10	1616 ±2	8 ±4	1657.9 ±0.6	15.5 ±0.6	0.135 ±0.001
I11	1620 ±1	6 ±3	1659.3 ±0.6	12.8 ±0.5	0.16 ±0.01
G12	1607 ±1	18 ±8	1658.7 ±0.9	16.3 ±0.7	0.18 ±0.02
I13	1616 ±3	7 ±5	1659.7 ±0.6	14.4 ±0.5	0.13 ±0.02
I14	1606 ±7	23 ±9	1655.6 ±1.7	23.0 ±5.0	0.21 ±0.03

Table 6.1 Fitting parameters of SFG spectra collected from ovispirin-1 without and with isotope labeled units at different sites

6.3.2 The implications of the isotope peakcenters and peakwidths

a)

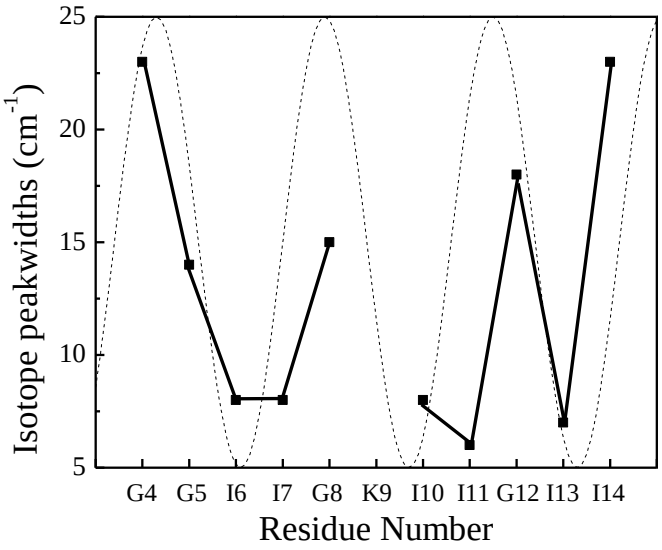

b)

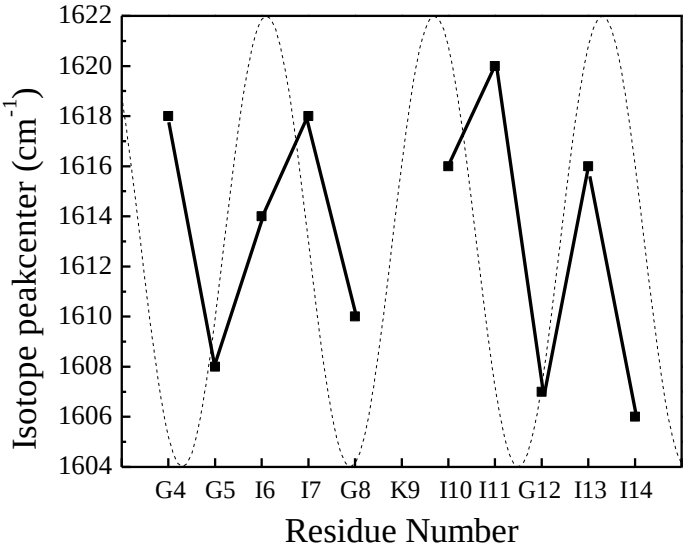

Figure 6.5 The a) widths and b) central frequencies of the collected SFG isotope peaks as a function of isotope labeled amino acid residue number

It is well known that the homogeneous linewidth of a vibrational peak is largely determined by the coupling between the vibrational modes, whereas the inhomogeneous broadening is caused by the environment. For example, previously 2D-IR linewidths study indicates that the homogeneous linewidth of a specific isotope labeled residue is an intrinsic property of the peptide and the inhomogeneous broadening, on the other hand, is a probe of the structure disorder (measured by hydrogen-bond length) and the environment (measured by electrostatic interactions) around that residue.[6,8] Similarly, FTIR and one dimensional SFG, which measures the total linewidth, can also be used to reflect the different environment of various peptide amino acid residues. Recently, the total linewidth information was extracted from FTIR spectra to map the environmental polarity in proteins. [29] Here, as shown in Figure 6.5a, SFG isotope peaks of the amino acids that are on the hydrophilic face of the α-helix, G4, G5, G8 and G12 have wider linewidths than those of the residues on the hydrophobic face, I6, I7, I10 and I11. It was shown previously that the region from G4 to I16 in ovispirin-1 forms well-

defined α-helical structure [6,30] associated with lipids or lipid-mimic agent TFE and thus the differences of the linewidth in Figure 6.5a are mainly due to the electrostatic interactions rather than the structural disorder. This linewidth variation trend agrees with previous 2D-IR diagonal linewidth (total and inhomogeneous linewidth) study and implicates that the peptides is buried beneath the lipid headgroups. Large frequency fluctuations of the isotope peak centers contributed by the G4, G5, G8 and G12 amino acid residues are induced by the lipid headgroups and water while the smaller frequency fluctuations for I6, I7 I10 and I11 are caused by the hydrophobic lipid interior.

The linewidth of the SFG signal detected from I14 using SFG is very different from what was measured by 2DIR [6]. I14 is on the hydrophobic face of the peptide helical wheel and exhibited a narrow diagonal line width in the 2DIR study of ~12 cm^{-1}. But in SFG measurement, the linewidth is ~24 cm^{-1}. It is worth noting that in the 2DIR experiment, ovispirin-1 was studied when associated with POPG bilayer, while SFG experiments were carried out on DPPG bilayer. In the aforementioned 2DIR experiments, signals detected from the isotope labeled peaks of K15 and K16 have an abrupt increase in linewidth which was attributed to the denaturation of the peptide starting from those two amino acids. Here, it is likely due to the large negative-charge density of DPPG, the peptide denaturation starts earlier at residue I14 and the larger linewidth of the SFG signals detected form I14 is an indicator of the structure disorder.

Figure 6.5b displays the peakcenter frequencies of different isotope labeled peaks, which have a similar sinusoidal variation trend to that of linewidth. The isotope peakcenter frequencies for G5, G8 and G12 are lower, while the peakcenter frequencies of the signals detected from I6, I7, I10 and I11 are higher. This indicates that inside the core α-helical structure, the peakcenter frequency of the isotope labeled $^{13}C=O$ group is a probe to the local electrostatic interaction. As

indicated above, the G5, G8 and G12 are interacting with lipid head groups, while I6, I7, I10 and I11 are facing the hydrophobic lipid interior.

However, although G4 has a wide linewidth, similar to that of G5, G8 and G12, its peakcenter remains at a higher frequency, different from G5, G8 and G12. The fact that both the SFG signal peakcenters from G4 and I14 have the highest frequency suggested that the sinusoidal trend breaks down at the ends where the α-helix unravels. This agrees with the results obtained from previous 2DIR study that the frequency is correlated with the hydrogen-bond length [8]. While the linewidth reflects the dynamics of hydrogen-bond length and electric fields, frequency prediction requires the absolute hydrogen-bond length and electric fields. Therefore their varation trends are correlated but not the same.

6.3.3 The intensities of the isotope peaks are related to peptide orientation

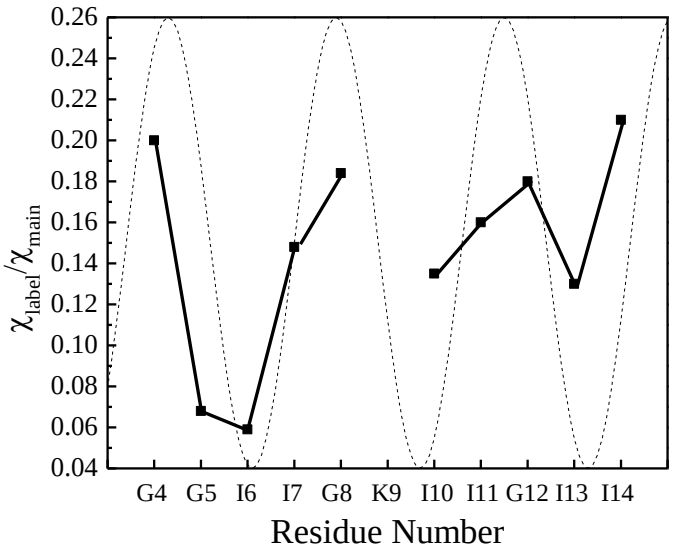

Figure 6.6: Experimentally measured SFG signal strength ratio χ_{label}/χ_{main} as a function of residue number

a) [0,0,0]

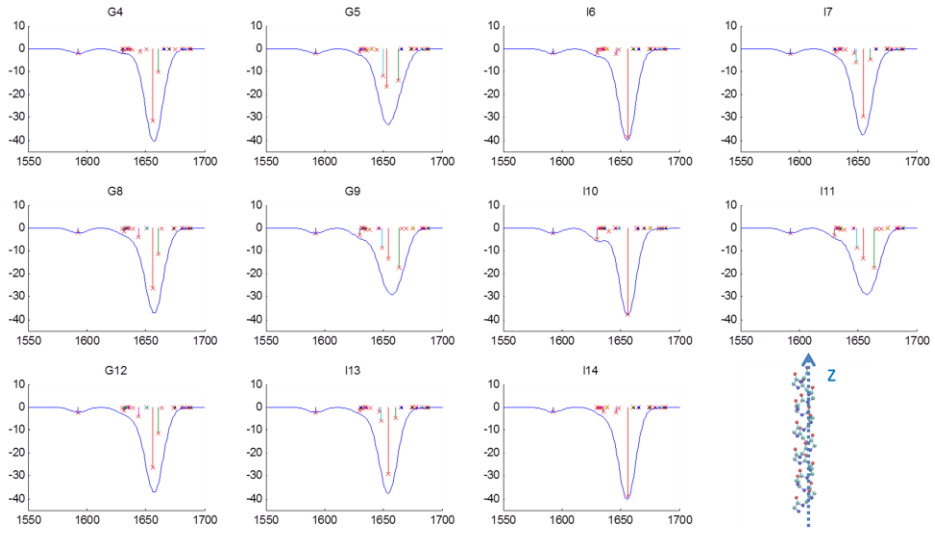
G4
G5
I6
I7
G8
G9
I10
I11
G12
I13
I14
z

b) [0,0,60]

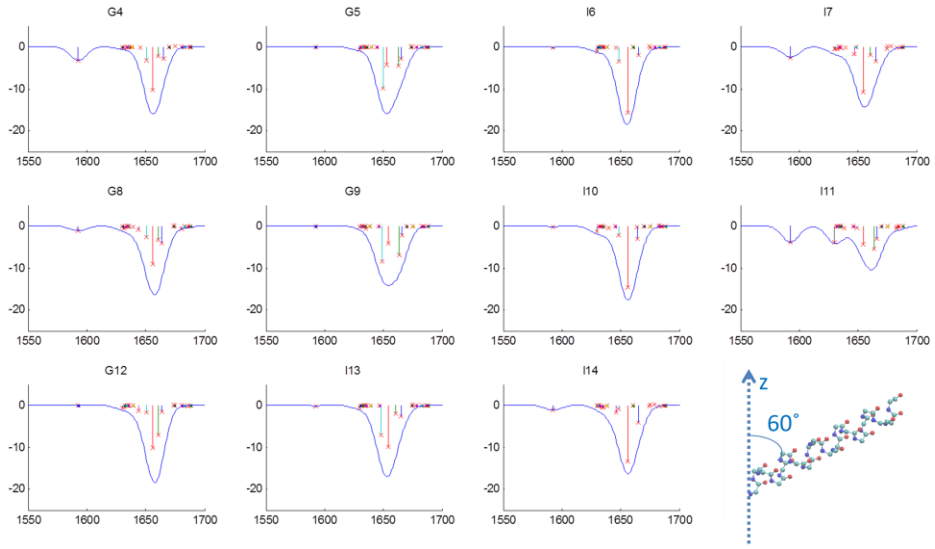
G4
G5
I6
I7
G8
G9
I10
I11
G12
I13
I14
z
60°

c) [0,0,80]

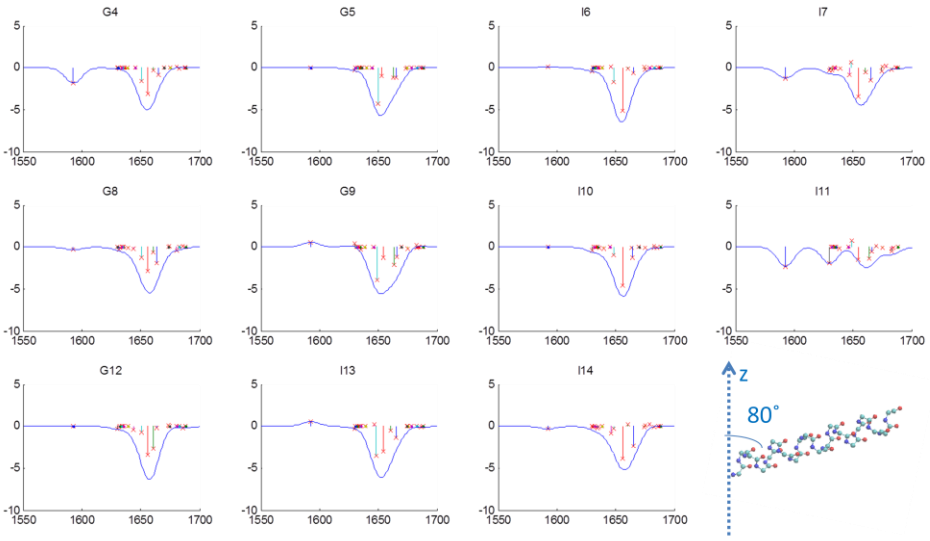

Figure 6.7 Simulated heterodyne SFG spectra for an ideal helix tilting from surface normal at different tilt angles a) 0 b) 60 c) 80 degrees. The x axis is the wavenumbers (cm^{-1}) and the y axis is χ_{zzz} (a.u).

The intensity of an SFG signal detected from a chemical group is sensitive to the orientations of this chemical group. In order to gain some insight into the isotope labeled carbonyl group orientations, we fitted the spectra with two peaks (Table 6.1) and observed a sinusoidal variation trend of χ_{label}/χ_{main} ratio and found that all the isotope peaks have positive interferences with the main peak. In order to understand what this implies we simulated SFG spectra corresponding to an ideal helix (with one amino acid isotope labeled at a different site) that tilting different angles from the surface normal with the Hamiltonian approach.

Previously, SFG spectra from different polarization combinations have been utilized to deduce orientations of different secondary structures such as α-helices [31,32], 3_{10} helices [31,33] and β-sheets [34]. Such studies require the knowledge of the molecular hyperpolizabilities for those secondary structures. To calculate the hyperpolarizability, a perturbation treatment which has

been used to calculate IR response for infinite regular polypeptide chains was adopted. [35] In this treatment, amplitudes of peptide SFG-active groups (e.g. the A mode and E1 mode for the α-helix) were calculated from the symmetry relations between local modes generated by individual amino acid residues. In this study, because an isotope label was incorporated into different sites of an α-helix, the symmetry of the local modes was severely disrupted. Thus, we adopt the Hamiltonian approach to solve the eigenvalue problem for the Hamiltonian matrix. In other words, when an isotope label was incorporated into the Hamiltonian matrix of an α-helix, there might not be two eigenvalues (namely A mode and E1 mode) only but instead, the new Hamiltonian matrix generates several new delocalized modes (for example, I11 in Figure 6.7a).

As shown in Figure 6.7a, for an ideal helix, when the tilt angle of the helix axis is 0 degree relative to the surface normal (i.e. standing up on the surface), all the amide I transition dipoles have the same orientation relative to the surface normal and the χ_{label}/χ_{main} ratios are the same for samples with different residue isotope labeled. However, when the peptide has a tilt angle as 60 degrees (Figure 6.7b), the z projection of the amide I modes has a sinusoidal variation as a function of the residue number that matches the χ_{label}/χ_{main} ratio with a 3.6 residue pitch. When the peptide has an even bigger tilt angle as 80 degrees (Figure 5c), some of the isotope peaks start to have a different phase from the main peak (destructive interference). This is because while the helical axis is 80 degrees relative to the surface normal which still points to the positive directions of the z axis (i.e. pointing up), some C=O transition dipoles point to the negative direction of the z axis (i.e. pointing down). Due to the different absolute orientations, SFG signals exhibit different phases.

The comparison between the experimental and simulated data suggests that different from the POPC:POPG=3:1 case where the peptide almost lies flat in the membrane, the peptide axis has a smaller tilt relative to the surface normal (less than 80 degrees) associated with a DPPG lipid bilayer. G4, G8, G12 are tilted up more than I6, I7, I10, I11 and I13. For the two possible absolute orientations with C-terminus or N-terminus tilting up, combining with the conclusion that G4, G8 and G12 are facing towards the hydrophilic lipid headgroups from the isotope peakwidth and peakcenter study, we deduce that the current scenario is the C terminus is more tilting up towards the lipid headgroups.

6.3.4 Site-specific orientation of G8 and I11

	χ_{zzz}/χ_{xxz}	$\theta_{\delta}/^{\circ}$	$\theta_{Gaussian}/^{\circ}$	$\theta_{0ns}/^{\circ}$	$\theta_{10ns}/^{\circ}$	$\theta_{25ns}/^{\circ}$	$\theta_{35ns}/^{\circ}$
G8	3.1 ±0.2	149±3	151±3	137	126	58	54
I11	2.28 ±0.08	142±2	142±2	140	147	81	93

Table 6.2: χ_{zzz}/χ_{xxz} is the SFG susceptibility ratio derived from the spectra taken with different polarization combinations for the isotope peak collected from samples G8 and I11. θ_{δ} and $\theta_{Gaussian}$ are calculated tilt angles of C=O transition dipole moment relative to the surface normal, assuming a δ distribution and Gaussian distribution with 15 degrees of full-width-at-half-maxima, respectively, in a Ψ-averaged case (Ψ is the rotational angle around the isotope labeled peptides). θ_{0ns} ,θ_{10ns} ,θ_{25ns} and θ_{35ns} are tilted angles derived from the MD simulation snapshots at different moments.

Previously we have shown that the χ_{zzz}/χ_{xxz} ratio of a single amide-I unit can be derived from the SFG isotope peak taken with different polarization combinations: ssp and ppp [19]. By correlating the experimental χ_{zzz}/χ_{xxz} ratio with the theoretical tilt-angle dependence curve, the tilt angle of the isotope labeled transition dipole relative to the membrane surface normal can be deduced. In this work, we successfully obtained quantitative fitting parameters from the isotope peak in the ssp spectra for two isotope labeled peptides: G8 and I11. The tilt-angle dependence

of χ_{zzz}/χ_{xxz} for both the Ψ-averaged and Ψ=0˚ and Ψ=90˚ case, where Ψ is the rotational angle around the isotope labeled transition dipole, was reported [19]. There is less than 10˚ difference for the calculated tilt angles between the Ψ-averaged and Ψ-fixed cases and thus here we only show the result for the Ψ-averaged cases (Table 6.2) assuming a δ distribution and Gaussian distribution with 15 degrees of full-width-at-half-maxima. We need to emphasize that the method here cannot distinguish the difference of a transition dipole pointing to the positive z axis (θ) and the negative z axis (180-θ) with the same tilt angle. For instance, the θ_δ for G8 is derived to be either 31 ± 3 or149 ± 3, however in section 6.3.2 and 6.3.3, we concluded all the amide I transition dipoles are more or less pointing to the positive z aixs, and thus all the corresponding θ_δ is in the range of 90~180 degrees. Therefore, 31 ± 3 is excluded in the calculation result of the θ_δ for G8.

6.3.5 MD simulation results

(a)

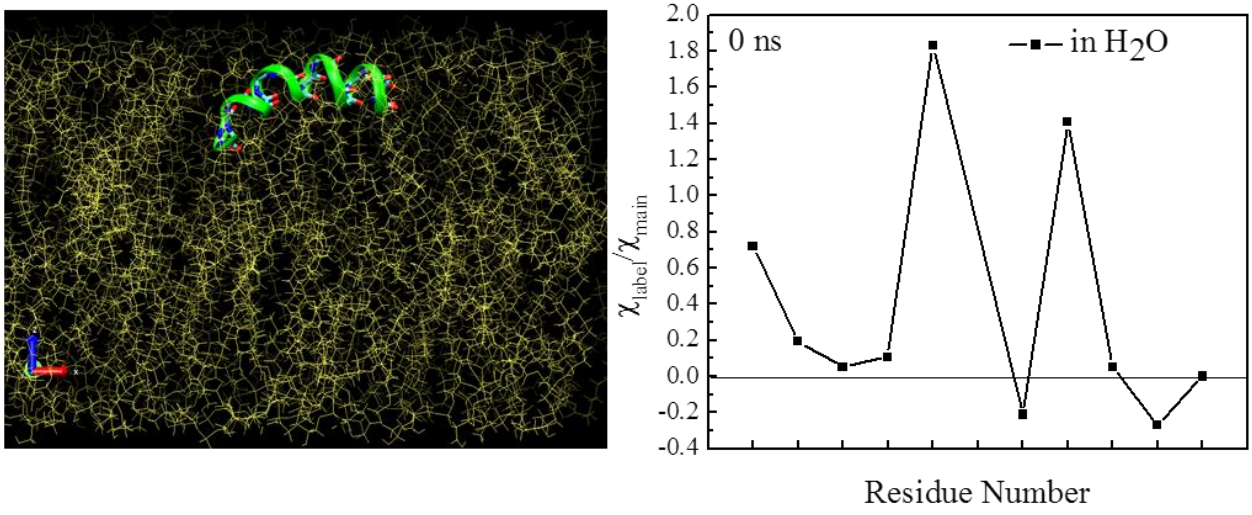

(b)

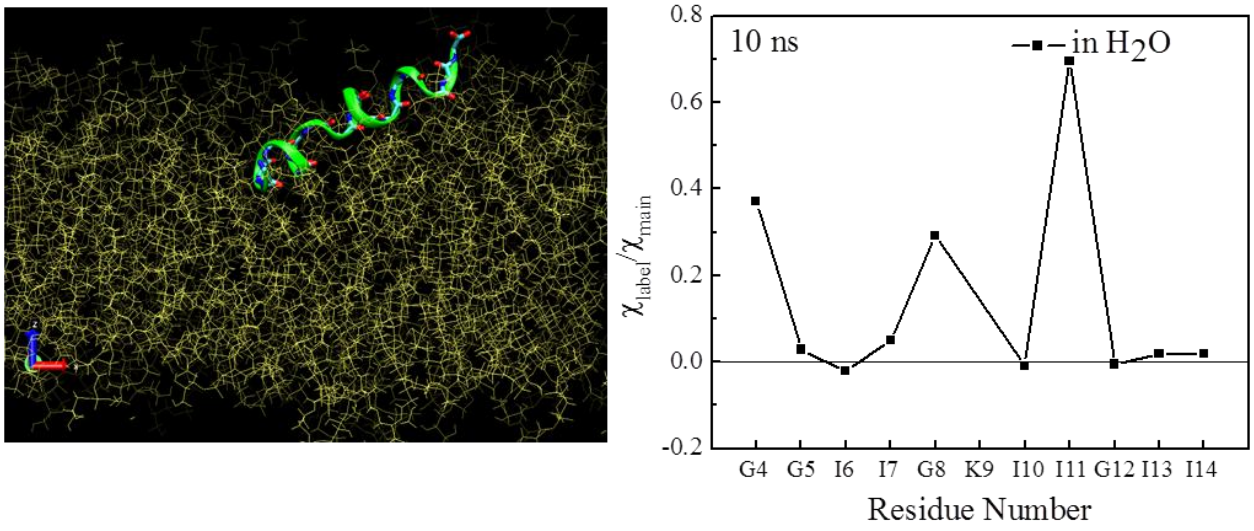
10 ns
in H_2O
χ_{label}/χ_{main}
0.8
0.6
0.4
0.2
0.0
-0.2
G4 G5 I6 I7 G8 K9 I10 I11 G12 I13 I14
Residue Number

(c)

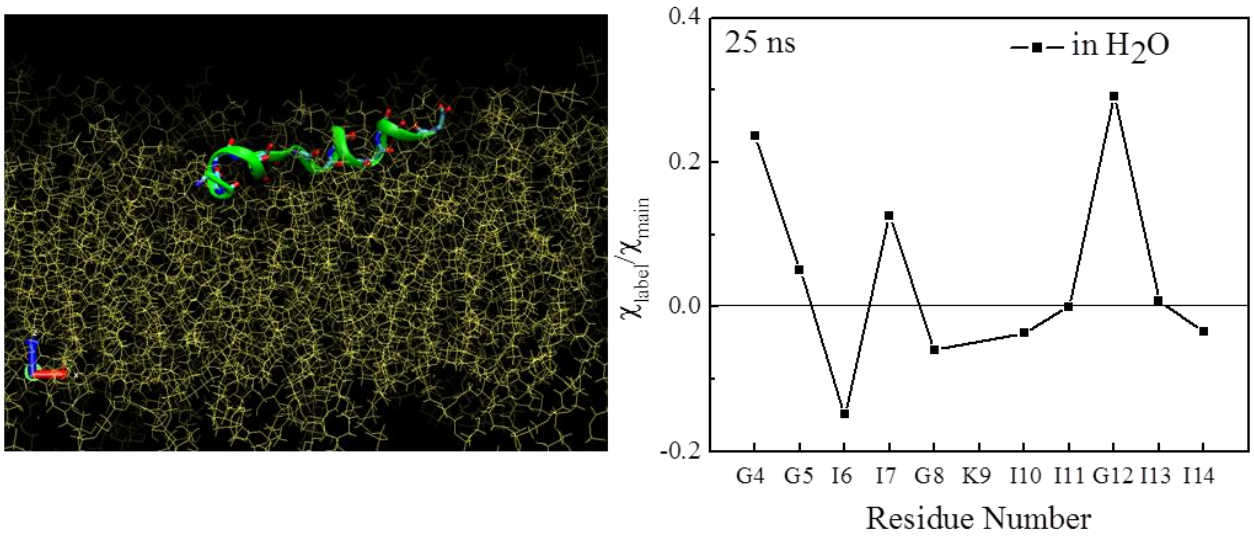
25 ns
in H_2O
χ_{label}/χ_{main}
0.4
0.2
0.0
-0.2
G4 G5 I6 I7 G8 K9 I10 I11 G12 I13 I14
Residue Number

(d)

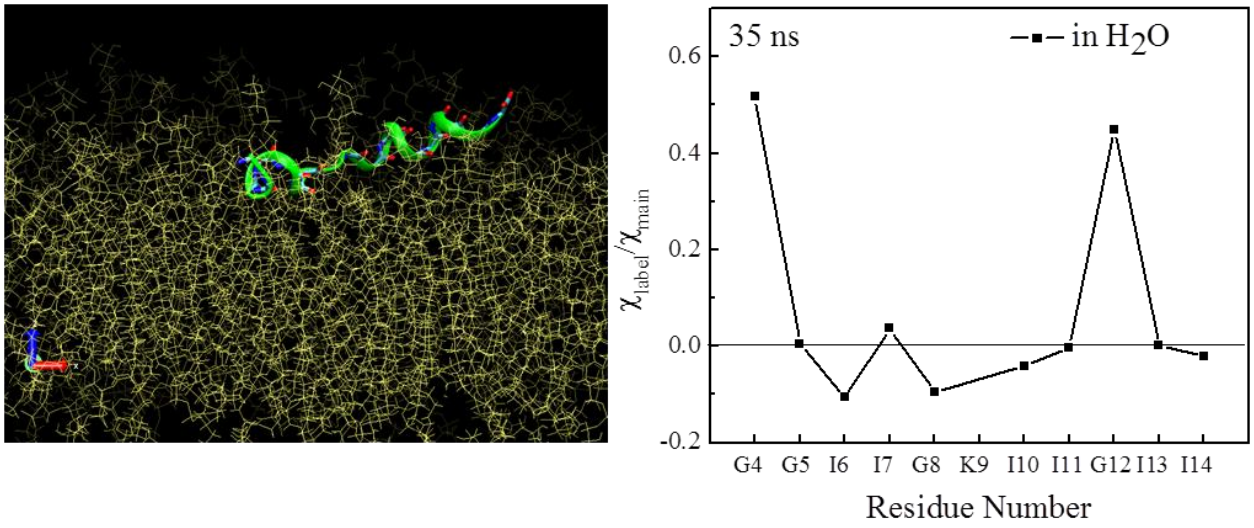

Figure 6.8 Snapshots and simulated SFG signal strength ratio χ_{label}/χ_{main} of the ovispirin-1 conformation and orientation at a) 0 ns b) 10 ns c) 25 ns d) 35 ns

Starting from a completely flat geometry, the peptide time-dependent trajectory shows a characteristic of the C terminus tilting up. As a result, the helix axis of ovispirin associated with a DPPG/dDPPG bilayer is not as parallel to the surface as in the case when associated with a POPC/POPG bilayer. Physically this might due to the increased negative charge density of the DPPG lipid which facilitates the interaction between the positive charged amino acids K15, K16 and the slightly charged H12 at the C terminus. This tilt-up characteristic is well captured by the isotope labeled SFG as discussed in section 6.3.2 and 6.3.3.

In order to compare with the variation trend of the experimental SFG signal strength ratio χ_{label}/χ_{main}, we simulated the SFG signal strength ratio χ_{label}/χ_{main} of ovispirin-1 at different snapshot times with the Hamiltonian approach outlined in section 6.3.2 and 6.3.3. We can compare the results from two aspects. First, the relative intensity trend of the SFG signal strength

ratio χ_{label}/χ_{main} is related to the peptide secondary structure. Comparing the 0 ns snapshot, 10 ns snapshot has a similar signal strength ratio trend up to residue I13, which suggests that at 10 ns the peptide largely maintains its original α-helical structure. However, this trend breaks down from G8 for the 25 ns and 35 ns snapshots. This suggests that the α-helical structure was disrupted around G8 for the 25 ns and 35 ns snapshots. In the MD simulation the peptide unravels its α-helical structure starting from G8 for the 25 ns and 35 ns snapshots and this is reflected in the variation trend of the simulated SFG signal strength ratio χ_{label}/χ_{main}. Second, the sign of the SFG signal strength ratio χ_{label}/χ_{main} is related to the helical axis orientation. As discussed in section 6.3.2 and 6.3.3, when the helix is more or less lying down on the surface, some of the C=O groups start to point to the negative direction of the z axis (i.e. pointing down) and thus the isotope peak has destructive interference with the main peak. In the 0 ns, 25 ns and 35 ns snapshots, several amino acids exhibit a strength ratio χ_{label}/χ_{main} less than -0.1, but for 10 ns snapshot, because the helical axis have a smaller tilt angle relative to the surface normal than the other snapshots, all the isotope peaks either have a constructive interference or a very small destructive interference ($\chi_{label}/\chi_{main} > 0.02$).

The experimental SFG signal strength ratio χ_{label}/χ_{main} (Figure 6.6) has a similar variation trend to the simulated one at the 10 ns (up to G12). This disruption in α-helix from G8 to I11for the 25 ns and 35 ns snapshots is not reflected in the experimentally observed variation trend. This suggests that in the current experimental condition, the α-helical structure is largely maintained. However, the breakdown of the similarity to the 10 ns snapshot from G12 suggests the denaturation starting from I14 affects the α-helical structure in the C terminus. Interestingly, all the experimental SFG signal strength ratios of χ_{label}/χ_{main} have positive signs, indicating the

helix axis has a relatively small tilt angle relative to the surface normal similar to the case in the 10 ns snapshot.

The tilt angles of the C=O transition dipole relative to the surface normal for G8 and I11 of different snapshots were shown in Table 2. It is clear that 10 ns better agrees with the experimentally derived angles than 25 ns and 35 ns. This again demonstrates that the α-helical unraveling starting from G8 for the 25 ns and 35 ns snapshots is not captured in the current experiment.

6.4. Discussion

In this chapter, for the first time, we have reported that $^{13}C=O$ can be used as a SFG probe for studying the site-specific structural information of peptides in model cell membranes. Very recently, a review paper on IR probes by Kim and Cho has summarized the criteria for useful IR probes [36] and one important requirement is that the probe should have large transition dipole strength for detection. It is more challenging to look for SFG probes in this regard: the second-order nonlinear susceptibility $\chi^{(2)}$ is a Kronecker product of the oscillator's Raman tensor and the transition dipole moment thus in order for the SFG signal of the probe to be detected, both the transition dipole moment and Raman tensor should have fairly large strength. Our work presented here has shown that with homodyne detection SFG, the isotope labeled $^{13}C=O$ signal can be detected and the peak center frequency, linewidth and intensity can be quantified in the ppp polarization combination for peptides associated with model cell membranes. Besides, the intrinsic SFG principle overcomes two limitations of isotope labeling infrared spectroscopy mentioned in the above review [36]: 1. The spectra window of the isotope labeling amide I vibrations overlaps with the infrared band of peptide side chains and this causes a problem in case of large proteins. For SFG, the contribution from side chains is minimized because, in large

proteins, side chains likely point to different directions, which leads to the cancellation of the SFG signal. 2. The broad combination band (2000-2500 cm^{-1}) of water bending and librational mode brings significant water background contribution in infrared spectroscopy. In SFG, water background comes from the interfacial water and when the protein molecule replaces the interfacial water molecules, the water background in SFG is largely suppressed.

With the advances in heterodyne detection SFG [37, 38,39], the SFG signal to noise ratio of the isotope peaks will be improved and more accurate orientation information can be extracted with SFG signal measured using more polarization combinations such as ssp and sps. The recent advance of the two dimensional SFG [40, 41]will greatly extend the application of isotope labeling SFG and provides insights into the peptide dynamics and mode coupling at the interface.

6.5 Conclusion

In this chapter, ten ovispirin-1 mutants, each isotope labeled at a specific site in the α-helical region of the peptides were used. The dependence of the SFG peak linewidths and frequencies on the isotope labeled amino acid residue number revealed that ovispirin-1 is lying beneath the headgroups of the DPPG/dDPPG bilayer. The positive\constructive interference of all the isotope peak indicated that the peptide backbone tilts around 60 degrees relative to the surface normal in the DPPG/dDPPG bilayer with the C terminus closer to the headgroup region. The MD simulation performed suggested that the C terminus of peptide was tilted towards the lipid headgroup region due to the electrostatic interaction between the negative charged headgroups and the positive charged Lys 15 and Lys 16 amino acids.

6.6 References

(1) Bloom, J. D.; Meyer, M. M.; Meinhold, P.; Otey, C. R.; MacMillan, D.; Arnold, F. H. *Current Opinion in Structural Biology* **2005**, *15*, 447–52.

(2) Petitpas, I.; Bhattacharya, A A; Twine, S.; East, M.; Curry, S. *The Journal of Biological Chemistry* **2001**, *276*, 22804–9.

(3) Opella, S. J.; Marassi, F. M. *Chemical Reviews* **2004**, *104*, 3587–606.

(4) Decatur, S. M. *Accounts of Chemical Research* **2006**, 39, 169-75.

(5) Ganim, Z.; Chung, H. S.; Smith, A. W.; Deflores, L. P.; Jones, K. C.; Tokmakoff, A. *Accounts of Chemical Research* **2008**, *41*, 432–41.

(6) Woys, A. M.; Lin, Y.-S.; Reddy, A. S.; Xiong, W.; Pablo, J. J. de; Skinner, J. L.; Zanni, M. T. *Journal of the American Chemical Society* **2010**, *132*, 2832–8.

(7) Lin, Y.-S.; Shorb, J. M.; Mukherjee, P.; Zanni, M. T.; Skinner, J. L. *The Journal of Physical Chemistry. B* **2009**, *113*, 592–602.

(8) Mukherjee, P.; Kass, I.; Arkin, I. T.; Zanni, M. T. *The Journal of Physical Chemistry. B* **2006**, *110*, 24740–9.

(9) Remorino, A.; Hochstrasser, R. M. *Accounts of Chemical Research* **2012**, *45*, 1896–905.

(10) Arkin, I. T. *Current Opinion in Chemical Biology* **2006**, *10*, 394–401.

(11) Jung, S.-Y.; Lim, S.-M.; Albertorio, F.; Kim, G.; Gurau, M. C.; Yang, R. D.; Holden, M. a; Cremer, P. S. *Journal of the American Chemical Society* **2003**, *125*, 12782–6.

(12) Mermut, O.; Phillips, D. C.; York, R. L.; McCrea, K. R.; Ward, R. S.; Somorjai, G. a *Journal of the American Chemical Society* **2006**, *128*, 3598–607.

(13) Boughton, A. P.; Yang, P.; Tesmer, V. M.; Ding, B.; Tesmer, J. J. G.; Chen, Z. *Proceedings of the National Academy of Sciences of the United States of America* **2011**, *108*, E667–73.

(14) Fu, L.; Liu, J.; Yan, E. C. Y. *Journal of the American Chemical Society* **2011**, *133*, 8094–7.

(15) Ding, B.; Chen, Z. *The Journal of Physical Chemistry. B* **2012**, *116*, 2545–52.

(16) Roeters, S. J.; Dijk, C. N. van; Torres-Knoop, a; Backus, E. H. G.; Campen, R. K.; Bonn, M.; Woutersen, S. *The Journal of Physical Chemistry. A* **2013**, *117*, 6311–22.

(17) Weidner, T.; Castner, D. G. *Physical Chemistry Chemical Physics : PCCP* **2013**, *15*, 12516–24.

(18) Weidner, T.; Breen, N. F.; Li, K.; Drobny, G. P.; Castner, D. G. *Proceedings of the National Academy of Sciences of the United States of America* **2010**, *107*, 13288–93.

(19) Ding, B.; Laaser, J. E.; Liu, Y.; Wang, P.; Zanni, M. T.; Chen, Z. *The Journal of Physical Chemistry. B* **2013**, *117*, 14625-34.

(20) Yamaguchi, S.; Huster, D.; Waring, a; Lehrer, R. I.; Kearney, W.; Tack, B. F.; Hong, M. *Biophysical Journal* **2001**, *81*, 2203–14.

(21) Woys, A. M.; Lin, Y.-S.; Reddy, A. S.; Xiong, W.; Pablo, J. J. de; Skinner, J. L.; Zanni, M. T. *Journal of the American Chemical Society* **2010**, *132*, 2832–8.

(22) Moad, A. J.; Simpson, G. J. *The Journal of Physical Chemistry B* **2004**, *108*, 3548–3562.

(23) Ye, S.; Nguyen, K. T.; Clair, S. V Le; Chen, Z. *Journal of Structural Biology* **2009**, *168*, 61–77.

(24) Nguyen, K. T.; Clair, S. V Le; Ye, S.; Chen, Z. *The Journal of Physical Chemistry. B* **2009**, *113*, 12358–63.

(25) Tamm, L. K.; Mcconnell, H. M. *Biophysical Journal* **1985**, *37*, 105-13.

(26) Torii, H.; Tasumi, M. *Journal of Chemical Physics* **1992**, *96*, 3379-87.

(27) Yang, P.; Ramamoorthy, A.; Chen, Z. *Langmuir* **2011**, *27*, 7760–7.

(28) Tamm, L. K.; Tatulian, S. A. *Quarterly Reviews of Biophysics* **1997**, *30*, 365–429.

(29) Manor, J.; Feldblum, E. S.; Zanni, M. T.; Arkin, I. T.; Campus, E. J. S. *the Journal of Physical Chemistry Letters* **2012**, 6–11.

(30) Sawai, M. V; Waring, A. J.; Kearney, W. R.; McCray, P. B.; Forsyth, W. R.; Lehrer, R. I.; Tack, B. F. *Protein Engineering* **2002**, *15*, 225–32.

(31) Nguyen, K. T.; Clair, S. V Le; Ye, S.; Chen, Z. *The Journal of Physical Chemistry. B* **2009**, *113*, 12169–80.

(32) Ding, B.; Soblosky, L.; Nguyen, K.; Geng, J.; Yu, X.; Ramamoorthy, A.; Chen, Z. *Scientific Reports* **2013**, *3*, 1854.

(33) Ye, S.; Nguyen, K. T.; Chen, Z. *The Journal of Physical Chemistry. B* **2010**, *114*, 3334–40.

(34) Nguyen, K. T.; King, J. T.; Chen, Z. *The Journal of Physical Chemistry. B* **2010**, *114*, 8291–300.

(35) Miyazawa, T. *The Journal of Chemical Physics* **1960**, *32*, 1647.

(36) Kim, H.; Cho, M. *Chemical Reviews* **2013**, 113, 5817-5847.

(37) Ji, N.; Ostroverkhov, V.; Chen, C.-Y.; Shen, Y.-R. *Journal of the American Chemical Society* **2007**, *129*, 10056–7.

(38) Stiopkin, I. V; Jayathilake, H. D.; Bordenyuk, A. N.; Benderskii, A. V *Journal of the American Chemical* **2008**, 2271–2275.

(39) Nihonyanagi, S.; Yamaguchi, S.; Tahara, T. *The Journal of Chemical Physics* **2009**, *130*, 204704.

(40) Xiong, W.; Laaser, J. E.; Mehlenbacher, R. D.; Zanni, M. T. *Proceedings of the National Academy of Sciences of the United States of America* **2011**, 2–7.

(41) Laaser, J. E.; Zanni, M. T. *The Journal of Physical Chemistry. A* **2012**, *117*, 5875-90.

.

CHAPTER 7

SUMMARY AND OUTLOOK

Membrane associated peptides and proteins with unique biological functions have drawn extensive attention due to their enormous therapeutic potential. Being an intrinsic surface-sensitive technique, Sum Frequency Generation (SFG) Spectroscopy has the capability to elucidate both structural and orientational information of biological molecules at biointerfaces, e.g., cell membranes. However, there are significant experimental and theoretical challenges in adapting this application from simple model peptides to more complex systems associated with cell membranes. Thus, my dissertation aimed at developing SFG data analysis and experimental methods in order to answer biological questions.

In Chapter 2, we elucidated structure and orientations of a simple linear helical peptide, Pep-1. Lipid bilayers prepared using hydrogenated and deuterated 1,2-dipalmitoyl-sn-glycero-3-phosphoglycerol (DPPG and dDPPG) and 1-palmitoyl-2-oleoyl-sn-glycero-3-phospho-(1'-rac-glycerol) (POPG), were used in the experiments to represent gel-phase and fluid-phase lipid bilayers, respectively. Our SFG results indicated that Pep-1 molecules adopted a β-sheet conformation when adsorbed to the surface of gel-phase DPPG lipid bilayers. When interacting with fluid-phase POPG lipid bilayers, Pep-1 adopted a mix of α-helical and β-sheet structures over a broad range of peptide concentrations. The orientation distribution of the α-helical Pep-1 segment associated with the fluid-phase bilayers was found to depend on the peptide

concentration. SFG orientation analysis showed that Pep-1 molecules adopted an orientation nearly perpendicular to the plane of the bilayer for peptide concentrations of 0.28 μM and 1.4 μM. When the Pep-1 concentration was increased to 7.0 μM, combined SFG and ATR-FTIR measurements showed that Pep-1 molecules were associated with the bilayer with a broad orientation distribution. Our results demonstrated that both lipid bilayer phase and peptide concentration affect the conformation and orientation of Pep-1 molecules associated with model cell membranes, which is crucial to the translocation process of CPPs. A combination of SFG and ATR-FTIR studies can be used to determine the conformation and orientation of CPPs interacting with model cell membranes *in situ*.

A previously developed SFG data analysis method was used in Chapter 2 to determine the membrane orientation of the linear α-helical structure of Pep-1. Many α-helices in peptides and large proteins may not be linear, but instead, they show structural distortions. In Chapter 3, we demonstrated the power of SFG by studying non-linear helical peptides. We successfully developed and applied data analysis methods to determine the membrane orientation of two types of bent helices (with or without a disruption between the two helical segments). The observed SFG signal changes capture the aggregating process of LL-37 on membrane. In addition, our SFG results on cholesterol-containing lipid bilayers indicate the inhibition effect of cholesterol on peptide-induced membrane permeation process.

In Chapters 2 and 3, both wild-type (full-length) LL-37 and Pep-1 peptides were investigated. However, in peptides or proteins, different segments may play different roles according to the properties of the consisted amino acids within these segments. G protein-coupled receptor kinase 5 (GRK5) is thought to associate with membranes in part via N and C-terminal segments that are typically disordered in available high resolution crystal structures. In

Chapter 4 we investigated the interactions of these regions with model cell membranes using combined SFG and ATR-FTIR techniques. It was found that both regions are associated with POPC lipid bilayers but adopt different structures when doing so: GRK5 residues 2–31 ($GRK5_{2–31}$) was in random coil whereas $GRK5_{546–565}$ was partially helical. When the subphase for the $GRK5_{2–31}$ peptide was changed to 40% TFE/60% 10 mM phosphate pH 7.4 buffer, a large change in the SFG amide I signal indicated that $GRK5_{2–31}$ became partially helical. By inspecting the membrane behavior of two different segments of $GRK5_{2–31}$, namely, $GRK5_{2–24}$ and $GRK5_{25–31}$, we found that residues 25–31 are responsible for membrane binding, whereas the helical character is imparted by residues 2-24. With SFG, we deduced that the orientation angle of the helical segment of $GRK5_{2–31}$ is 46±1˚ relative to the surface normal in 40% TFE/60% 10 mM phosphate pH=7.4 buffer but increases to 78±11˚ with higher ionic strength. We also investigated the effect of PIP_2 in the model membrane and concluded that the POPC:PIP_2 (9:1) lipid bilayer did not change the behavior of either peptide compared to a pure POPC lipid bilayer. With ATR-FTIR, we also found that Ca^{2+} calmodulin is able to extract both peptides from the POPC lipid bilayer, consistent with the role of this protein in disrupting GRK5 interactions with the plasma membrane in cells.

In Chapter 4, we studied interfacial behavior of different peptide segments (N-terminus peptide and C-terminus peptide) in a protein (GRK5) as well as different segments ($GRK5_{2–24}$ and $GRK5_{25–31}$) within one peptide ($GRK5_{2–31}$) using SFG and ATR-FTIR. Now we further ask a question whether SFG is sensitive enough to detect structural information such as orientation of one single amino acid segment in the peptide backbone to probe local structure of biomolecules at interfaces. In Chapter 5 we addressed this question by examining a peptide ovisprin-1 by combining SFG and isotope labeling technique. To interpret the spectral intensities, we simulated

the SFG spectra using an excitonic Hamiltonian approach. We showed that the polarization dependence of either the label or the unlabeled amide I band alone does not provide sufficient structural constraints to obtain both the tilt and the twist of the ovispirin helix at a solid/liquid interface, but that both can be determined from the polarization dependence of the complete spectrum. For ovispirin, the detailed analysis of the polarized SFG experimental data shows that the helix axis is tilted at roughly 138 degrees from the surface normal, and the transition dipole of the isotope labeled C=O group is tilted at 23 degrees from the surface normal, with the hydrophobic region facing the polystyrene surface. We further demonstrated that the Hamiltonian approach is able to address the coupling effect and the structural disorder. For comparison, we also collected the FTIR spectrum of ovispirin under similar conditions, which reveals the enhanced sensitivity of SFG for structural studies of single monolayer peptide surfaces. Our study provides insight into how structural and environmental effects appear in SFG spectra of the amide I band and establishes that SFG of isotope labeled peptides will be a powerful technique for elucidating secondary structures with residue-by-residue resolution.

Understanding membrane structures of polypeptides and proteins is of essential importance to the biology society. However, the structure determination at the interface in situ is difficult due to the lack of an appropriate technique. In Chapter 6 we demonstrated for the first time that, the isotope-labeled SFG technique we developed in Chapter 5 can serve as a new route for structure determination in situ of a peptide associated with a single lipid bilayer. In Chapter 6, ten ovispirin-1 mutants, each isotope labeled at a specific site in the α-helical region of the peptides were used. The dependence of the SFG peak linewidths and frequencies on the isotope labeled amino acid residue number revealed that ovispirin-1 is lying beneath the headgroups of the DPPG/dDPPG bilayer. The positive\constructive interference of all the isotope peak

indicated that the peptide backbone tilts around 60 degrees relative to the surface normal in the DPPG/dDPPG bilayer with the C terminus closer to the headgroup region. The MD simulation performed suggested that the C terminus of peptide was tilted towards the lipid headgroup region due to the electrostatic interaction between the negative charged headgroups and the positive charged Lys 15 and Lys 16 amino acids.

Taken together, the work presented in my dissertation has shown that SFG spectroscopy is able to reveal both global and site-specific information on peptide backbone, especially when combining with other techniques. Looking beyond, our work could be extended in several directions.

First, the study of cell penetrating peptide Pep-1 could be extended to the investigation of other cell penetrating peptides and peptides associated with cargos. In particular, the delivery of nanoparticles into cells could be facilitated by surface immobilized cell penetrating peptides and the detailed mechanisms may be able to be elucidated by SFG.

Second, the combination of isotope labeling and SFG spectroscopy can be used to reveal site-specific structural information of interfacial biological molecules. In my dissertation, we mainly focus on an α-helical peptide ovispirin-1, yet this approach can be applied to other peptides, amyloids and proteins. For example, researchers are interested in how different segments of an amyloid molecule undergo conformation transition during the formation of amyloids. This can be examined in detail by the combination of isotope labeling and SFG spectroscopy.

Third, as the structure of ovispirin-1 has been well characterized in Chapters 5 and 6, this molecule can be used as a model to study the effect of more complicated lipid bilayer systems on peptide-membrane interactions.

Finally infrared probes ($^{13}C=O$, $^{13}C=^{18}O$, CN, N_3, SCN) have been widely used by vibrational spectroscopic techniques such as ATR-FTIR and 2D-IR to reveal abundant structural and dynamic information on peptides and proteins. Probes other than $^{13}C=O$ need to be explored by SFG spectroscopy so that those infrared probes could be applied to study biological molecules on surfaces and at interfaces.